Magnetic Domain Microstructure Analysis of Sintered Rare Earth Magnet Materials with high coercivity

Muhsien M. N. Yazid

B.Sc., M.Sc.

A thesis submitted for the degree of

Doctor of Philosophy

School of Electrical and Electronic Engineering

Newcastle University

United Kingdom

October 2017

The author dedicates this thesis in memory of his parents

أهدي ثمرة هذا العمل الى روح والدي العزيزين، رحمة الله عليهما

ABSTRACT

Rare earth magnet materials are commonly used in many applications, such as the motors in hybrid and electric vehicles. To improve the magnetic performance of these materials at high temperatures, certain heavy rare earth elements are added to the structure. The high demand and scarcity of heavy rare earth elements have led to a considerable increase in rare earth prices. In this context, more research is being conducted to develop of free rare earth magnets that combine high coercivity and high thermal resistance. The coercivity of sintered permanent magnet materials is controlled by the microstructural parameters of magnet such as grain shape, grain size, grain boundary, and phase morphology. As part of this research effort, a great understanding of the microstructural analysis of materials is vital. In this thesis, different areas have been identified in which improvements can be made in understanding the magnetic domain microstructure of sintered Nd-Fe-B and SmCo magnets with high coercivity.

Firstly, this thesis describes the use of magnetic force microscopy (MFM) to investigate the domain structure of sintered rare earth magnet materials in a thermally demagnetised state. Observations are made at both perpendicular and parallel surfaces to the alignment axis. Maze-like magnetic domains and stripe magnetic domains are observed in the perpendicular and parallel surfaces respectively. Branched-like domain patterns are imaged for sintered Nd-Fe-B and Sm_2Co_{17} magnets in the parallel alignment axis. Clear magnetic contrast images in 3D view with defined domain structures are presented. An important microstructural domain patterns are shown in the 3D MFM images such as spike domains and reverse spikes. Samples with wider magnetic domains have spike domain regions, whereas samples with narrower domains exhibit reverse spikes.

Secondly, a model is developed that determines the microstructural parameters, such as domain width and domain wall energy, for sintered Nd-Fe-B and SmCo magnets, from the observed MFM images. The domain width and domain wall energy have been determined in the parallel and perpendicular alignment directions. A surface parallel to the alignment axis exhibits a higher domain width and energy compared to that in the perpendicular direction. It is shown that just changing the annealing temperature can have a major effect on the domain width and domain wall energy

that leads to change the magnetic properties. In addition the ratio of root-mean-square values for MFM phase images is found to be a good indicator for the variation of magnetic properties.

Finally some distorted regions on the topographic image are observed which have a clear effect on MFM image. The effect of the distorted regions on the domain walls is studied using MFM. These regions have been identified using Raman spectroscopy. In addition, the impact of increasing temperature on the distorted regions and their corresponding domain walls is studied using MFM and Raman spectroscopy. The observation are made in-situ and at different locations of sample surface. The distorted regions are increased as the temperature raise. New methods are presented to compute the size of distorted domain walls. The techniques are 2D line profile method and watershed method.

The samples studied include both sintered Nd-Fe-B and SmCo materials aimed at understanding the microstructure of sintered Nd-Fe-B and SmCo magnets with a high coercivity.

ACKNOWLEDGMENTS

First and foremost, all praises is due to Allah Almighty (God), the most merciful and the most gracious, who gives me wisdom, health and patience to finish this work. The author would like to express sincere gratitude to those who have made this thesis possible.

A particular thanks to the Libyan Ministry of Higher Education and Scientific Research, and Benghazi University, for sponsoring this research, as without their funding this work would not have been carried out.

Many thanks are given to my research supervisors Dr Glynn Atkinson and Dr Sarah Olsen for their support, assistance and guidance. I also appreciate their patiently reading and commenting on this thesis. It is such a pleasant experience to work with them and learn from their experience that helped me through all the difficulties.

Special thanks to Dr Alan Walton from Birmingham University for providing the SmCo magnets used in this thesis. Also many thanks to Dr Ahmad Alsaab from Marine Science and Technology department for his help and support with the thesis models.

I would like to thank the technical support staff within the department; Jack Noble, Chris Manning, Allan Wheatley, John Smith, James Richardson and Stephen Robson, in helping with the equipment required for this project. Also, special acknowledgement must go to Gill Webber, the postgraduate research coordinator, for her support and great help.

Many thanks to the valuable friends in the UG lab, past and present, which have provided a motivating, enjoyable and friendly place of work. .

Finally I would like to thank my brothers and sisters who are helped me about the previous education in order to reach this stage and support me a lot. A special thank must go to my wife for her quiet patience, daily devotion and moral support. I would like to thank my lovely daughters Maisa and Maram for their warm hugs and lovely smile. Thanks to my little son Anas for changing my study mode by his lovely small smile.

TABLE OF CONTENTS

LIST OF FIGURES

LIST OF TABLES

LIST OF SYMBOLS

The common symbols used in this thesis are listed below.

AFM	Atomic force microscope	M_s	Magnetisation saturation
A_{ex}	exchange coefficient	N_{eff}	Effective demagnetizing factor
B	Flux density	SEM	Scanning electron microscopy
B_r	Residual flux density	S_V	Magnetic viscosity
$(BH)_{max}$	Maximum product energy	T	Temperature
D	Grain size	TEM	Transmission electron microscope
D_w	Domain width	v	Reversed nucleus volume
H	Magnetic field applied	v_a	Activation volume
H_c	Coercivity or coercive field	XRD	X-ray diffraction
H_{ci}	Intrinsic coercive force	Φ	Gibbs free energy
HDD	Hard disk drive	β	Coefficient
H_A	Anisotropy field	α	Nucleus nature
k	Boltzmann's constant	γ_w	Domain wall energy
K	Anisotropy constant	μ_0	permeability
kT	Temperature dependence	($^{//}$)	Parallel
MFM	Magnetic force microscopy	$\perp$	Perpendicular
M_r	Remanence magnetisation	$Ø_{r,m,s}$	Root-mean-square values of phase shift
M	Magnetisation	3D	Three dimensional

CHAPTER 1 INTRODUCTION

1.1 Introduction

Permanent magnet materials are commonly used in most modern technology. Applications such as electric vehicles, motors, generators, electronic goods, data recording devices, automobiles, and quantum devices use high performance hard magnetic materials. The high performance is achieved by including rare-earth intermetallic compounds in the materials. This enables high energy densities at high operating temperature. At room temperature, sintered Nd-Fe-B currently exhibits the highest remanence, intrinsic coercivity, and energy product of all magnetic materials. However, to improve the performance of sintered Nd-Fe-B magnet at high temperature, some heavy rare earth elements are added to the structure of material. Due to their performance boosting properties, there is a high demand for rare earth materials but only limited supplies are available. Gutfleisch *et al.* in 2011 estimated that 97% of global rare earth magnets are supplied from China [1]. This has led to significant increase in rare earth prices [1, 2]. Lewis *et al*. in 2013 reported the sales profiles of the four types of permanent magnets, and Nd-Fe-B magnets saw the fastest growth in sales in the previous 10 years, and expected to increase over $17 billion on 2020 [3]. The availability and price of dysprosium Dy, which is used to enhance the properties of Nd-Fe-B, have been particularly volatile [1]. In some applications [1, 4] a new generation of sintered Sm_2Co_{17} are being used to substitute Nd-Fe-B where high temperature is required. The main priority for permanent magnet material research is to simultaneously achieve high coercivity (H_c), high remanence (B_r), and high Curie temperature. Consequently research is now being conducted to develop free heavy rare earth magnet with high performance and heat resistance [5-8]. Therefore, it is important to understand the microstructural analysis of materials in greater detail.

Previous research has shown that studying the microstructure of magnets in terms of grain boundary isolation and magnetisation reversal is vital for developing high coercivity magnets. In this context, it is stated that the coercivity of sintered permanent magnet materials such as SmCo and Nd-Fe-B is controlled by the microstructural parameters of magnet such as grain shape, grain size, grain boundary, and phase morphology. The crystal structure of sintered Nd-Fe-B magnets

comprises mainly of a hard magnetic $Nd_2Fe_{14}B$ matrix surrounded by Nd-rich phase. The Nd-rich phases between grain boundaries and at triple junctions play a crucial role in the coercivity mechanism. The Nd-rich phases have a great impact on the domain wall movement. It is vital to understand the effect of Nd-rich phases on the domain wall and the change of magnetic anisotropy that lead to the possibility of improving coercivity. Extending reversal magnetisation and reducing coercivity have been possible by observing the behaviour of magnetic domains [9]. Therefore, the work in this thesis stems from this initiative.

1.2 Aims of the study

The work aims to understand the magnetic microstructure of sintered rare earth magnet materials by the observations of micromagnetic domain patterns using magnetic force microscopy (MFM). The project is targeted to achieve the following:

- Evaluation of micromagnetic domain structure of sintered rare earth magnet materials using magnetic force microscopy (MFM).
- Analysing the domain microstructures in the 3D view of MFM images.
- Determination of micromagnetic parameters, such as domain width and domain wall energy, form MFM images.
- Estimate the variation of magnetic properties of sintered permanent magnet materials using MFM images.
- Study the structure of grain separation of sintered rare earth magnet materials.
- Observation of the impact of some distorted regions on domain patterns using MFM.
- The possibility of using Raman spectroscopy to identify the distorted regions.
- Study the effect of increasing temperature on distorted regions using MFM and Raman spectroscopy.

This work has allowed to study the impact of grain separation phases on magnetic domains patterns using MFM technique.

1.3 Scientific contribution

The lists below are the important scientific contributions that are stemmed from this study.

1- Observation of micromagnetic domain structure for sintered Nd-Fe-B and SmCo magnets at surfaces perpendicular and parallel to the alignment axis. The magnetic domains have maze-like and stripe-like patterns in both the perpendicular and parallel alignments respectively. Branched-like domain patterns is appeared in the parallel side for sintered Nd-Fe-B and SmCo magnets.

2- Novel 3D analysis of magnetic domain microstructure using MFM method. The 3D data explains the domain structure more clearly and distinguishes unwanted features.

3- Determination of domain width and domain wall energy for sintered rare earth magnet materials. These parameters are calculated in both parallel and perpendicular directions.

4- Evaluation of the ratio of root-mean-square values for MFM phase images of sintered Nd-Fe-B and SmCo materials. These values are found to be an indicator for the variation of magnetic properties of the studied samples.

5- Observation of some distorted regions that have a great impact on domain wall size.

6- New methods compute the size of distorted domain walls. The techniques are 2D line profile method and watershed method.

7- Observation of the distorted domain walls at elevated temperatures of up to 120°C using MFM method. The distorted regions are increased as the temperature raise. The growth of distorted domain walls with increasing temperature are viewed in 3D. The observation is made in-situ and at different locations of the same sample surface.

8- Using Raman spectroscopy for the first time to identify the distorted regions. The variation of distorted regions is analysed using Raman spectroscopy at room and high temperature.

1.4 List of Publications

The research in this thesis has resulted in the following journal paper, conference proceedings, and academic awards:

- **Journal paper**

1- **M. M. Yazid,** S. H. Olsen, and G. J. Atkinson**,** "MFM Study of a Sintered Nd-Fe-B Magnet: Analyzing Domain Structure and Measuring Defect Size in 3-D View," *IEEE Transactions on Magnetics,* vol. 52, pp. 1-10, 2016.

- **Conference proceedings**

2- **M. M. Yazid,** S. H. Olsen, and G. Atkinson, "Comparison of magnetic microstructure for different sintered SmCo Alloys obtained using magnetic force microscopy," *In 1st IEEE Conference Advance in Magnetics Proceedings* (**AIM2016**), Bormio, Italy, March 14-16 2016.

3- **M. M. Yazid,** S. H. Olsen, and G. Atkinson, "Nucleation regions and coercivity mechanism of sintered permanent magnet materials," *In Proceedings of 24rd international workshop on rare earth and future permanent magnets and their applications (REPM2016)*, Darmstadt, Germany, 2016.

4- **M. M. Yazid**, S. H. Olsen, and G. Atkinson, "Nucleation regions and coercivity determination of sintered Nd-Fe-B magnets," in *2016 International Conference for Students on Applied Engineering (ICSAE)*, 2016, pp. 340-344.

- **Invited Talk**

5- **M. M. Yazid,** S. H. Olsen, and G. Atkinson, "Magnetic microstructure investigation of rare earth materials for motors," *UK Magnetic Society* , Newcastle, UK, 26-02- 2016.

- **Academic Awards**

1- **"Best Poster"** In the International Conference for Students on Applied Engineering (ICSAE 2016), Newcastle, United Kingdom, 20-21 October 2016.

2- Third place for **"Best Paper Presentation"** in the Electrical Power research group at the School of Electrical and Electronic Engineering, Annual Research Conference, ARC2016.

3- Second place for **"Best Poster"** in the Electrical Power research group at the School of Electrical and Electronic Engineering, Annual Research Conference, ARC2014.

The following works are future submission:

1- **M. M. Yazid**, S. H. Olsen, G. Atkinson, and Alan Walton, "3D analysis of magnetic domain structure for sintered SmCo magnets," future manuscript for consideration for publication in Journal of Applied Physics (JAP).

2- **M. M. Yazid,** S. H. Olsen, and G. Atkinson, "Thermal analysis of distorted regions of sintered Nd-Fe-B magnets," future manuscript for consideration for publication in Journal.

1.5 Thesis structure

This thesis describes the use of magnetic force microscopy (MFM) to investigate the domain structure of sintered Nd-Fe-B and SmCo magnets in a thermally demagnetised state. The thesis is divided into seven chapters. The structure of the thesis as following:

- Chapter one consists of a general discussion about the applications and issues of sintered rare earth magnet materials and some information on the thesis layout. Aims and scientific contribution of the work are presented. The publications stemmed for this work are listed.
- Chapter two introduces a literature survey on the field of permanent magnet materials, in terms of the historical development of hard magnets, magnetic properties, microstructure analysis, the magnetisation process, and commercially used types of materials. In this review, attention is focused on the basic concepts of microstructure analysis and micromagnetic domain analysis for sintered permanent magnet materials as these subjects relate closely to the aims of this thesis.
- Chapter three considers the local techniques employed in this research in terms of basic principles and the process developed. The samples used are discussed in detail in this chapter, including their magnetic properties and surface preparation requirements. In addition any models and software used in this research have been discussed.
- Chapter four describes the domain structure for the proposed sintered Nd-Fe-B and SmCo magnets that are observed using MFM in both perpendicular ($\perp$) and parallel ($^{//}$) directions in relation to the alignment axis. Attention is focused on analysing domain patterns in the 3D view to clarify the domain structure.

- Chapter five discusses the determination of domain width and domain wall energy in the parallel and perpendicular alignment directions. In addition, the ratio of root-mean-square values for MFM phase images ($Ø^{\perp}/Ø^{//}$) is found to be a good indicator for predicting the magnet properties. The ratio of $Ø^{\perp}/Ø^{//}$ is determined in both direction alignment, parallel and perpendicular.
- Chapter six presents the effect of grain separation on domain patterns of the proposed sintered Nd-Fe-B magnet, observed using MFM technique. This chapter studies the impact of increasing temperature on some distorted regions appeared on the MFM images. The distortion regions have been illustrated in 3D view. In addition the use of Raman spectroscopy, to identify the distorted regions at room and high temperature, is presented in this chapter.
- Chapter seven illustrates the overall conclusions of the thesis and recommendations for future work.

1.6 Summary

In this chapter, a general discussion about the applications and issues of sintered rare earth magnet materials has been conducted. It is apparent that rare earth magnet materials have been the preferred choice of materials in many applications. The prices of sintered rare earth magnets have been significantly increased. The high demand and increased prices of sintered permanent magnet materials have led to direct research into understanding the microstructure properties of these materials in order to a locate substitution or improve the existing rare earth magnet materials. The targets of this research were clearly mentioned, and the main aim is to understand the magnetic microstructure of sintered rare earth magnet materials by the observations of micromagnetic domain patterns using magnetic force microscopy (MFM). The thesis structure has been split into mainly seven chapters, and the purpose of each chapter was explained. Next chapter will describe the literature study about the work in detail.

CHAPTER 2 LITERATURE REVIEW

2.1 Introduction

Most modern technology depends on permanent magnet materials, such as electric vehicles, motors, generators, electronic goods, data recording devices, automobiles, and quantum devices. High performance hard magnetic materials are based on rare-earth intermetallic compounds that provide high energy densities at different operating temperatures. However, to improve the magnetic performance of hard magnet materials at high temperatures, certain heavy rare earth elements are added to the structure, such as dysprosium (Dy) in Nd-Fe-B magnets. The high demand for rare earth materials and the expected short supply of heavy rare earth elements has led to a considerable increase in rare earth prices in recent years. Consequently research is now being conducted into hard magnetic materials that are free of heavy rare earth elements but still offer high performance and heat resistance [5-8]. As part of this research effort, a great understanding of the microstructural analysis of materials is vital. More emphasis in research has been directed toward controlling the microstructure of grain boundary phases which are important in understanding the coercivity mechanism.

In sintered permanent magnet materials such as SmCo and Nd-Fe-B, the coercivity is controlled by the microstructural parameters of magnet such as grain shape, grain size, grain boundary, and phase morphology. The crystal structure of sintered Nd-Fe-B magnets comprises mainly of a hard magnetic $Nd_2Fe_{14}B$ matrix surrounded by Nd-rich phase. However, the Nd-rich phases between grain boundaries and at triple junctions play a crucial role in the coercivity mechanism.

In this chapter a literature survey introduces the field of permanent magnet materials, in terms of the historical development of hard magnets; magnetic properties; microstructure analysis; the magnetisation process; and commercially used types of materials. In this review, attention is focused on the microstructural analysis and coercivity of sintered Nd-Fe-B magnet materials, as these subjects relate closely to the aims of this thesis. The effect of microstructure on domain wall movements and coercivity is discussed. In addition models for determination of domain width and domain wall energy are stated in detail along with relevant expressions.

2.2 Modern permanent magnet materials

Permanent magnet materials have been developed at various times over the centuries, and an extraordinary improvement has been witnessed in the twentieth century. The first modern development of hard magnetic materials was announced in 1930 and the products were named as Alnico magnets, with double the coercivity compared to the magnetic steel of the era [10-12]. These materials have strong anisotropy with a two-phase nanostructure comprising of small Fe-Co particles participating in the magnetic Al–Ni matrix which can lead to a significant magnetic hardness [3]. In addition, there are two possible ways of producing Alnico alloys: sintering or casting. This creates Alnico materials with maximum energy products from 40 to 56 kJ/m^3 (5-7 MGOe). These materials have low coercivity and magnetisation, high operating temperature, and good resistance to corrosion. The next material to be developed was the ferrite magnet, also known as a ceramic. The first commercial ferrite magnets were introduced in 1952 by the Philips Company in response to the need for non-metallic and electrically insulating materials [13]. These materials are made from iron oxide combined with barium or strontium carbonate, using pressing and sintering techniques. However, ferrite magnets possess a rather low remanence (typically 0.35 Tesla), and a low energy product; they are however easy to process, and commercially important [3]. Therefore, these materials are widely used for inexpensive, low-performance applications such as kitchen appliances.

Rare earth-cobalt permanent magnets (R-Co) were discovered in the 1960s in types of intermetallic RCo_5 compounds [14]. The early generation of these magnets was made of $SmCo_5$ with high maximum energy products and coercivity. To date, the maximum energy produced for $SmCo_5$ has reached the range from 14 to 24 MGOe with high temperature capability (250-350°C). The next innovation in rare earth magnets came in the 1970s and is recognised as Sm_2Co_{17} with the addition of Cu,Fe and Zr [15]. Sm_2Co_{17} has a high Curie temperature, increased magnetisation, high coercivity, and rather low magnetocrystalline anisotropy in contrast to $SmCo_5$ [16]. Generally, SmCo magnets have become commercially widespread with maximum energy products today in the range of 22 to 32 MGOe and Curie temperature approximately of 750°C, making them the best choice for high temperature applications [17].

A new direction in the development of the rare earth magnet family occurred in the 1980s. In 1983, General Motors Inc., the U.S. Naval Research Laboratory (NRL) and Sumitomo Special Metals in Japan discovered the neodymium iron boron permanent magnet materials. Each of these groups established a separate route for the development process of Nd-Fe-B materials. The ternary $Nd_2Fe_{14}B$ was quasi-simultaneously reported for sintered magnets and quenched magnets by Sagawa *et al* [18] and Croat *et al* [19, 20] respectively. The Nd-Fe-B magnets produce higher maximum energy products comparing to SmCo magnets. The sintered magnets can now have energy products up to 50 MGOe and bonded magnets up to 14 MGOe. These materials have a high remanence (>1 Tesla) and linear B-H characteristics in the second quadrant. Moreover, the Nd-Fe-B magnet has a low Curie temperature, low magnetocrystalline anisotropy and relatively cheap energy-density per unit at room temperature. Therefore, heavy rare earth elements (mainly Dy and Tb) have to be added to these materials in order to improve magnet performance at high temperatures (> 100 ◦C). The scarcity of heavy rare earth elements is a key problem with Nd-Fe-B materials. There is presently a great effort underway to decrease the use of heavy rare earths by using different methodologies [5-7]. With today's technology, Nd-Fe-B has become the most commercialised permanent magnet material available.

Generally, permanent magnet materials are designated as hard magnetic material. Materials described as hard magnetic have sufficiently high resistance to demagnetisation (coercivity), and hence the coercivity of permanent magnet materials is categorized as above 10 kAm^{-1} (125Oe). They have strong magnetic properties in terms of magnetic induction, maximum energy product and resistance to demagnetisation. The energy products of permanent magnet materials have been enhanced over the past 100 years as shown in Fig 2.1, starting from nearly 1 MGOe for steels in the early twentieth century, increasing to ≈ 3 MGOe for ferrites and finally at 56MGOe for Nd-Fe-B [1].

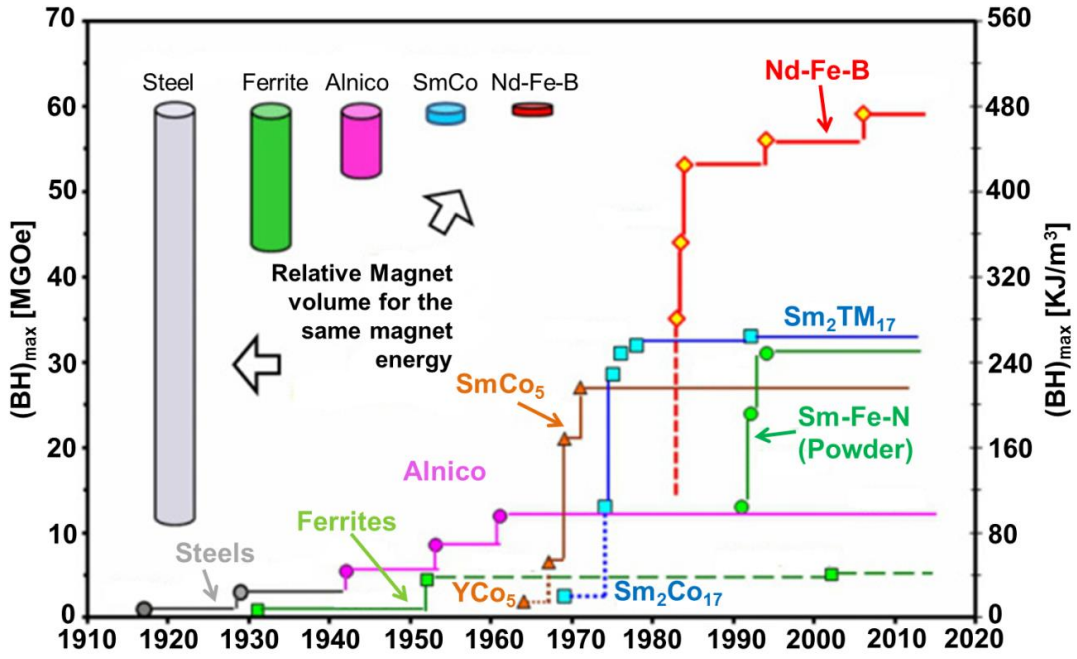

Figure 2-1 Development on the energy products $(BH)_{max}$ of hard magnetic materials in the 20th century [1].

2.3 Criticality of permanent magnet materials

The most important ingredients in producing high-energy permanent magnets are rare earth elements. In recent years, rare earth magnet materials have been the most advanced choice for materials in many applications. This is mainly because of their spectacular magnetic properties, and the demand for device designs of lower weight and smaller size. Nd-Fe-B magnets currently have the highest energy density available for use in high-performance motors and generators in contrast to other classes of magnets (Ferrite, Alnico, SmCo and Sm-Fe-N magnets). Recently, the production of sintered Nd-Fe-B magnets with large amounts of Dysprosium (Dy) has been common in order to develop high coercivity grades with high thermal stability. A list of applications and products which use Nd-Fe-B magnets is shown in table 2.1. Applications such as hard disk drive components, hybrid/electric vehicles, electric bicycles, and wind power generators are the most common and popular applications using Nd-Fe-B magnet. These products are anticipated to experience dramatic increase in demand over the next decade.

Furthermore, China has dominated the entire world production of rare earth oxides for more than a decade since the 1990s. Gutfleisch *et al.* in 2011 estimated that 97% of global rare earth magnets are supplied from China [1]. The high demand and the

expected supply shortages have led to a significant increase in prices of rare earth magnets. Lewis *et al*. in 2013 reported the sales profiles of the four types of permanent magnets, and Nd-Fe-B magnets saw the fastest growth in sales in the previous 10 years, and expected to increase over $17 billion on 2020 [3]. The availability and price of dysprosium Dy, which is used to enhance the properties of Nd-Fe-B, have been particularly volatile [1].

The combination of both price increase and demand rise for Nd-Fe-B is known in the press as the rare earth crisis. Therefore, the issues associated with today's rare earth supply need to be addressed in more depth.

Table 2-1 The Nd-Fe-B magnet applications and products [3]

Category:	Application Examples:
Computer and office automation	Desk drive spindle motor, voice coil motors, CD-ROM spindle motors, printer and fax motors, fax stepper motors, printer hammer, and copy machine rollers.
Automotive and transportation	Starter motors, electric steering, sensors, electric fuel pumps, instrumentation gauges, brushless DC motor, and electric bicycles.
Consumer Electronics	VCRs and camcorders, cameras, speakers, headsets, microphones, pagers, DVD players, watches and cell phones.
Appliances & systems	Portable power tools, household appliance motors, scales, air conditioners, water pumps and security systems.
Factory automation	Magnetic couplings, pumps motors, servo motors, generators and bearings
Medical industry	Magnetic resonance, imaging equipment, surgical tools and medical implants.
Alternative energy	Hybrid/ electric vehicles, electric bicycles, wind power systems, wave and tidal power systems, power generation systems and energy storage systems.
Military	Weapons systems, vehicles, watercraft, avionics precision-guided munitions, communications systems and radar satellites.

2.4 Recent developments in sintered permanent magnets

In order to satisfy the demand for advanced permanent magnet materials, the creation of high energy product magnets free from rare earth content must be established.

Therefore, different challenges have been considered in the literature which may change the shape of future research into hard magnetic materials.

On the one hand, many industry sectors and scientific institutions are beginning to conduct research and development on substitution options for rare earth materials, but no alloy or component has yet been discovered that has all the properties required. E. Kneller and R. Hawing proposed in 1991 the idea of obtaining a high energy product magnet by making an exchange coupled at the nanoscale level between hard/soft nanocomposite phases at the mutual interface, also known as the exchange spring [21]. The soft magnetic phase would provide large saturation magnetisation, while the hard phase would offer high anisotropy and high coercivity. There has been considerable interest in this idea, but no commercial products have yet resulted [22].

On the other hand, research is now being conducted into Dy-free sintered Nd-Fe-B magnets with high coercivity H_c and heat resistance [5-8]. In order to achieve this aim, it is significantly important to understand the mechanism of coercivity in greater detail. Microstructure analysis is critical for magnet coercivity in terms of the grain boundary structure, magnetic isolation of the grains, and magnetisation reversal. Fig. 2.2 illustrates the routes towards improving coercivity with the percentage of Dy addition.

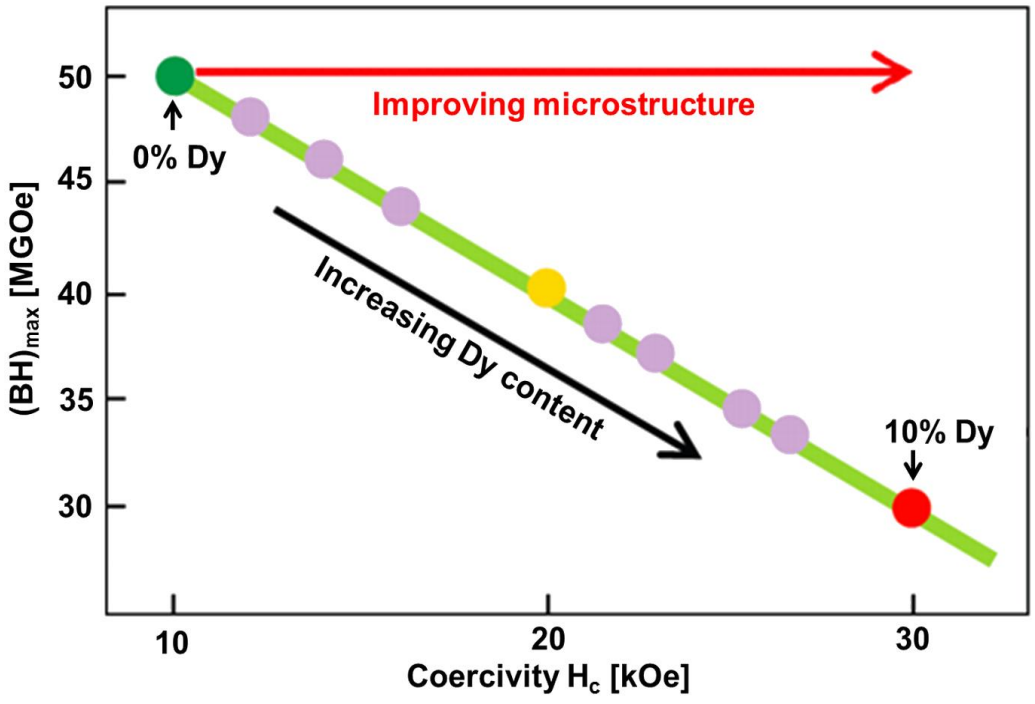

Figure 2-2 Routes towards improving coercivity with the percentage of Dy addition.

More emphasis in research has been directed toward controlling the microstructure of grain boundary phases, which is important for understanding the magnetisation reversal that is relevant to the coercivity mechanism. However, no study has yet correlated the coercivity mechanism with magnetisation reversal in sintered Nd-Fe-B magnets experimentally. Most recent studies depend on simulation and the fabrication of magnetic microstructures [5, 23, 24].

In addition, in some applications [1, 4] a new generation of sintered Sm_2Co_{17} are being used to substitute Nd-Fe-B where high temperature is required. However, the key components in the future development of magnetisation structures are the precise observation and accurate control of material microstructure.

2.5 Microstructural analysis of sintered Nd-Fe-B magnets

Sintered Nd-Fe-B magnets were first produced in 1984 by Sagawa *et al*. [18]. These magnets exhibit the highest remanence, intrinsic coercivity, and energy product in contrast to other rare earth magnets. The main priority for developers of permanent magnet materials is always to achieve high coercivity and remanence (B_r). Microstructural variables such as grain size and phase morphology have a strong influence on coercivity and remanence. The coercivity (H_c) of a magnetic material varies inversely with grain size (D) [25]. Detailed knowledge and a complete understanding of the magnetic microstructure of materials are very important for the development of high performance permanent magnets in order to achieve high coercivity (H_c). In this context, knowledge of magnetic domain behaviour in relation to macroscopic parameters shows that the physical microstructure of magnets has a strong influence on coercivity and remanence. The microstructure of grains and domains is discussed in detail in sections 2.5.1 and 2.5.2 respectively.

2.5.1 Crystal structure:

The crystal structure of sintered Nd-Fe-B magnets consists mainly of a hard magnetic $Nd_2Fe_{14}B$ matrix. To improve the magnetic properties of Nd-Fe-B magnets at high temperature, minor phases are added to the Nd-Fe-B phase. These include: Dy substitution for Nd; Co substitution for Fe; $NdFe_4B_4$ phase; Nd-rich phase; α-Fe; and Nd oxides and pores [26]. The typical crystalline microstructure of sintered Nd-Fe-B magnet is imaged using SEM in Fig. 2.3.

The grey area in Fig 2.3 is the grain structure of a magnet, which is mainly the hard $Nd_2Fe_{14}B$ magnetic phase and is responsible for the magnetic properties. Heavy rare earth elements such as Nd-rich and Dy are located at the grain boundary (the white area between grains in Fig. 2.3). The grain boundary phases have a major impact on magnet coercivity and performance.

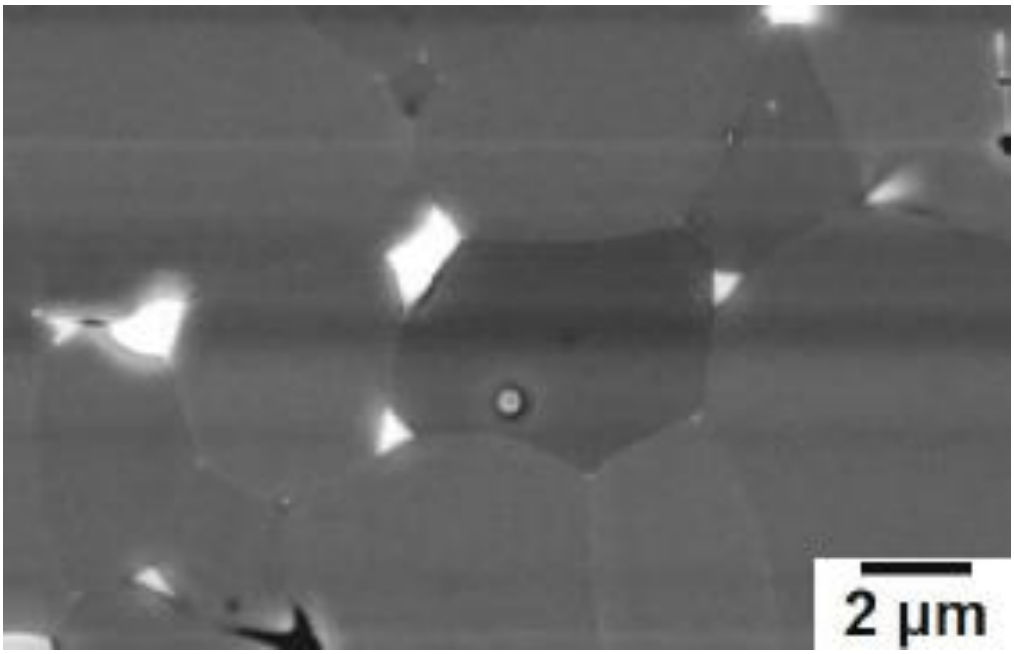

Figure 2-3 Sintered NdFeB microstructure imaged using SEM [27, 28].

The crystal structure of the hard $Nd_2Fe_{14}B$ magnetic phase is tetragonal in shape with uniaxial crystalline anisotropy. The magnetisation direction of the ferromagnetic atoms aligns in the c-direction with magnetic moments along the c-axis. There are two directions of magnetisation for each grain: upwards along the c-axis or downwards. Generally, to achieve high coercivity, the tetragonal $Nd_2Fe_{14}B$ matrix phase has strong magnetocrystalline anisotropy. This causes the alignment of the magnet to be preferred along the c-axis (alignment axis) [29]. In addition, the magnet magnetisation (remanence) arises from the spontaneous magnetisation (M_s) of the $Nd_2Fe_{14}B$ phase [2].

The next section will discuss the grain boundary phases and triple junction of sintered Nd-Fe-B magnet in more details.

2.5.2 Grain boundaries and triple junctions

The grain boundary phase separates the hard magnetic grains from each other and prevents magnetic interaction between grains. The grain boundary phases prevent

the propagation of reversal domains from one grain to another; instead a nucleation of reversal domains is generated in each grain. Usually, a paramagnetic Nd-rich phase is added as an insulation layer between the grains and is located at the boundary and triple junctions. The Nd-rich layers are present in the sintered Nd-Fe-B magnet in oxide and metallic phases [30].

Woodcock *et al*. [2] observed the microstructure analysis of sintered Nd-Fe-B magnet using backscattered electron microscopy, as shown in Fig. 2.4. The dark regions are crossponding to the $Nd_2Fe_{14}B$ phase and the white contrast areas related to the Nd-rich regions (metallic Nd, NdO or Nd_2O_3). It has been revealed that the grains of $Nd_2Fe_{14}B$ are rounded by thin layer of Nd-rich phases and large Nd-rich grains at the triple junctions. The larger and more rounded Nd-rich regions in the triple junctions are oxides in character whereas the smaller layers in the boundaries are metallic.

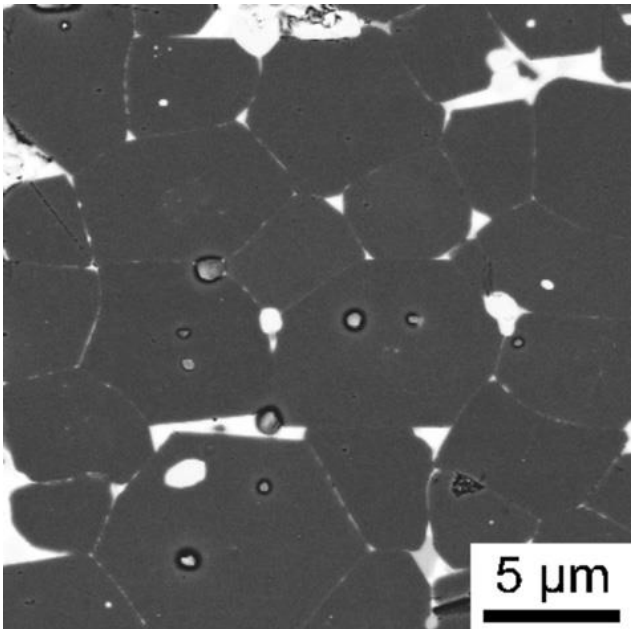

Figure 2-4 Typical $Nd_2Fe_{14}B$ grains, grain boundary and triple junctions of sintered Nd-Fe-B magnet revealed using backscattered electron microscopy [2].

Sasaki *et al*. [31] reported the observation of microstructure of sintered Nd-Fe-B magnets in directions both in-plane and out of plane to the alignment axis, using backscattered electron SEM, as shown in Fig. 2.5. It is shown that the grain boundary and triple junction comprises from five different phases of Nd-rich and only NdO phases are confirmed at the large triple points. In addition, Sepehri-Amin

et al. [32] stated that NdO_x and Nd_2O_3 phases appear as almost spherical in shape at the triple junction and produce minimum interfacial energy.

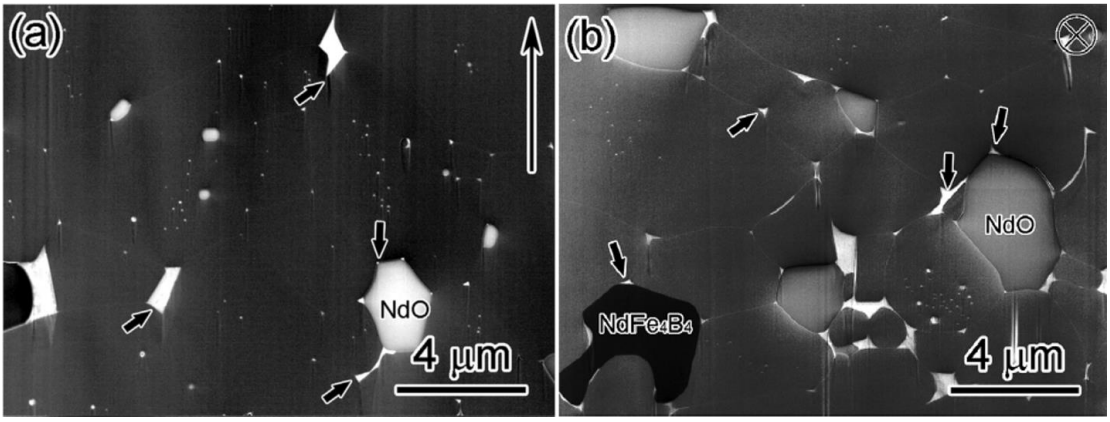

Figure 2-5 the microstructure of Nd-Fe-B sintered magnets are imaged using Backscattered electron SEM in directions both in-plane (a) and out of plane (b) to alignment axis [31].

Recently, more research has been conducted into the microstructural formation of the grain boundary phase [32-36]. These studies concluded that the crystal structure of Nd-rich phases at the triple junctions of sintered Nd-Fe-B magnet composed of several phases such as face centred cubic (fcc)-Nd, fcc-NdO, and hexagonal close packing (hcp)-Nd_2O_3, and these phases are referred to Nd oxides for simplicity.

Various types of heavy rare earth elements are added to the structure of Nd-Fe-B for different reasons. The most important element is dysprosium (Dy) as a replacement for neodymium. The addition of Dy improves magnet coercivity and increases the operating temperature. Furthermore, the temperature coefficient of the $Nd_2Fe_{14}B$ compound is improved by the substitution of Fe with cobalt (Co), leading to an increase of the Curie temperature, but the coercivity is reduced [26]. The addition of Co also improves the material's resistance to corrosion.

Therefore, the segregation of the magnetic domains at grain boundaries is an important concern in the development of high coercivity magnets. However, it is difficult to experimentally analyse the influence of the microstructure of grain boundary on coercivity; instead simulations are conducted to describe the relevant correlations. Detailed explanation about the microstructure and coercivity are discussed in detail in section 2.11.

2.5.3 Domain structure

Each grain of sintered Nd-Fe-B magnet consists of a multi-domain structure in the demagnetised state. The boundaries between the main domains are known as domain walls or Bloch walls. The total magnetic energy is minimized by the formation of domains. The formation of domains depends mainly on four energy factors: exchange energy; magnetostatic energy; crystalline anisotropy; and magnetostrictive energy [37]. The size and shape of domains depends on the crystalline and magnetostrictive energies. The anisotropy and exchange energies influence the width of the domain wall.

Nd-Fe-B magnets have strong uniaxial crystalline anisotropy and narrow domain walls. Fig. 2.6 presents the domain structure of Nd-Fe-B magnets imaged using Kerr microscopy in the thermally demagnetised state.

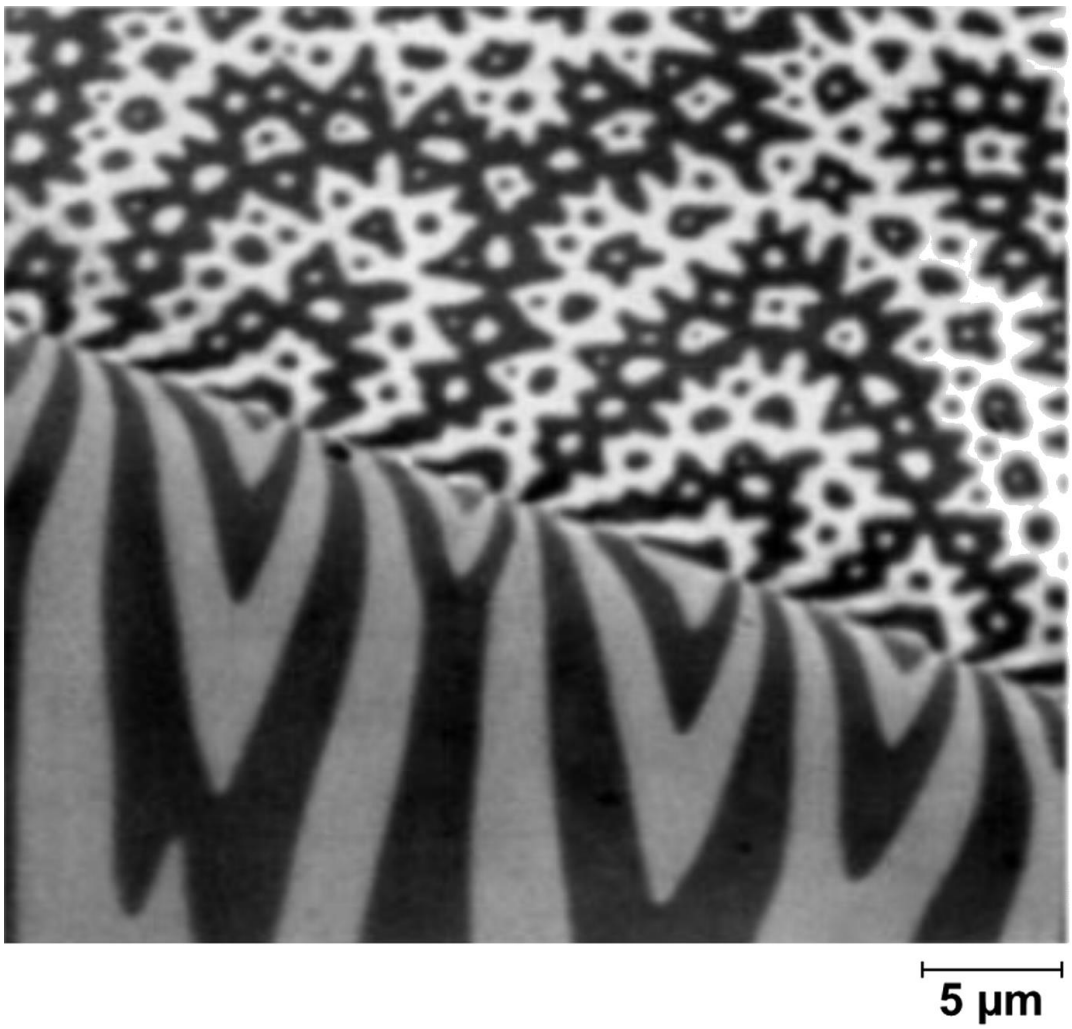

Figure 2-6 Kerr microscopy image obtained around a twin boundary in a Nd-Fe-B magnet [38].

The domain structure of Nd-Fe-B appears in different patterns depending on the direction of magnetic alignment axis. Using magnetic force microscopy (MFM), Folks *et al* [39] described the microstructure observation of sintered Nd-Fe-B along the perpendicular alignment axis as a magnetic domain with different patterns such as bubble domains and stripe domains. Furthermore, in 2006, Szmaja reported the domain structure of different samples of sintered Nd-Fe-B as observed by MFM in a direction perpendicular to the alignment axis, describing its appearance as maze domain and reverse spikes [40].

The main domains and domain walls are detected when the magnet is thermally demagnetised, but at magnetisation saturation, the main domains are considered as single domains with magnetic dipoles aligned in one direction. The relationship between magnetic domains and the magnetisation process is discussed in the next section.

2.6 Magnetic hysteresis loop and the magnetisation process

The magnetic hysteresis loop appears for all types of magnet materials, from the softest to the hardest, and denotes the magnetisation process of the materials. Essentially, a ferromagnetic material consists of a miniature particle in a large number of areas called magnetic domains, and every single domain represents a small magnet. The orientation of each domain is changeable according to the process of magnetisation. Fig. 2.7 shows the hysteresis loop of permanent magnet materials, and simplifies the alignment of the magnetic domain in a graphical illustration, during the processes of magnetisation and demagnetisation of the magnet. In this figure, the X-axis shows the magnetic field applied and the Y-axis shows magnetisation M or flux density B.

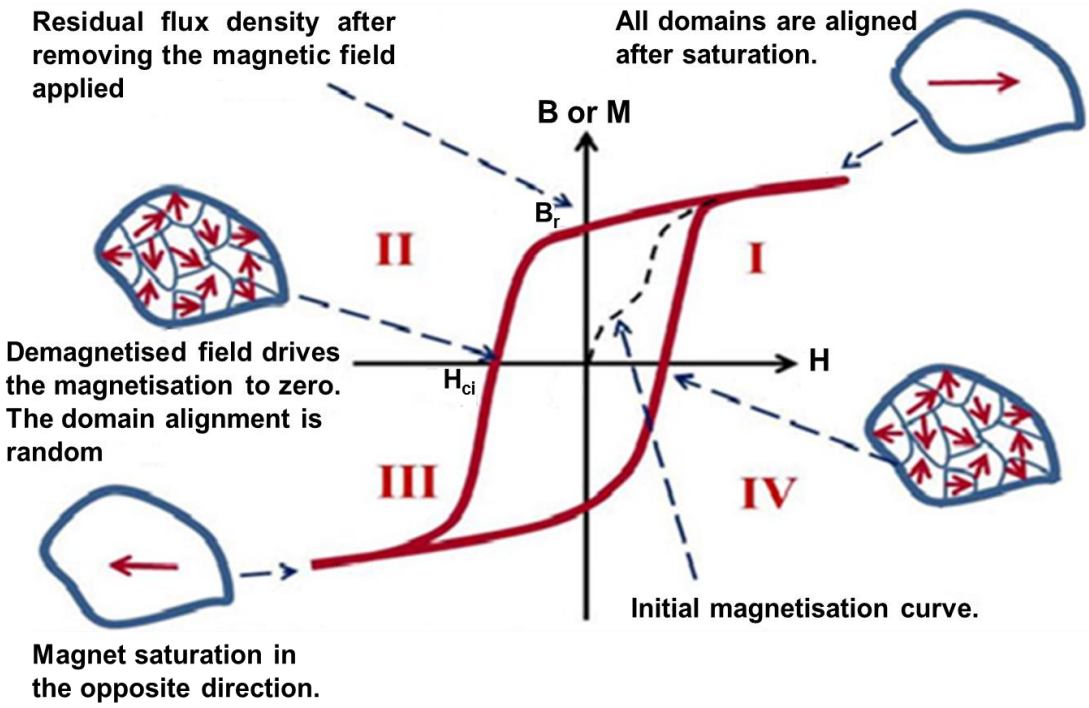

Figure 2-7 Schematic representation of magnetic domain alignment and the hysteresis loop of permanent magnet materials**.**

Starting from the origin point, when the magnetic field is first applied to the permanent magnet materials, induction B or magnetisation M increases with an increase the magnetic applied field. The magnetising procedure follows the dashed line in the figure above, which is called the initial magnetisation curve. At this stage the magnetic domain curves in the same direction as the magnetising field. At some point, the magnetisation will reach saturation, which means that there is only a small increase in flux density as the magnetic field increases. However, when the applied field is reduced to zero, much of the magnetisation remains, and this is defined as the residual flux density (B_r). On the other hand, when a negative magnetic field is applied, the magnetisation M is minimized to zero and the domain direction rotates to be parallel to the demagnetisation field. A significant force is needed to reduce the magnetisation M to zero, and this is defined as the intrinsic coercive field (H_{ci}). The material will become saturated in the opposite direction when a higher negative field is applied. Moreover, an identical shape can be perceived in the rest of the curve and closed back again to the first quadrant.

In addition, because of the significant field required to saturate the magnet in both directions, the loop in the Fig. 2.7 is a major hysteresis loop. Hence, the magnetic material data should be supplied based on a major hysteresis loop, unless clearly

stated otherwise [41]. However, the hysteresis loop in the second quadrant is the best way to describe the magnetic properties of permanent magnet materials, as shown in Fig. 2.8, which is sometimes referred to as the "demagnetising curves".

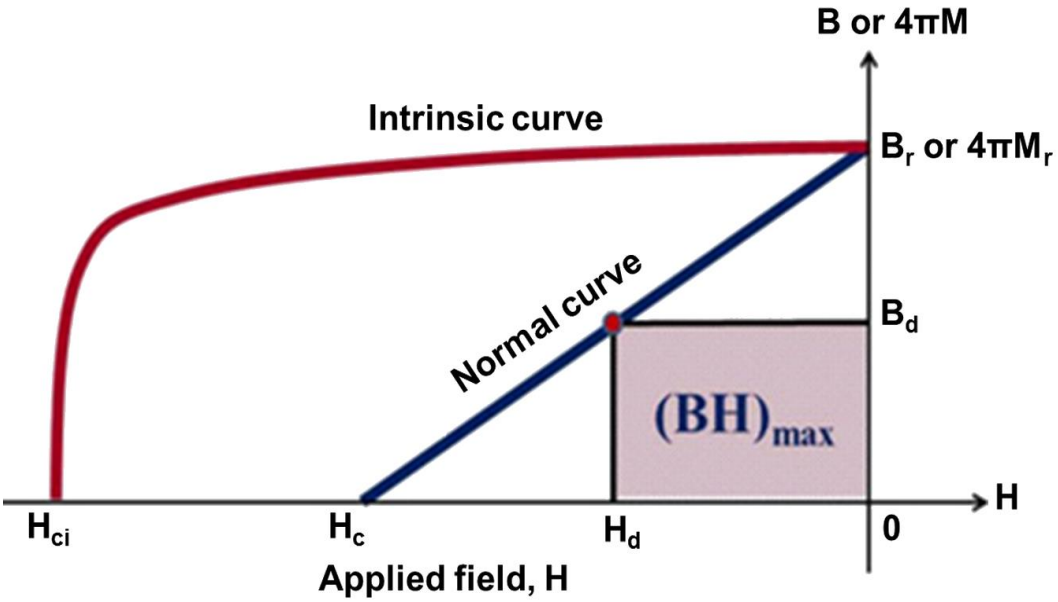

Figure 2-8 Typical intrinsic and normal demagnetisation curves**.**

In Fig. 2.8, the H versus B_r or $4\pi M_r$ is named the intrinsic demagnetisation curve, and H versus B is called the normal or extrinsic demagnetisation curve. The magnetic induction or flux density (B) of permanent magnet materials is large in value and is given by:

$$B = H + 4\pi M \text{ (CGS)} \tag{2.1}$$

$$B = \mu_0 (H + M) \text{ (SI)} \tag{2.2}$$

where M is magnetisation and H is the magnetic field applied. Usually, the magnetic field is negative in the second quadrant of demagnetisation curves; hence, the normal curve is below the intrinsic curve. In addition, M = 0 in free space, and thus $B = \mu_0 H$ in the SI units, where μ_0 is the permeability of free space ($\mu_0 = 4\pi \times 10^{-7}$ Tesla*m/A). In a closed circuit after saturation and the removal of magnetic field (H=0), the remaining magnetic flux density is called the residual induction (B_r); therefore, $B_r = \mu_0 M_r$.

Consequently, the demagnetising field required to reduce the magnetic flux density to zero is called the coercivity (H_c), whereas the demagnetising field required to maintain magnetisation M = 0, also known as the intrinsic coercive force (H_{ci}). Therefore, the intrinsic coercivity represents the magnet's ability to resist

demagnetisation. Mathematically, coercivity (H_c) cannot be higher than the intrinsic coercivity H_{ci}.

In fact, to identify the performance characterisation of permanent magnet materials, the maximum energy product is often of interest, which is the maximum value of $(BH)_{max}$ achieved in the second quadrant. This energy is written as a point (B_d, H_d) along the normal demagnetisation curve as shown in Fig. 2.8. The shaded area under the normal demagnetisation curve represents the maximum value of (B_d*H_d) or the maximum energy product $(BH)_{max}$. This maximum energy product is measured in Mega Gauss Oersteds (MGOe) in CGS units or kilo Joule per cubic meter (kJ/m^3) in SI units. In addition, the maximum energy product illustrates the maximum amount of valuable work that a permanent magnet can supply to an external magnetic circuit. In broad terms, any measure of field that can be produced outside a unit volume of magnet materials is provided by $(BH)_{max}$. Therefore, the potential of reducing the weight and size of a device is proportional to the $(BH)_{max}$, where the higher value of $(BH)_{max}$, the larger the potential for reducing the weight and size of a machine [42].

One important characteristic which can affect the magnetic properties of materials is the Curie temperature. In many sophisticated devices such as aircraft, where ambient conditions are extreme, it is essential to consider the Curie temperature of the materials used. However, each type of magnet material has a temperature range which it can operate within. Fig 2.9 shows the effect of temperature on magnetic properties for a variety of permanent magnet materials.

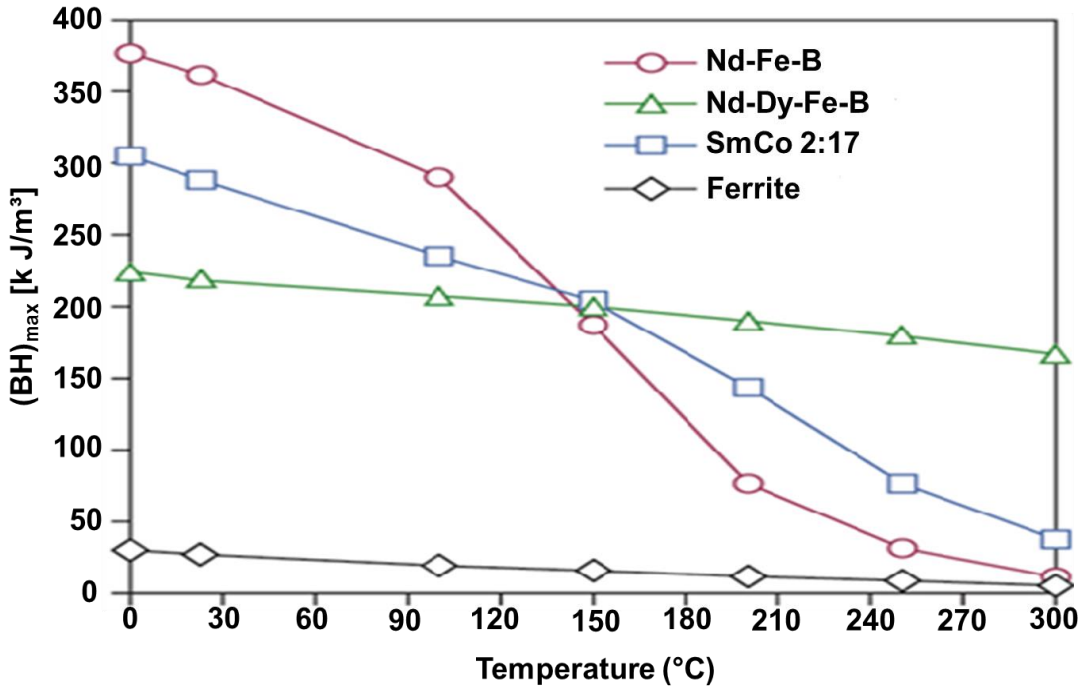

Figure 2-9 The temperature effect on magnetic properties for a variety of PM materials [1].

The behaviour of the hysteresis loop in permanent magnet materials is due to the variations in the magnetic domain structure, where the magnetic moments are aligned. Therefore, it is important to identify the coercivity mechanism of the materials, which is explained in the following section.

2.7 Magnetisation reversal and the coercivity mechanism

The coercivity or coercive field H_c is the reversal field required to reduce the remanence magnetisation (M_r) to zero in the second quadrant. It is the capability of ferromagnetic materials to resist the demagnetisation state. Usually, the demagnetisation field is generated from two actions: the heat by the operation temperature and magnetic or electric circuit. These two demagnetisation sources are continuously occurred in motor applications during operation. Therefore the coercivity is very important to be high in value. The higher coercivity value, the better magnet properties achieved for the motor. The ferromagnetic materials are categorised as either soft or hard depending on the coercivity value. A soft magnet needs a low field to reduce the remanence magnetisation to zero, whereas a high field is required to reduce the remanence to zero in hard magnetic materials.

The origin of coercivity is the energy barrier. There are two equal energy minima depending on the directions of magnetising reversal, which are metastable and stable

energy. The energy barrier exists between the two energy minima. Fig 2.10 illustrates the energy profile of a single grain. The energy required to form a new domain wall is described by the energy barrier. The energy barriers imply the magnetic anisotropy energy which related to the shape of the grains.

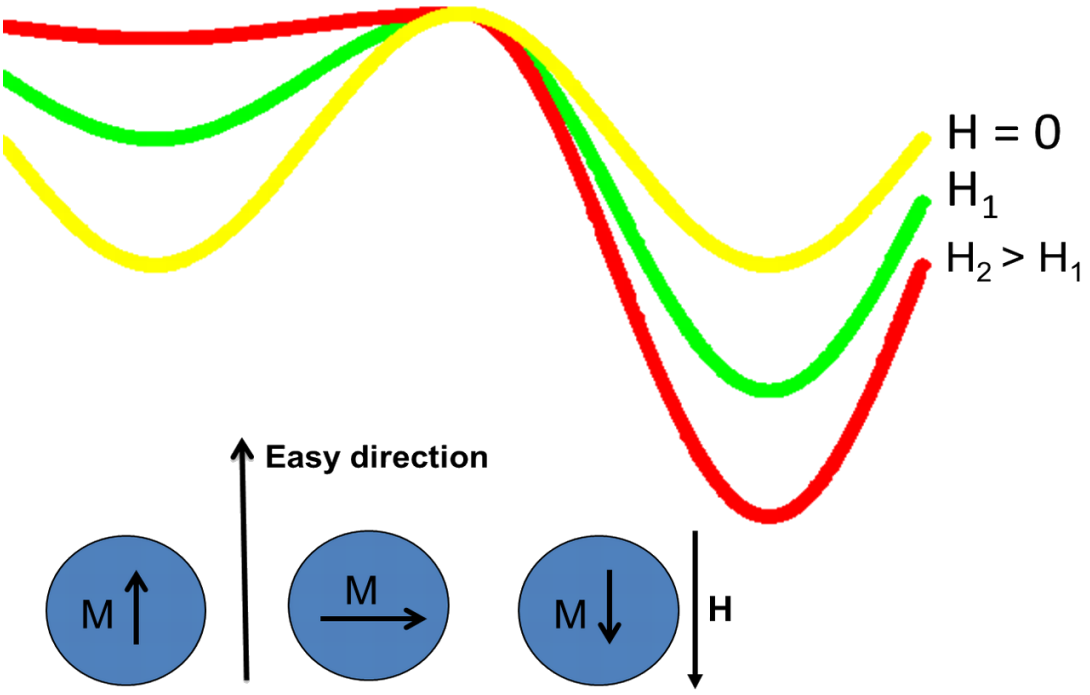

Figure 2-10 Energy profile and energy barrier for a magnet.

The coercivity in sintered permanent magnet materials such as SmCo and Nd-Fe-B is controlled by the magnetisation reversal of domains near the grain surface. Large numbers of grains reverse their magnetisation at the coercivity point H_c. The domain walls move across the grains because of the external applied field, which leads to magnetisation reversal. The reversal of magnetisation of hard magnetic materials is initiated in a small nucleation or pinning volume around a surface defect [43, 44].

2.8 Nucleation, pinning, and the role of defects

The main anisotropic phase and surface defects of sintered permanent magnets are sources of local magnetisation reversal, under the influence of a reverse applied field. The formation of reverse domains acts as nucleation regions in the centres of surface defects. The process of reverse magnetisation is divided into four steps: nucleation, passage, expansion, and pinning. In the nucleation stage, the domain walls and reverse domains are created and nucleated respectively. Following nucleation, the domain walls are passed from the defects to the main phase (passage), and expanded

into the main phase (expansion). After that, the domain walls are pinned on defects near grain boundaries. Fig. 2.11 shows the stages of magnetisation reversal involved in the second quadrant of the hysteresis loop. The domain walls may propagate outwards when the small nucleus is formed.

There are contrasting opinions concerning the impact of defects on coercivity. On the one hand, it has been stated by Woodcock *et al*. [2] that these defects lead to a decrease in the coercivity of the magnet because of the resulting distortion in the crystals. Hence, it was suggested that decreasing defects at the surface of $Nd_2Fe_{14}B$ grains will increase coercivity. However, on the other hand, it has also been stated [37] that these defects or imperfections are important for materials to obtain a large coercive field. During the magnetisation process, the moving domain walls intersect with imperfections such as defects or dislocations in the crystal. A large external field is required to pass the boundary across the defect. When the domain boundary moves past the defect, the formation of spike-like domains is generated. A schematic diagram of the formation of the spike domain has been given elsewhere [37] and is shown in Fig. 2.12.

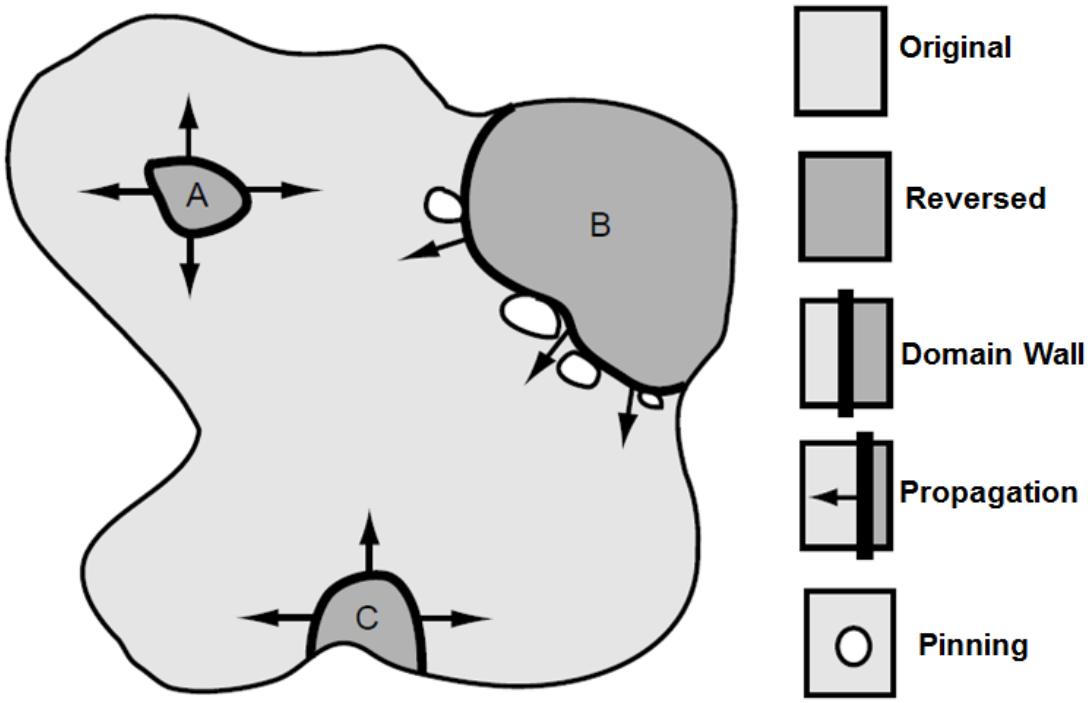

Figure 2-11 Stages involved in magnetisation reversal: (A) nucleation of the reverse domain at a defect; (B) reversal domain trapped by pinning centres; (c) nucleation of the reverse domain at surface asperity [45].

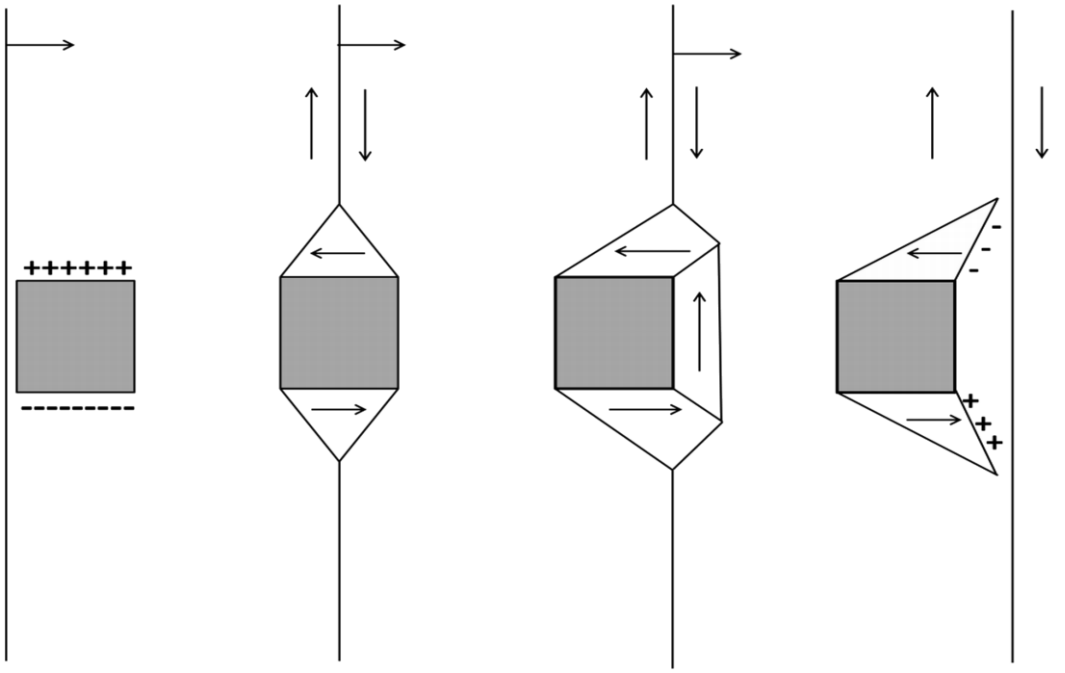

Figure 2-12 Schematic evaluation of the domain boundary moving past the defects which form spike domains.

When the magnetic field is removed at saturation, the reformation of the domain walls is resisted by the defect. The demagnetising field is not sufficient to overcome the energy barrier in order for the domain walls to reverse back to their original positions. The domain walls are incapable of fully inverting back to their original locations and an external field in the opposite direction is required to reduce the magnetisation to zero. As a result, the magnetisation curve of the materials shows large-area hysteresis loops with high remanence and large coercivity. Therefore, it is very important for hard magnetic materials to contain many defects or impurities in order to be used as permanent magnets.

2.9 Models of coercivity

The understanding of the coercivity mechanism relies on the theoretical analysis of the different processes of magnetisation reversal, due to the small size of the critical nucleus. Microstructure models have been developed in order to relate the magnetisation reversal to coercivity (H_c). The strong correlation between the nucleation of domains and coercivity in permanent magnet materials has rarely been discussed in the literature. The majority of recent studies rely on micromagnetic simulations to determine the magnetisation reversal process [24, 46-48].

Theoretically, in describing the relationship between reversal magnetisation and the coercivity of permanent magnet materials, two main models have been developed. One was proposed by Kronmüller [49] within the so called micromagnetic approach, and the other is a phenomenological (global) model suggested by Givord *et al*.[50]. Both models describe the defect mechanism and have the common weakness that they use the hard magnetic phase energy as the energy reference because the physical characteristics of the defects are unknown. The models are discussed in detail in the following sections.

2.9.1 Micromagnetic approach

The theoretical analysis of magnetisation processes in small grains always starts from Gibbs free energy Φ for uniaxial crystal:

$$\Phi=\int \{A_{ex} (\bigtriangledown\varphi(r))^2 + K_1 \sin^2\varphi(r) + K_2 \sin^4\varphi(r) - 1/2\ \mu_0 H_s(r) \cdot M_s(r) - \mu_0 H_{ex} \cdot M_s(r)\}\ d^3r \qquad (2.3)$$

where K_1,K_2 are the anisotropy constants, M_s is the spontaneous magnetisation, A_{ex} is the exchange coefficient, M(r) is the magnetisation vector, φ(r) is the angle between the c-axis of the grain and $M_s(r)$, and $H_s(r)$ is the field of magnetic dipolar.

Then the micromagnetic equilibrium equations are obtained from the calculation $\delta_\varphi\Phi = 0$ with respect to the angle φ, leading to:

$$2\ A_{ex} (\bigtriangledown\varphi(r)^2 - 2K_1 \sin\varphi(r) \cos\varphi(r) - 4K_2 \sin^3\varphi(r) \cos\varphi(r) + \mu_0 H_{ex} M_s \sin[\theta_{cH} - \varphi(r)] + \mu_0 H_s M_s \sin[\theta_{cH} - \varphi(r)] = 0 \qquad (2.4)$$

The micromagnetic model was developed by Kronmüller [49] from the solution of equation 2.2. In this model, the shape of the defect is assumed to be quasi-harmonic inhomogeneity. A planar region of half width r_0 is considered as shown in Fig. 2.13, where the spatial form is followed by anisotropy.

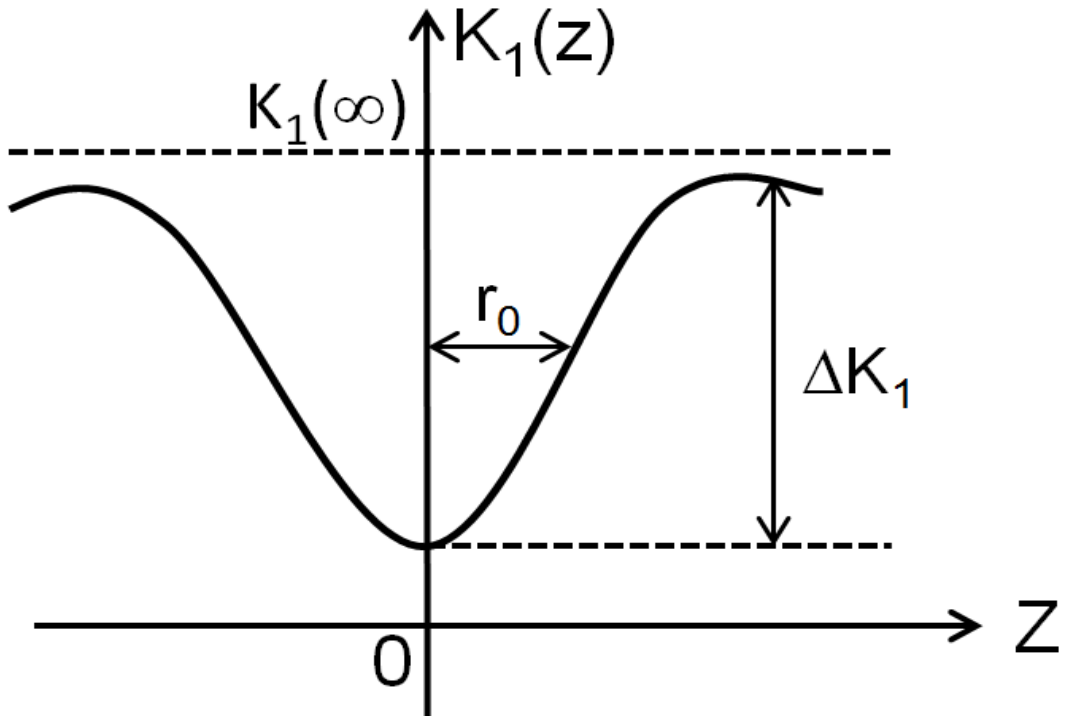

Figure 2-13 Schematic representation of a quasi-harmonic defect [49].

When the field is applied in the opposite direction, equation 2.2 is solved with K_2=0, as:

$$H_c = \frac{2K_1}{\mu_0 M_S}\alpha_\Psi \alpha_K - N_{eff} M_S = H_N - N_{eff} M_S \tag{2.5}$$

Here, α_K is the microstructural parameter given by:

$$\alpha_K(r_0) = 1 - \frac{1}{4\pi^2}\frac{\delta_B'^2}{r_0^2}\left[1 - \sqrt{(1 + \frac{4\pi^2 r_0^2}{\delta_B'^2})}\right]^2 \tag{2.6}$$

where: $\delta_B' = \pi\sqrt{(A_{ex}/\Delta K_1)}$

And α_Ψ describes the misalignment parameter of grains and was determined by Stoner-Wohlfarth [51] as:

$$\alpha_\Psi = \frac{1}{(\cos^{2/3}\Psi + \sin^{2/3}\Psi)^{3/2}}\left(1 + \frac{2K_2}{K_1 + K_d}\frac{\tan^{2/3}\Psi}{1 + \tan^{2/3}\Psi}\right) \tag{2.7}$$

where: $K_d = \frac{1}{2}(N_\perp - N_{//})\mu_0 M_s^2$, is the coefficient of the shape anisotropy field.

2.9.2 Phenomenological approach

In parallel with the micromagnetic model, the phenomenological (global) model was developed by Givord *et al*. [50]. The approach describes the behaviour of coercivity for hard magnetic materials and links the intrinsic microstructural properties with extrinsic properties. The global approach is based on the fact that the same energy terms are mainly involved in all magnetisation reversal processes. It is assumed that the formation of a small nucleation (with activation volume (v)) is initiated with the reverse magnetisation which induces the complete reversal. Therefore, the volume of the nucleus (v) appears in the expression for the coercive field, and is assumed to be equal to the activation volume (v_a) which can be evaluated experimentally. The effects of thermal activation are considered in this model.

The coercivity field was expressed as:

$$H_c = \alpha \frac{\gamma_w}{\mu_0 M_s \nu^{1/3}} - N_{eff} M_s - 25 \frac{kT}{\mu_0 M_s \nu} \tag{2.8}$$

The parameters α and N_{eff} represent the nature and dipolar interactions respectively in the nucleus, and they are purely phenomenological parameters. γ_w is the domain wall energy and M_s is the magnetisation saturation. The reversed nucleus volume (v) is an important feature of this model.

The first term of the expression represents the effect of defects on reversal magnetisation, whereas the second term describes dipolar interactions. The third term is the magnetic viscosity, $S_v = kT/\mu_0 M_s \nu$ realized from after-effect measurements.

The global model has been used to analyse the coercivity of sintered SmCo magnet [52], and a good fit was obtained. However, it has been recommended to use the global model for comparing the temperature dependence of coercivity to the intrinsic physical parameters of hard magnetic materials [53].

The global model relates the energy barrier to the domain wall energy, whereas the microstructure model relates the barrier to the anisotropy energy.

2.9.3 Magnetic viscosity

The phenomenon of magnetic viscosity is found to delay the reverse magnetisation in the second quadrant of hysteresis loop. The combination of thermal activation and the field induced during the demagnetisation process converts the magnetic materials form the metastable states of energy to stable ones [54]. The magnetic viscosity can be detected in a steady reverse field state near the coercivity point H_c, and results from the fact that thermal activation may overcome the barrier energy of coercivity. Magnetic viscosity is a time-dependent occurrence and relies on the waiting time to pass the barrier. Gaunt [55], Wohlfarth [56], and Givord [50] have expressed viscosity as:

$$S_v = kT/\mu_0 M_s \nu \tag{2.11}$$

where kT is the temperature dependence (temperature T and Boltzmann's constant k).

The magnetic viscosity (S_v) for Nd-Fe-B magnets has been found to be unchangeable at a constant temperature and independent of the magnetic field [57, 58]. Generally, in higher coercivity materials such as sintered Nd-Fe-B and SmCo, the magnetic viscosity is more explicit [59].

2.10 Measurements of the main domain width and domain wall energy

Knowledge of domain width (D_w) is one of the most significant parameters in the identification of the magnetic domain structure of the materials. Microstructural variables such as grain size and phase morphology have a strong influence on coercivity and remanence. The coercivity (H_c) of a magnetic material varies inversely with grain size (D) [25]. From the global model expression (equation 2.6) the coercivity of permanent magnet materials is influenced by domain wall energy (γ_w). The domain wall energy and exchange constant of materials are calculated from the measurement of domain width. However, a strong correlation between domain width and coercivity has not been discussed in the literature so far.

It is not easy to determine using visual methods the domain width in materials such as the Nd-Fe-B magnet which have complicated domain patterns. Therefore, a digital method has been applied to obtain the main domain width.

In general, an effective domain width can be defined using the ratio between an area and the integrated wall length in this area, as shown in Fig. 2.14. One procedure for evaluating the domain width is based on the stereological method proposed by Rudolf and Hubert [60, 61]. In this method, the intersections of the domain walls with arbitrary test lines are counted and evaluated. According to Rudolf and Hubert, the domain width D_w is determined using the following formula:

$$D_W = \left(\frac{2}{\pi}\right) \times \left(\sum_i l_i\right) / \left(\sum_i n_i\right) \tag{2.9}$$

where l_i is the length of the i^{th} test line and n_i is the number of intersections of the i^{th} test line with the domain walls.

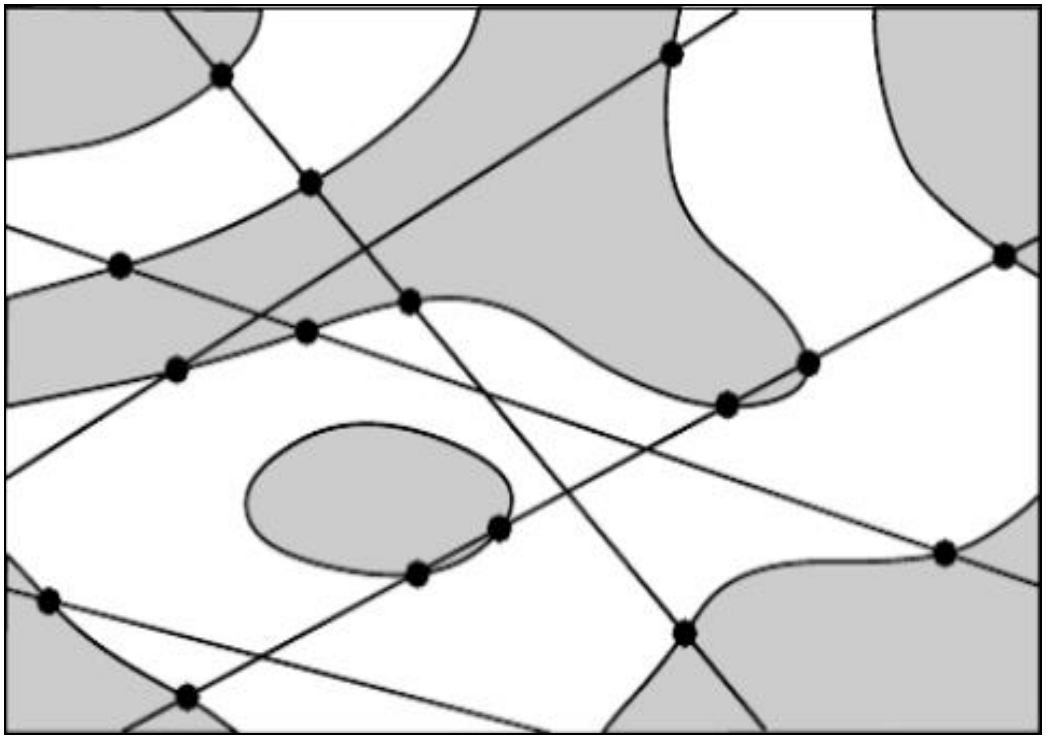

Figure 2-14 Determination of domain width based on the stereological method: the intersections of the domain walls with arbitrary test lines are counted and evaluated.

The stereological method has been applied successfully for measuring the domain width by Szmaja [40, 62]. It has been stated that, to determine the position of domain walls, the observed images are transferred to black and white images using digital imaging procedures such as a thresholding technique and median filter.

In addition, the main parameter related to the coercivity mechanism is the domain wall energy (γ_w). The domain wall energy depends mainly on exchange and

magnetic anisotropy energies. Domain wall energy (γ_w) can be evaluated according to the model proposed by Bodenberger and Hubert [61] from the expression

$$\gamma_w = \frac{D_w (M_s)^2}{4\pi\beta} \tag{2.10}$$

where D_w is the determined domain width and M_s is the magnetisation saturation of the magnet. β is a coefficient depending on the surface structure and its value has been previously determined as 0.31 for $SmCo_5$ and similar magnetic materials with high magnetocrystalline anisotropy [61].

2.11 Previous work in the effect of microstructure on domain walls and coercivity

The extrinsic magnetic properties of the magnet (coercivity and remanence) are controlled by the microstructural variables of magnet such as grain shape, grain size, grain boundary, and phase morphology.

It is known experimentally that the coercivity (H_c) of a magnetic material varies inversely with grain size (D) [25, 63-65]. However, Li *et al.* [66] proved that the coercivity is reduced in small grain size below 3μm because of the oxidation of Nd-rich phases. It has been demonstrated that the non-ferromagnetic Nd-rich phases between $Nd_2Fe_{14}B$ grains and at triple junctions have a great impact on the coercivity of sintered magnet. The exchange magnetic interaction between $Nd_2Fe_{14}B$ grains can be effectively decoupled using a layer of Nd-rich phase. The Nd-rich layer will block the movement of domain walls. Therefore, the uniform distribution of Nd-rich is highly important for the process of demagnetisation and magnetisation of the Nd-Fe-B magnet. However, the defects are mainly generated from the non-uniform distribution of Nd-rich phases during the annealing process [7, 67]. The Nd-rich phase prevent the propagation of reversal domains. Therefore, the distribution of Nd-rich phases in the microstructure of a sintered Nd-Fe-B magnet is a critical concern for coercivity.

Schematically, the contribution of microstructure towards coercivity is mainly from the thin and large layers of Nd-rich phases [2]. The thin Nd-rich layers at $Nd_2F_{14}B$ grain boundary are metallic in character. They tend to separate the $Nd_2F_{14}B$ grains with respect to the magnetic interactions and act to reduce defects on the surface. The large and more rounded Nd-rich regions at triple junctions are usually oxides in

character and the interface with the $Nd_2Fe_{14}B$ phase is different to the case of metallic character. However, it has been stated that lager oxide layers of Nd-rich phases at triple junction is rarely studied comparing to the thin layers [2].

Ono *et al*. [68] found that ferromagnetism is weak at the Nd-rich triple junctions. The authors suggested that, when an external field is applied, the reverse domains may appear as nucleation sites in these regions. Furthermore, Goto *et al.* [7] stated that, at low reverse magnetic fields, the reverse magnetic domains appear when some defects are found on the surface of the $Nd_2Fe_{14}B$ grains. The presence of interfacial defects is expected to decrease the anisotropy of the $Nd_2Fe_{14}B$ phase, and in addition interaction and exchange significantly change at these defect regions. Hrkac *et al* [69, 70] proved that the distorted sites at the grain boundary lead to a decrease in the magnetic anisotropy of the main phase. The large distortion is expected to be from the oxide Nd_2O_3. The authors suggested that the removing the Nd_2O_3 phases from the microstructure could lead to produce a high coercivity magnet.

In addition, from the phenomenological model explained earlier (equation 2.8), the coercivity of permanent magnet materials is influenced by domain wall energy (γ_w). The domain wall energy and exchange constant of materials are calculated from the measurement of domain width. However, a strong correlation between domain width and coercivity has not been discussed in the literature so far.

The segregation of the magnetic domains at grain boundaries is an important concern in the development of high coercivity magnets. However, it is difficult to experimentally analyse the influence of the microstructure of grain boundary on coercivity; instead simulations are conducted to describe the relevant correlations. The practical coercivity H_c is limited to only 20%–30% of the theoretical maximum, which is the anisotropy field H_A, also known as Brown's paradox [71]. This is due to the reverse domains at nucleation regions which occur at lower magnetic fields than the anisotropy field.

From all previous research in the microstructure, it can be confirmed that the Nd-rich phases between grain boundaries and at triple junctions play a crucial role in the coercivity mechanism. The Nd-rich phases have a great impact on the domain wall movement. It is vital to understand the effect of Nd-rich phases on the domain wall and the possibility of improving the coercivity. Hence the aim of this thesis is to study the impact of Nd-rich phases at triple junctions on the domain wall size. In

addition, study the dynamic behaviour of domain walls at different temperature is very important to understand the coercivity mechanism. Next section will describe the previous study of domain wall movement for sintered Nd-Fe-B magnet, under different conditions such as high temperature.

2.12 Previous work in the thermal analysis of magnetic microstructure of Nd-Fe-B magnet

Most of the applications for sintered Nd-Fe-B magnets, such as the motors in hybrid and electric vehicles, are operating at high temperature around T=450K. Usually, the magnetic properties of magnet materials deteriorate with the increase of operating temperature. The coercivity mechanism is closely related to the dynamic behaviour of magnetic domains, such as domain wall interactions and magnetisation reversal. The magnetocrystalline anisotropy, which is the source of coercivity, reduces with the increase of temperature. Therefore it is vital to understand the dynamic behaviour of magnetic domains at high temperature. There are high demands from both industry and academia to develop Dy-free Nd-Fe-B magnet operating at high temperature.

Takezawa *et al.* [9] reported the observations of magnetic domains using a Kerr microscopy at elevated temperature for sintered Nd-Fe-B magnet. The temperature was applied up to 150°C. The authors confirmed that the reversal domains grow with the increase of temperature. It was stated that the magnetocrystalline anisotropy decreases with temperature, which deteriorate the magnetic properties of sintered Nd-Fe-B magnet.

Yamaoka *et al.* in 2014 [72] proved the observations of magnetic domains for sintered Nd-Fe-B magnet at high temperature using vacuum MFM technique. The temperature was applied up to 200°C in vacuum MFM chamber. The authors confirmed the observation of multi-domain structures for each grain as shown in Fig. 2.15. The figure shows the appearance of multi domains in each grain in the form of maze-like patterns. Yamaoka *et al.* concluded that the number of grains, which have a multi-domain structure, increases with the temperature, and the multi-domain patterns change from one grain to another. However, the observations of reversal magnetisation and the movement of domain walls for sintered Nd-Fe-B magnet were not stated in this reference.

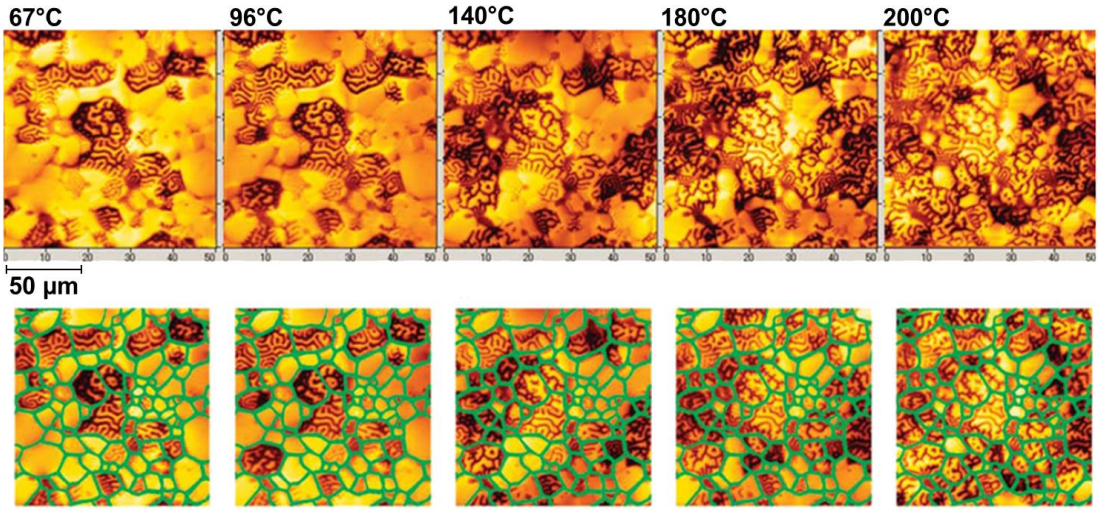

Figure 2-15 In-situ MFM images of sintered Nd-Fe-B magnet observed at high temperature [72].

Fang *et al* in 2016 [73] estimated the appearance of reversal magnetisation of die-upset Nd-Fe-B magnet at high temperature using MFM technique. It was demonstrated that the reverse domains start to nucleate when the temperature rise up to 80°C and grow as the temperature increase. The temperature was applied below 120°C and the MFM observations were made in-situ. The authors concluded that the reverse domains initiate originally from small surface nucleus, and there are more than one nucleus appears on the surface of die-upset Nd-Fe-B magnet.

However the impact of grain separation on the domain wall size at room and high temperature has not been observed using MFM technique for sintered Nd-Fe-B magnet. Therefore, it is proposed in this work to observe the effect of Nd-rich regions on the domain wall of sintered Nd-Fe-B magnets using MFM technique at room and elevated temperature.

2.13 Summary

In this chapter a literature survey has been conducted in the field of permanent magnet materials, in terms of magnetic properties; microstructural analysis; the magnetisation process; and commercially available types of PM materials. It is apparent that rare earth magnet materials have been the preferred choice of materials in many applications. The high demand and expected supply shortages, however have led to a significant increase in the prices of rare earth magnet materials. Therefore, the issues associated with today's rare earth supply need to be addressed in more depth. In this context, more research is being conducted to understand the microstructural analysis of materials in greater detail.

The crystal and domain structure of sintered Nd-Fe-B magnets have been chosen to be described in detail, because this type of magnet is used in many of today's technologies. Each grain of sintered Nd-Fe-B magnet consists of a multi-domain structure in the demagnetised state. Generally, the crystal structure of sintered Nd-Fe-B magnets comprises mainly of a hard magnetic $Nd_2Fe_{14}B$ matrix surrounded by Nd-rich phase. However, the Nd-rich phases appear in thin and large layers between the grains and at triple junctions, respectively. The large layers of Nd-rich phases are oxides in character, whereas the thin layer are metallic in character. The thin Nd-rich phases prevent the propagation of reversal domains and decouple the exchange magnetic interaction between $Nd_2Fe_{14}B$ grains. The larger layers (Nd-oxides) interface with the $Nd_2Fe_{14}B$ phase in a different way to the thin layers (Nd-metallic). It has been stated that the segregation of the magnetic domains at grain boundaries is an important concern in developing high coercivity magnets.

In this review, more attention was focused on microstructural analysis and coercivity of sintered Nd-Fe-B magnet materials, which closely relate to the aims of this thesis. Previous research has shown that studying the microstructure of magnets in terms of grain boundary isolation and magnetisation reversal is vital for developing high coercivity magnets. In this context, it is stated that the coercivity of sintered permanent magnet materials such as SmCo and Nd-Fe-B is controlled by the microstructural parameters of magnet such as grain shape, grain size, grain boundary, and phase morphology. From all previous research in the microstructure, it can be confirmed that the Nd-rich phases between grain boundaries and at triple junctions play a crucial role in the coercivity mechanism. The Nd-rich phases have a great impact on the domain wall movement. Hence the aim of this thesis is to study the impact of Nd-rich phases at triple junctions on the domain wall size at room and high temperate. Therefore, it is suggested that magnetic force microscopy (MFM) should be used to study the structure of grain separation of sintered permanent materials and to correlate it with domain wall, since; the MFM has a high resolution.

CHAPTER 3 DESCRIPTION AND DEVELOPMENT OF LOCAL CHARACTERISATION METHODS AND SAMPLE PREPARATION

3.1 Introduction

This chapter considers the local characterisation techniques employed in this research in terms of basic principles and the process developed. The samples used are discussed in detail, including their magnetic properties and surface preparation requirements. The sample preparation procedure is explained, from sectioning and mounting to grinding and polishing. A brief review of magnetic force microscopy as a main technique is presented in terms of operation, main parts, and the settings for local MFM measurements. The MFM mode is installed successively on the AFM system, and tested on a controlled sample.

In addition, the structural and microstructural methods used are reviewed. These techniques are utilized for the analysis of the grain structure and chemical composition of the magnets. The MFM images are enhanced using digital imaging process software to produce images that are readable using Matlab. The digital imaging software is explained along with the procedure involved. Models developed using Matlab are discussed. The models are used for the determination of main domain width and domain wall energy.

3.2 Sample preparation and equipment

The sample surface for most modern permanent magnet materials has to be well-prepared before recording any images using magnetic force microscopy (MFM).

Szmaja *et al.* reported that, in order to reduce the topographic contrast and effectively enhance the magnetic domain contrast, the sample has to be carefully polished [40, 74-76]. He used successively finer SiC abrasive papers (down to 1200 grades) and diamond powders (3, 1 and 0.25 μm in average diameter) with a water-free lubricant. It has been stated that polishing modern bulk permanent magnets presents a difficulty due to the fact that they are multiphase and mechanically anisotropic, have high hardness and some inter-granular constituents are chemically very reactive.

Folks *et al.* stated that it is essential for good imaging to first obtain a flat surface [39, 77]. This is achieved by using metallurgical polishing with diamond films and SiC paper, resulting in samples with a peak-to-valley roughness of the order of tens of nano-metres over scales of several micro-metres. The samples should be mounted in epoxy resin and polished using diamond paste (15, 6, 3 and 1 μm) with a water free lubricant (ethanol). It has been emphasised that one of the difficulties of polishing hard magnetic materials is that the material removed during polishing tends to adhere to the surface magnetically, and this must be carefully removed in each step before changing to lower diamond film grades. Therefore an adhesive fine silicon paper needs to be used.

In addition, Thielsch *et al*. [78] reported that the surface of the sample has to be well-prepared, and that standard metallographic techniques should be used to polish the sample. Furthermore, Al-Khafaji *et al.* revealed that the sample has to be well-prepared before taking any image, and it was prepared by grinding on successfully finer SiC paper down to 1200 grade, followed by polishing on diamond-impregnated wheels down to 0.25 μm [79]. Therefore, the samples have to be well-prepared before any further step in order to obtain good images by reducing topographic contrasts.

The standard metallographic techniques for preparing the samples are discussed in detail in the following sections, along with the samples used in this study.

3.2.1 Samples and magnetic properties

In this study, five different types of sintered permanent magnet materials are studied;

- A commercially available sintered Nd-Fe-B magnet grade N42 supplied from the First4magnets Company in a cuboid shape of size $10\times8\times21 mm^3$ (L×W×H). The magnet is axially magnetised between the two 10×8 mm rectangular faces.
- Four different types of sintered SmCo-type magnets are investigated. They are on batch sintered $SmCo_5$ magnet and a selection of three different sintered $Sm_2(Co,Cu,Fe,Zr)_{17}$ magnets. The $Sm_2(Co,Cu,Fe,Zr)_{17}$ samples (A, B and C) have been prepared using different processing routes. Sample A is the standard Sm_2Co_{17} while specimens B and C have been annealed at different annealing temperatures. The SmCo magnets were supplied by Birmingham University for the investigation using the MFM method.

The measured magnetic properties for each sample of sintered SmCo in terms of coercivity H_c and magnetisation saturation M_s are shown in table 3.1.

Table 3-1 Magnetic properties of each SmCo magnet material studied.

Type	ID	M_s(T)	H_c (k A/m)
$SmCo_5$	R22	1	750
Sm_2Co_{17} (A)	HE- Standard	1.2	780
Sm_2Co_{17}(B)	He-LM	1.1	560
Sm_2Co_{17}(C)	HTA	1.3	865

Recently, Périgo *et al* [27] measured the magnetic properties of N42 grade sintered Nd-Fe-B using a vibrating sample magnetometer (VSM). According to the authors, the magnet has a coercivity H_c of 1058 kA/m, magnetisation saturation M_s of 1.44T, remanence B_r of 0.68T, and maximum energy density (BH) max= 75 k J/m^3. Fig. 3.1 shows the magnetic properties of N42 grade sintered NdFeB magnet measured using VSM.

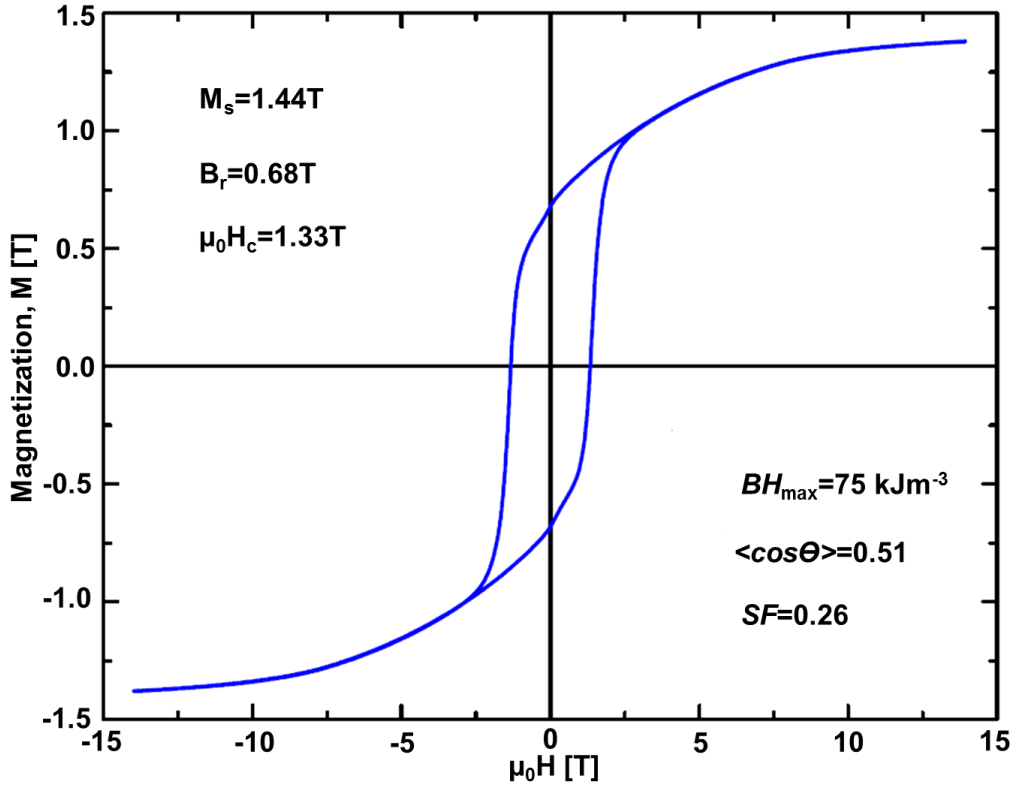

Figure 3-1 Magnetic properties of sintered Nd-Fe-B magnet grade N42 (T=300K) [27].

3.2.2 Preparation requirements

The samples are prepared prior to examination using magnetic force microscopy (MFM). The following items are required for preparing the hard magnetic materials proposed:

- Silicon carbide abrasive paper, with different grades (120, 180, 240, 320, 400, 600, 800 and 1200 grade). These are designed for metallographic applications to coarse and fine grind for a wide variety of materials.
- Diamond compound, Polycrystalline, of different sizes (14, 10, 7, 5, 3.5, 2.5, 1, 0.5 and 0.25 microns) for polishing the surface in order for it to be very smooth. This is an abrasive polishing paste and is specifically formulated for metallographic sample preparation, offering a higher concentration of diamond compared with suspensions.
- Water-free lubricant (ethanol-based). This lubricant is excellent for increased stock removal and is used to enhance the polishing performance of diamond suspensions, compounds, sprays and films. Also, isopropanol and distilled water are used for washing the surface.
- Grinding and polishing machine, shown in Fig. 3.2. The machine consists of two rotating wheels. These wheels rotate of approximately 150 rpm. One of the wheels is used for grinding and the other for polishing.
- Plastic moulds and epoxy resin (Araldite Standard) to mount the samples.

Figure 3-2 Grinding and polishing machine used for preparing the samples.

3.2.3 Sectioning and mounting

The samples are sliced into two sections from the side and top view, in order to investigate the magnet from two orientations, with the initial magnetisation direction parallel and perpendicular respectively to the alignment axis.

The sintered Nd-Fe-B magnet is mounted using cold moulding with epoxy and a plastic mould as shown in Fig. 3.3. The plastic mould is cut and prepared to be suitable for the samples. The samples are positioned face down in the cold-mounting ring, then the epoxy is mixed and poured over the samples. After six hours, the samples are removed from the mounting ring. The small and large sections relate to the perpendicular and parallel alignments respectively.

Figure 3-3 Mounting equipment and procedure.

The SmCo magnets have been sliced into sections and mounted in conducting Bakelite in two orientations, with the initial magnetisation directions parallel and perpendicular to the surface. They have been supplied by Birmingham University in a well-prepared state

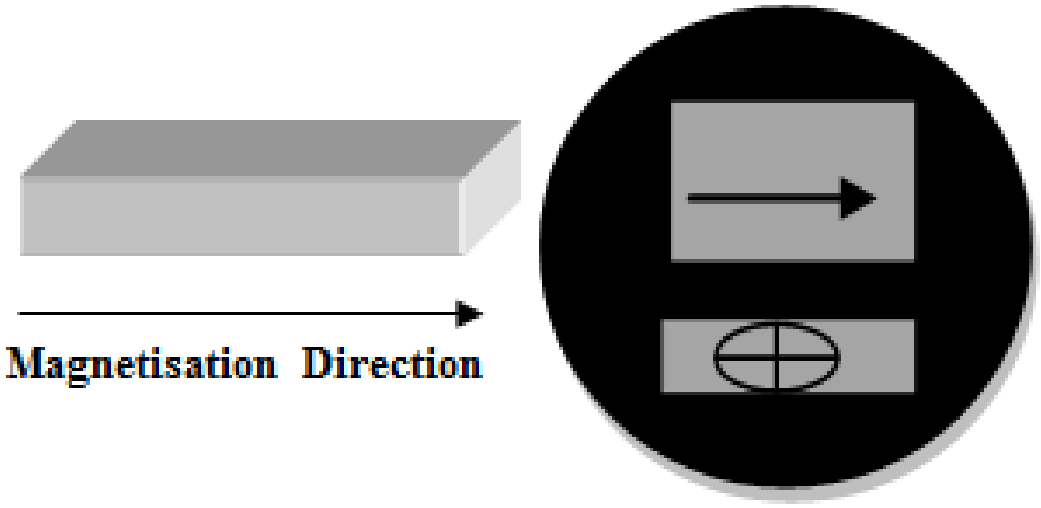

Figure 3-4 Magnetisation direction of the sample (left) and the mounted samples (right).

The initial magnetisation direction of the samples can be seen in Fig. 3.4 which shows how the samples were mounted. All the MFM images obtained refer to the smaller and larger sections for each sample. The smaller section has the initial magnetisation direction perpendicular to the alignment axis of the surface (top view of the surface). The larger section has the magnetisation direction parallel to the alignment axis of the surface (side view of the surface).

3.2.4 Grinding and polishing

The surface is ground in two stages: coarse and medium or fine grinding. The coarse stage generates the initial flat surface for the following grinding and polishing steps. The coarse grinding is accomplished using different silicon carbide papers down to 240 grit (80, 120, 240 grit) fixed in one of the wheels. Next, the medium and fine grinding produce a surface free from scratches and smooth. The latter is achieved using silicon carbide papers fixed in one of the wheels in decreasing grades from 240 to 1500 grit (240, 400, 600, 800, 1000, 1200 and 1500 grit). Some drops of cold water are applied during the grinding process to avoid the side effect of heating produced by the grinding. The sample is carefully washed and dried at each step and after the final fine grinding step before starting the polishing stage.

3.3 Magnetic characterisation methods

The main interest for fundamental and applied research into these magnets is the understanding of the magnetic microstructure of materials. From the fundamental viewpoint, observing the magnetic domain structure of magnetic materials can be

useful in understanding the intrinsic parameters and microscopic properties of the materials. One important key for understanding and improving the coercivity of materials is to investigate their magnetic microstructure.

The observation of the structure of micromagnetic domains and magnetisation reversal is the main purpose of this work in order to understand the coercivity mechanism. The most widely used method for analysing and imaging the domain structure of the materials is magnetic force microscopy (MFM) [77, 80]. In the following sections, the literature on the MFM is briefly described by considering the operation and the main parts of MFM. In addition, a capacitive discharge magnetiser is used for magnetizing the samples, and this is discussed in detail.

3.3.1 Magnetic Force Microscope (MFM)

Magnetic force microscopy (MFM) is a special operational mode of the atomic force microscope (AFM). The MFM was first introduced by Martin and Wickramasinghe in 1987 shortly after the invention of AFM [81]. They improved the AFM to investigate the magnetic properties of surfaces with submicron spatial resolution. It was proposed that the magnetic force can be measured using a micro-needle made of ferromagnetic materials as a probing tip to the AFM. Since 1990s, MFM has been widely used in the fundamental research of magnetic properties of materials.

Magnetic domains can be observed using a variety of techniques [60], and among these methods is magnetic force microscopy MFM [81]. MFM is based on the magnetostatic interaction or force gradients between a magnetic tip and the magnetic specimen. Various investigations of hard and soft magnetic samples have been analysed using the MFM technique [4, 77, 82-84]. However, this technique has never been employed to study the nucleation regions of permanent magnet materials. Detailed explanations of the basic principles of MFM and local MFM settings are discussed next.

3.3.1.1 Basic principles of MFM

The basic principle of MFM is the same as that of AFM. A special flexible MFM cantilever probe vibrates close to its resonant frequency at a constant height above the sample surface. A schematic diagram for the principle of MFM is shown in Fig. 3.5. The tip scans the sample surface in non-contact mode. The properties of the

sample surface are magnetic and the interaction force is the magnetic force between the magnetised tip and the magnetic sample. The cantilever is deflected by repulsive or attractive forces, depending on the tip-sample distance. The cantilever deflection is measured by a focused laser beam on the back side of the cantilever. The laser beam is redirected towards a position sensitive photo-detector (PSPD). This detector comprises of four photodiodes positioned in four quadrants A–D. The vertical information is provided by the (A+C) − (B+D) signal, whereas the (A+B) − (C+D) signal generates the lateral information. An electronic controller receives the information form the PSPD. Two separate scanners (X-Y scanner and Z-scanner) control the movement of the sample and tip.

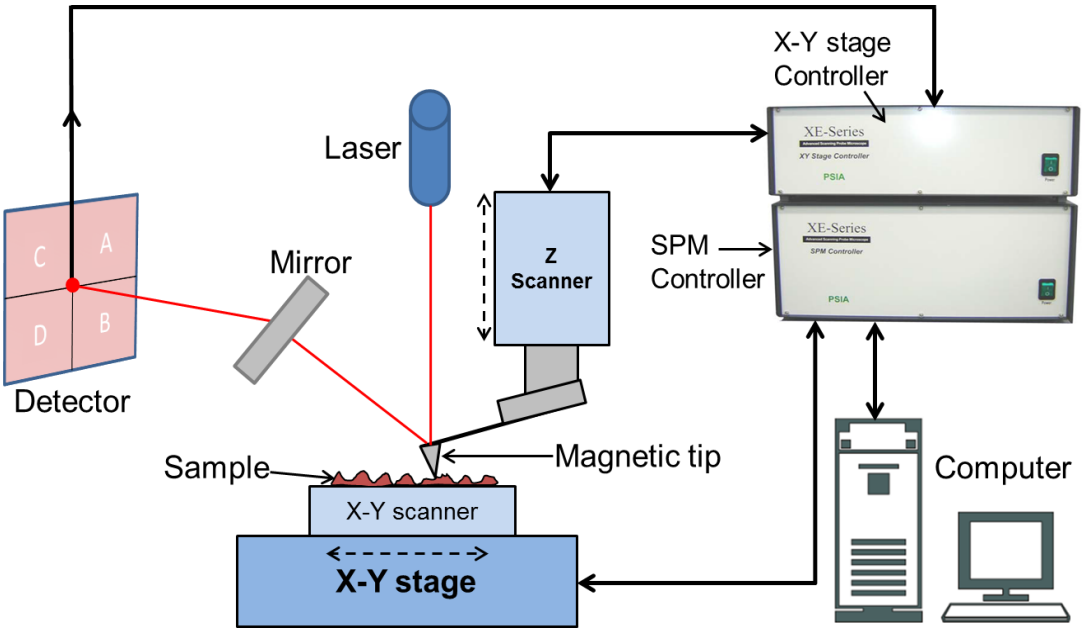

Figure 3-5 System diagram of the magnetic force microscopy (MFM).

The resulting interaction between the surface magnetic field and the magnetised tip produces an image of the magnetic field gradient, independent of the surface topography. However, in addition to the magnetic force, Van der Waals forces always exist between the tip and the sample. The Van der Waals forces vary according to the tip-sample distance and are used to measure the topography of the surface. During the MFM imaging process, the magnetic and Van der Waal's forces act on the tip. These two types of forces generate a signal that contains information about both the surface topography (Topo. signal) from the Van der Waals forces, and surface magnetic properties resulting from the magnetic force (MFM signal). The

two forces are affected by the tip-sample separation; the magnetic force perseveres for a greater tip-sample distance than do the Van der Waals force.

In addition, information about the magnetic domain distribution is generated from the MFM images on the sample surface. However, the key factor for a successful MFM image depends on the separation of the magnetic signal from the whole signal. This can be achieved using a two-pass technique or lift mode.

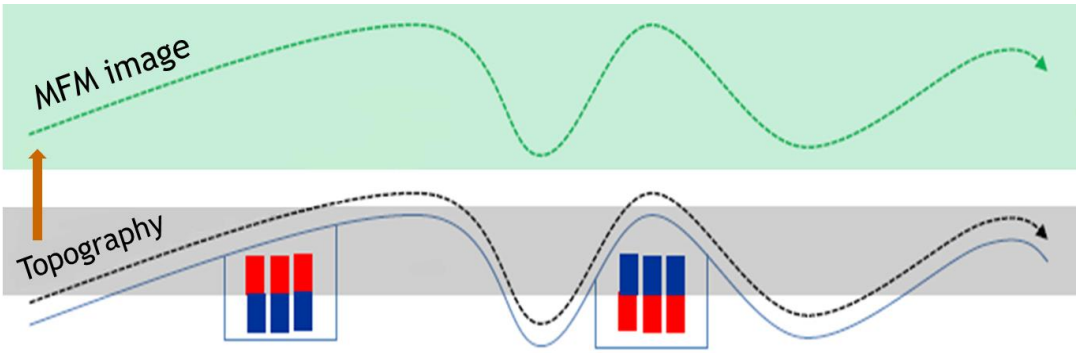

Figure 3-6 Schematic of the two-pass technique and scanning procedure of MFM

The MFM measurements are carried out in the lift mode regime with a two-pass scanning technique as shown in Fig. 3.6. At first the sample is scanned in true non-contact mode at a close tip-sample distance (trace-retrace) with a constant drive frequency and amplitude. The oscillation amplitude of the probe is kept at the same level during scanning by adjusting the distance between the tip and sample surface. These measurements generate a topography line with any misalignment and tilt on the surface, giving a topographic image of the sample. In the second scan, the magnetic force image is determined, during which the tip is lifted vertically at a higher distance from the first pass (100 nm in this case) and scanned along the same path as the first topography line at fixed frequency and amplitude. The oscillation phase and amplitude of the cantilever are revealed as MFM images with a different contrast. As the tip is repulsed or attracted by the magnetic force of the sample, the resonant frequency of the cantilever changes and leads to variations in image contrast. Therefore, the contrast in the MFM image is directly proportional to the magnetisation of the sample surface.

3.3.1.2 Setting of local MFM measurements

MFM analysis is performed using an XE-150 AFM in MFM mode at room temperature as shown in Fig. 3.7. The MFM mode is ordered and successfully

installed. A silicon cantilever (PPP-MFMR probes by Park System Corporation) is used to record the images. The cantilever is coated with a hard magnetic coating (≈ 50 nm thick) to avoid switch polarisation [79, 80]. The probe has a coercivity of almost 400 Oe; tip radius of 38 nm; resonance frequency of 200-400 kHz; and force constant of 25-75 Nm^{-1}. A special magnetiser is used to magnetise the tip before each experiment in a direction perpendicular to the specimen surface, as shown in Fig. 3.8. A non-magnetic sample holder is used to mount the sample under investigation.

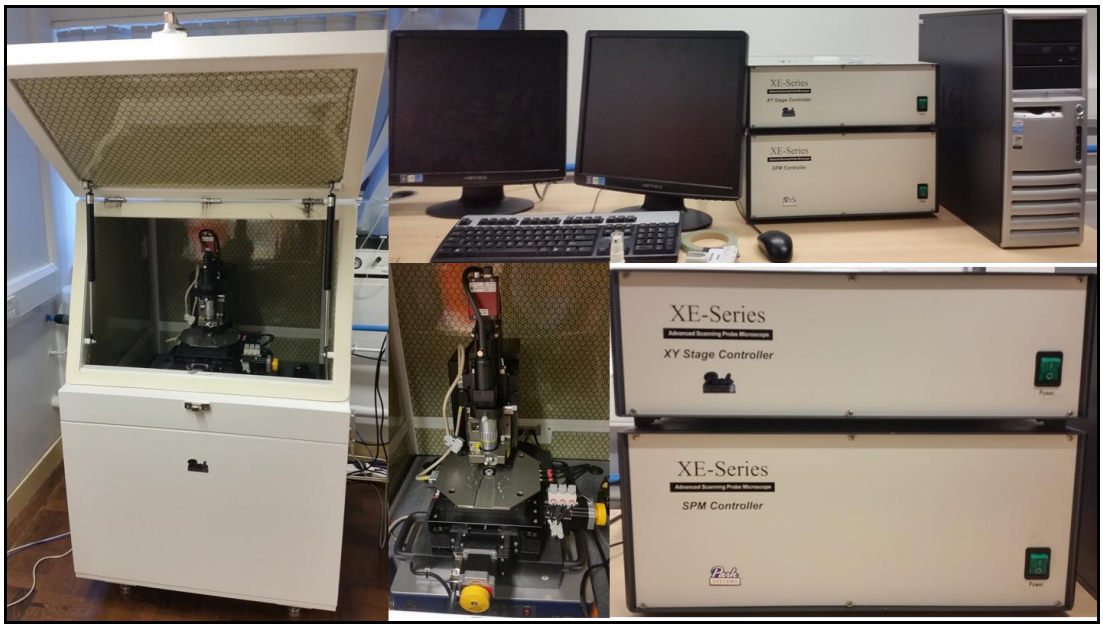

Figure 3-7 Atomic force microscopy (AFM) working in MFM mode used as a main method for the analysis in this study.

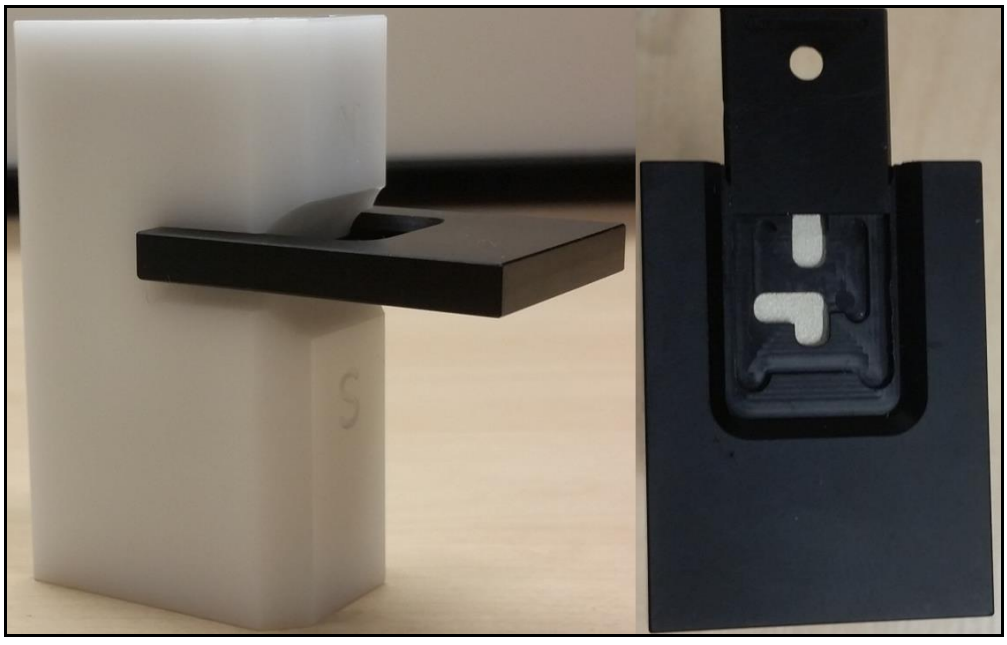

Figure 3-8 Special magnetiser and magnetiser clip to magnetise the tip.

The MFM measurement system is controlled using a multimode scanning probe microscopy (SPM) controller adopted with a stage controller designed specifically for the XE-150 AFM. The stage controller has two independent scanners: an X-Y scanner scans the sample in two-dimensional space, and the z-scanner moves the tip in the z direction. The Z scanner is designed specifically for the XE-150 unit and has a high-force piezoelectric element which allows precise control of vertical movement. Conventional AFMs have a single piezo-tube scanner that moves the tip in three directions at the same time. In these AFMs, non-linear responses are often encountered. The SPM controller processes the information from the two separate scanners to obtain 3-dimensional images.

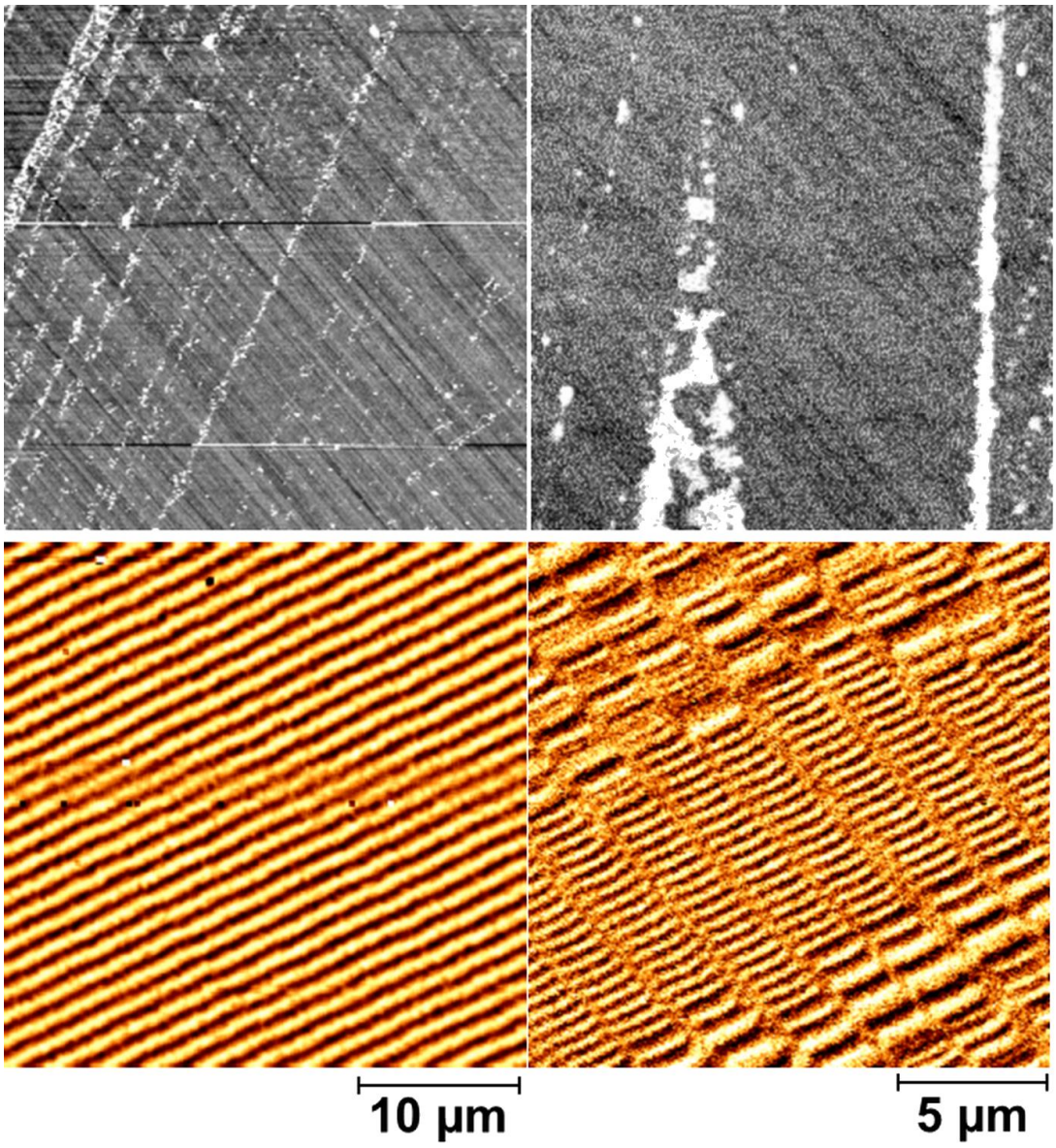

Figure 3-9 MFM images (upper row) and MFM topography (lower row) of HDD sample imaged at different scan sizes of 10µm and 5µm.

The MFM test is performed on a controlled sample from Park System Company, which is a piece of hard disk drive (HDD). The results of the MFM and topography images for the standard control sample are shown in Fig. 3.9. The images show that the MFM mode is set up correctly. The HDD sample is studied as a control and validates the MFM mode; the images produced show the topography and magnetic domain of the HDD. The surface shows a data bit in the HDD, and each magnetic domain represents a single bit that is magnetised.

In addition, it has been observed that the MFM images exhibit dependence on the tip-specimen distance [74]. The dependence is studied for the HDD sample to the distance of 200nm in order to validate the distance of the working of the MFM mode and this is illustrated in Fig. 3.10. The MFM image from Fig. 3.10b is observed at a scan height of 50nm, which shows the magnetic structure most clearly in comparison to other scan heights. As the distance between the tip-sample is increased or reduced from 50 nm (Fig.3.8 a, c and d), deterioration in the resolution of the MFM images occurs and consequently the visibility of the domain worsens and finally becomes invisible at 200nm.

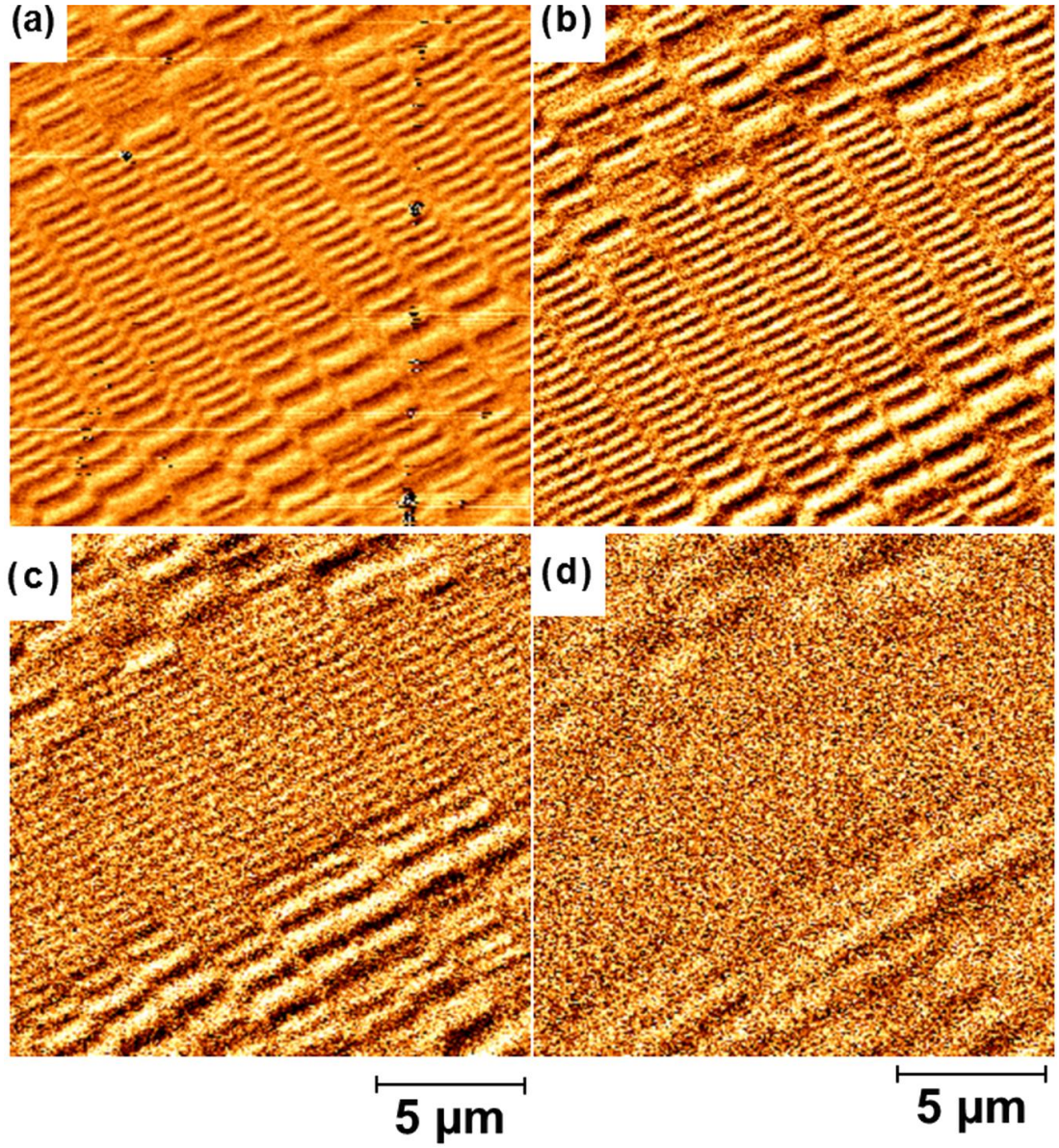

Figure 3-10 MFM images of HDD sample observed at different tip-sample separations: a) 25nm; b) 50nm; c) 100nm; and d) 200nm.

3.3.2 Capacitive discharge magnetiser

The fundamental principle of the magnetiser is to magnetise the sample by applying an external magnetic field in pulses to the sample. A strong pulse of a magnetic field in a short time is applied. The magnetiser is connected to a pick-up coil with a number of turns to convert the magnetiser current into a magnetic field to magnetise the magnets.

Fig. 3.11 shows the M6KJ magnetiser and pick-up coil from the Hirst Company which is used in this research. The magnetiser supplies energy up to 6000 Joules and variable DC voltage up to 800V. The pick-up coil has 72 turns with an inner

diameter of 80mm. In this research, the magnetiser is used to magnetise the samples in steps of voltage applied, and after that the sample is thermally demagnetised.

Figure 3-11 Magnetiser and pick-up coil for magnetizing the samples.

3.4 Structural and microstructural methods

In addition to the MFM technique used for magnetic characterisation, the structural and microstructural analysis of the materials is evaluated; in particular, to understand the grain structure of materials so as to correlate this with the MFM findings. Therefore, other characterisation techniques are used in this work and are discussed below.

3.4.1 Scanning electron microscopy (SEM)

SEM produces information about the crystal structure and chemical composition of the materials, in which a focused electron beam is directly projected onto the sample surface. The focused beam is of secondary or back-scattered electrons depending on whether the scattering is inelastic or elastic. The topographic information is generated using secondary electrons, whereas the multi-layer structures are obtained by back-scattered electrons. In addition SEM analysis generates X-rays for elemental analysis of the materials. For elemental composition analysis, the SEM usually employs energy-dispersive x-ray spectroscopy (EDX) analysis.

In this work, the SEM (Hitachi TM3030) is used to image the crystal structure of the proposed magnets in order to understand the microstructure of the samples in terms of grains and grain boundaries, and to try to connect the results with those of the MFM analysis.

3.4.2 Raman spectroscopy

Raman spectroscopy provides information on the structure and chemical composition of the materials based on the Raman effect. A laser beam interacts with the vibration of the lattice on a sample surface, leading to some photons or light particle being scattered. A few photons vary from the projected beam and are inelastically scattered. The inelastic scattering (Raman scattering) provides information about different properties of the material. The inelastic Raman scattering causes shift in energy level, and is usually called the Raman shift or wavenumber shift in units of cm^{-1}.

The LabRAM HR 800 Raman system is used in this work and is shown in Fig. 3.12. The HR 800 Raman system is integrated with a confocal microscope and two laser units.

Figure 3-12 LabRAM 800 Raman system used in this work.

3.4.3 X-ray diffraction XRD

XRD is used to study the atomic structure of crystalline solids and is a non-destructive technique. A beam of monochromatic x-rays irradiates the sample at an angle of θ or (ω) and this generates the diffraction of the x-rays. A detector records the x-ray diffraction at an angle of 2θ with respect to the projected beam. Therefore,

ω-2θ curves refer to the XRD spectra. Bargg's law describes the conditions of deductive interference for the diffracted X-rays from the expression:

$$n\lambda = 2d \sin \theta \quad (3.1)$$

where λ is the wavelength of the incident beam, n is an integer and d is a constant. XRD diffraction is used in this research to analyse the chemical composition of the magnets studied in the powdered condition.

3.5 Thermal analysis methods

The sintered Nd-Fe-B magnet is analysed at elevated temperature. The thermal analysis is performed on order to study the dynamic behaviour of microstructure of the sample. There are two thermal stages for MFM technique and Raman spectroscopy, as follows:

3.5.1 Thermal stage for MFM

The MFM is equipped with thermoelectric stage in order to image the magnetic microstructure at high temperature. The capability of thermoelectric unit is to vary the temperature degree from room temperature to 200°C. Fig. 3.13 illustrates the thermal analysis equipment. A temperature controller (LDT5525) is connected to the thermal stage which detects the heating or cooling of the sample. Small water pump is attached to the thermoelectric stage for cooling purpose. The sample is heated in-situ up to 80°C, and at different locations up to 120°C.

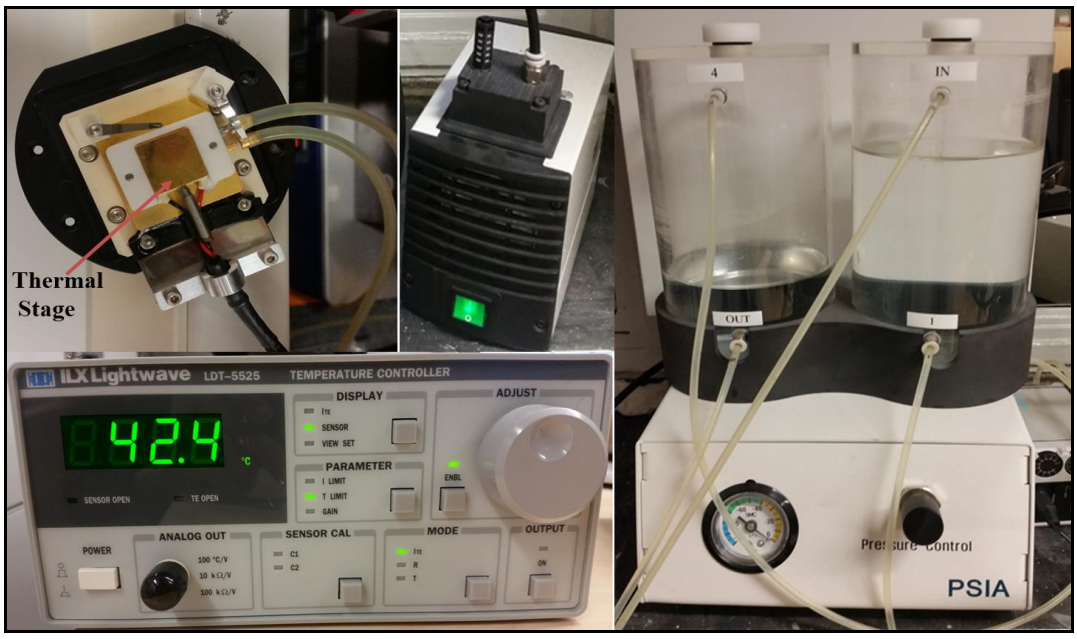

Figure 3-13 Thermal stage used with MFM technique

3.5.2 Thermal stage for Raman spectroscopy

The equipment of thermal analysis system for Raman spectroscopy is shown in Fig. 3.14. The system consists of temperature controller and thermoelectric stage. The controller detects heating or cooling of the sample. The sintered Nd-Fe-B sample is heated up to 120°C in the same and different locations.

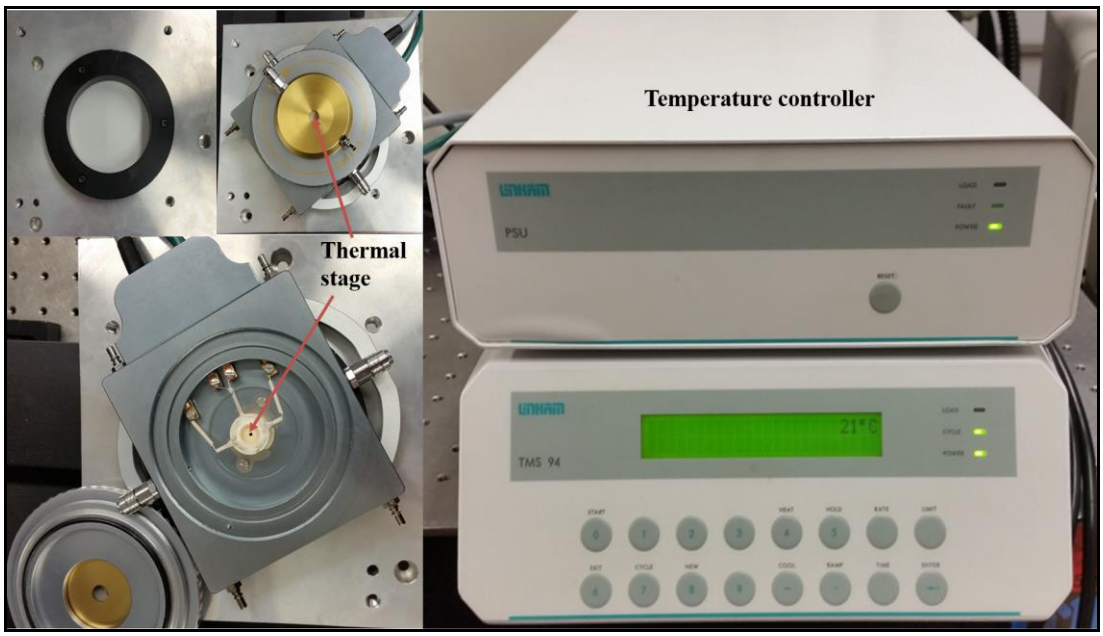

Figure 3-14 Thermal stage used with Raman spectroscopy.

3.6 Software and models developed

In this study, digital imaging process software is used and two models are developed to analyse the MFM images and determine the main domain width and domain wall energy. A brief description of the procedure used for the imaging software is shown in the following sections along with the models developed:

3.6.1 XEI digital imaging process software

The MFM images are analysed using XEI image processing software developed by Park System (XEI version 1.8.0.Build20, Copyright © 2002-2011 Park Systems Corp.), specifically designed for SPM data and mainly used to process AFM images [85, 86]. The XEI software is similar to WSXM software [87].

The strategy applied is to enhance the image using arithmetic filter processing techniques. The techniques of the arithmetic filter in XEI are divided into four groups: smoothing, sharpening, edge enhancement, and custom. Both smoothing and

sharpening processes are applied on MFM images. The sharpening process uses a high-pass filter with a kernel size of 13×13 to produce more noticeable smaller features. Then, the smoothing process is utilized using a Gaussian blur filter with kernel size 7×7 in sequence to remove the noise from high frequencies [87, 88].

The XEI digital processing software is carefully utilised in this work to produce an image similar to the original observed MFM image with black and white areas in order to be identified for Matlab software.

In addition, XEI digital processing software is adopted with the 3-dimensional view [86, 89]. In the 3D view, the sample surface is scanned horizontally in the X-Y line by line while the profile of the vertical (z) direction is collected at the sample surface. As a result, truly 3D information from the surface is collected by the SPM controller. Detailed explanations of the 3D view mechanism of the XEI software is shown elsewhere [86]. This 3D data explains the domain structure more clearly and distinguishes unwanted features or defects.

Furthermore, the watershed method in XEI software is used to evaluate the nucleus volume from the MFM images. The algorithm of the watershed method is explained in detail elsewhere [86]. However, to understand the idea of the watershed algorithm, assume that water is dropped over a surface. The lowest points of the surface are filled first with water. These lowest regions are recognised first as a single grain. More grains are detected as the water fills more regions. The algorithm recognizes the grain boundaries and sets the points when the level of water reaches a certain level and overflows from one grain to other neighbouring grains. A number of parameters is detected using the watershed method, such as the area, volume, and length of each recognised grain.

3.6.2 Models for main domain width and domain wall energy

An effective domain width can be defined using the ratio between an area and the integrated wall length in this area. One procedure for evaluating domain width is based on the stereological method proposed by Rudolf and Hubert [60]. In this method, the intersections of domain walls with arbitrary test lines are counted and evaluated. According to Rudolf and Hubert, the domain width D_w is determined using the following formula:

$$D_W = \left(\frac{2}{\pi}\right) \times \left(\sum_i l_i\right) / \left(\sum_i n_i\right) \tag{3.2}$$

where l_i is the length of the i^{th} test line and n_i is the number of intersections of the i^{th} test line with the domain walls.

The domain width is determined by developing a model based on the stereological method with 1000 test straight lines or more (100 test lines are shown in Fig. 3.15). The length of each line, the total length of the test lines and the number of intersection points are then accurately determined. The procedure is repeated 10 times for each image in order to evaluate the accuracy of the determination of domain width. This method is applied after enhancing the MFM images using the XEI digital imaging process so as to produce an MFM image suitable for Matlab software. The model code is illustrated in Appendix A.

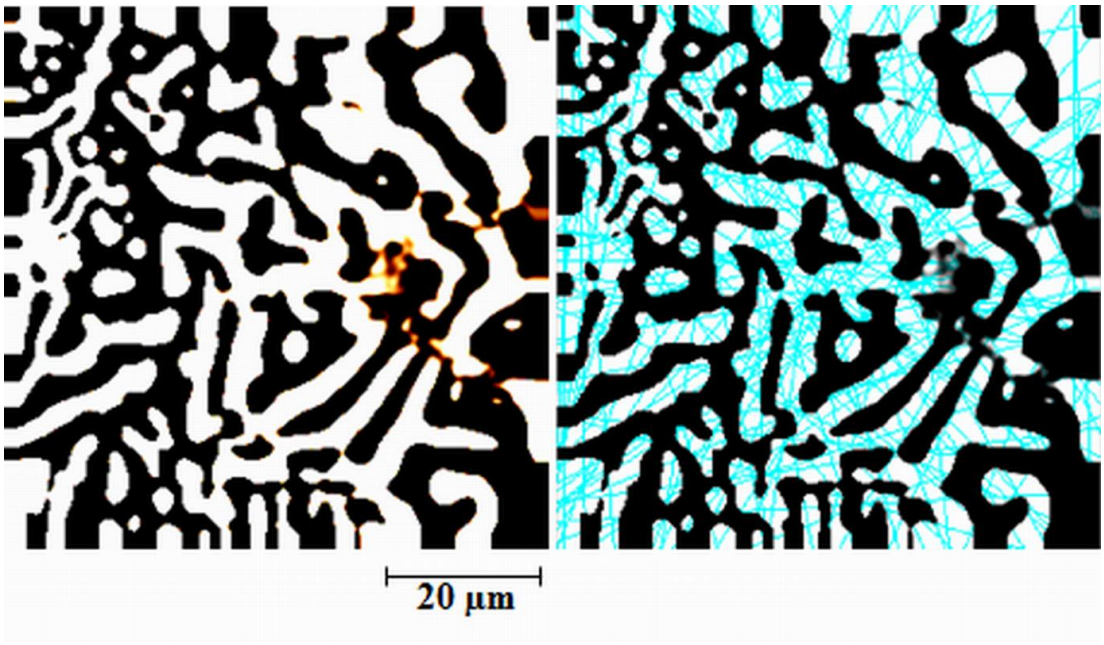

Figure 3-15. 100 test lines applied on an MFM image in the stereological method.

In addition, the domain wall energy (γ_w) is evaluated according to the model proposed by Bodenberger and Hubert [61] from the expression:

$$\gamma_w = \frac{D_w (M_s)^2}{4\pi\beta} \tag{3.3}$$

where: D_w is the determined domain width and M_s is the magnetisation saturation of the magnet. β is a coefficient depending on the surface structure and its value has

been previously determined as 0.31 for $SmCo_5$ and similar magnetic materials with high magnetocrystalline anisotropy [61]. The Matlab code of the model is illustrated in Appendix A.

3.7 Summary

This chapter has described the local techniques used in this research in terms of basic principles and working processes. The chapter is divided into three main sections. The first section has explained the sample preparation and equipment, including the samples used, magnetic properties and preparation requirements. The sample preparation procedure has been explained, from sectioning and mounting to grinding and polishing. The second section has presented the magnetic characterisation methods, such as magnetic force microscopy (MFM) and the capacitive discharge magnetiser. This section discussed the basic principles and settings for local MFM along with details of the schematic diagram of the system. In the third section, the structural and microstructural methods used for crystal structure analysis have been reviewed. The models and software involved in this study for the analysis of the MFM images have been presented in detail in this chapter.

CHAPTER 4 MAGNETIC DOMAIN ANALYSIS OF SINTERED ND-FE-B AND SMCO MAGNETS

4.1 Introduction

The analysis of magnetic domain structures is very important for the development of high performance permanent magnets. An important mechanism in explaining improvements in coercivity and remanence is magnetic domain morphology and interaction. In this chapter the domain structure for the proposed sintered Nd-Fe-B and SmCo magnets are observed using MFM in both perpendicular ($\perp$) and parallel ($/\!/$) directions in relation to the alignment axis. A comparison of domain structures in both alignment directions is illustrated. Attention is focused on analysing domain patterns in the 3D view to clarify the domain structure and distinguish unwanted features.

In addition, the impact of tip-sample distance and random magnetisation on MFM images are discussed. This chapter provides a deeper understanding of magnetic domains for sintered permeant magnet materials in different directions of magnetic alignment.

4.2 The effect of tip-sample distance and random magnetisation

During the scanning process, two forces are generated depending on the tip-sample distance: van der Waals forces and magnetic forces. The van der Waals forces are at small tip-sample distances, while the magnetic interactions are at higher separation. The generation of these forces relies on the effect of the interaction force from the sample on the scanning tip. Hence, the MFM images depend on the distance between the magnetic tip and the magnetic sample surface. In this section, the sample is scanned at different tip-specimen distances in order to evaluate the distance range of magnetic signal.

Fig. 4.1 illustrates the dependence of MFM images on the tip-sample distance up to 300 nm. The sample is a sintered Nd-Fe-B magnet. At low tip-sample separation from 25 nm to 100 nm, the MFM images are influenced by the topographic forces or van der Waals forces and the magnetic domains are not visible. The magnetic

domains become clearly visible from tip heights of 150 nm to 250 nm. The contrast in the MFM images deteriorates as the tip-sample distance increases up to 300 nm. Consequently the domain structures are expected to be less visible above 300nm until they become completely invisible because the impact of the sample magnetic force on the tip is lower at very high tip-specimen distances (>300nm). Therefore the range of good contrast MFM images is observed to be from 150 to 250 nm for the sintered Nd-Fe-B magnet.

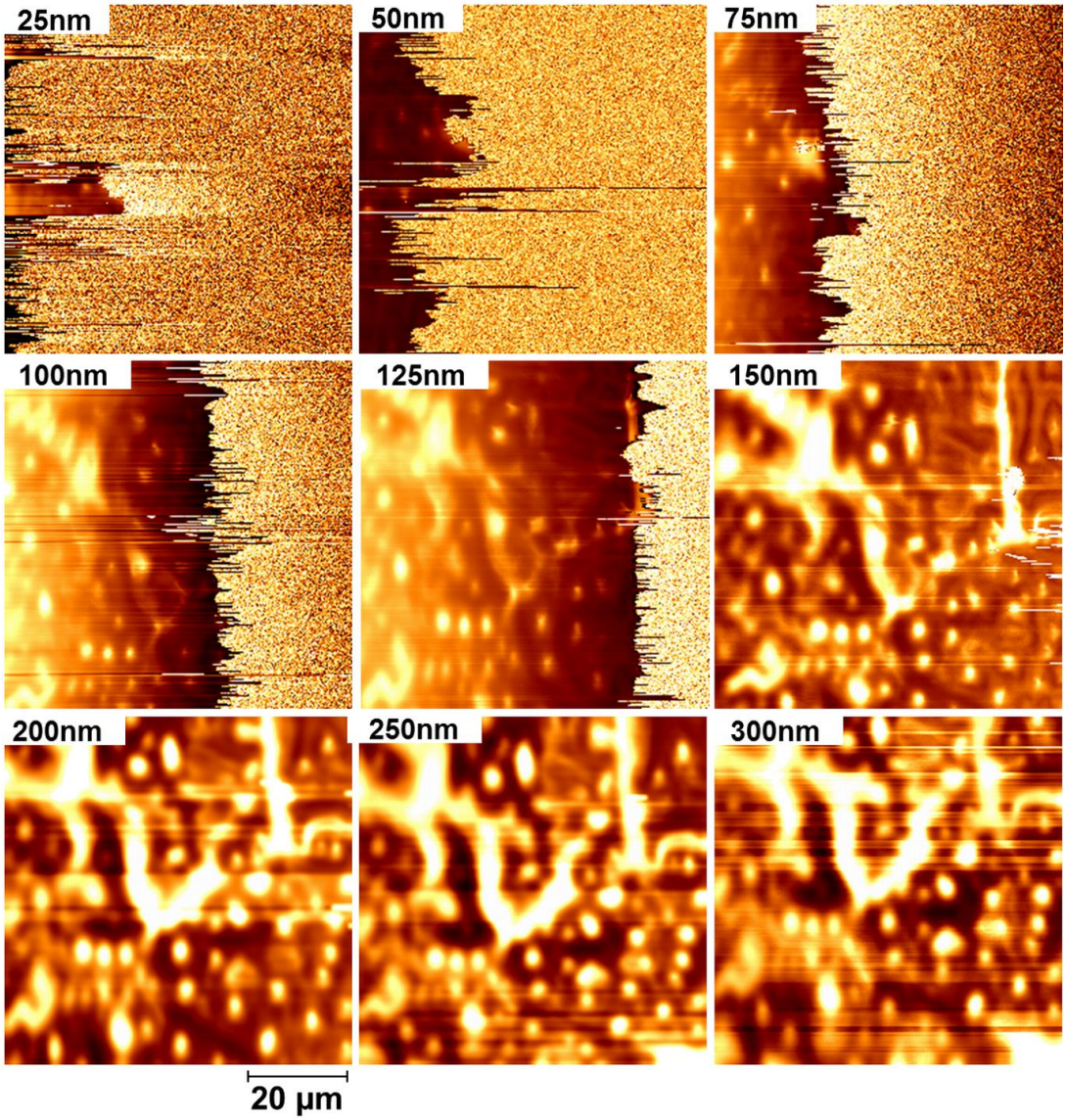

Figure 4-1 MFM images of sintered Nd-Fe-B magnet observed at different tip-sample distances.

Usually, the magnetic tip senses the stray field of the sample at a constant height over the surface. As the tip-sample distance is increased, the stray field cannot be sensed by the magnetic tip. Therefore it is important to understand the location of

the magnetic tip over the sample surface to obtain better MFM images with good contrast.

The surface roughness is measured at each tip-sample distance, as shown in Fig. 4.2. The average roughness increases with tip-sample distance, and at higher distances (≥300), the roughness is reduced. The surface roughness may indicate the range of tip-sample distances over the sample.

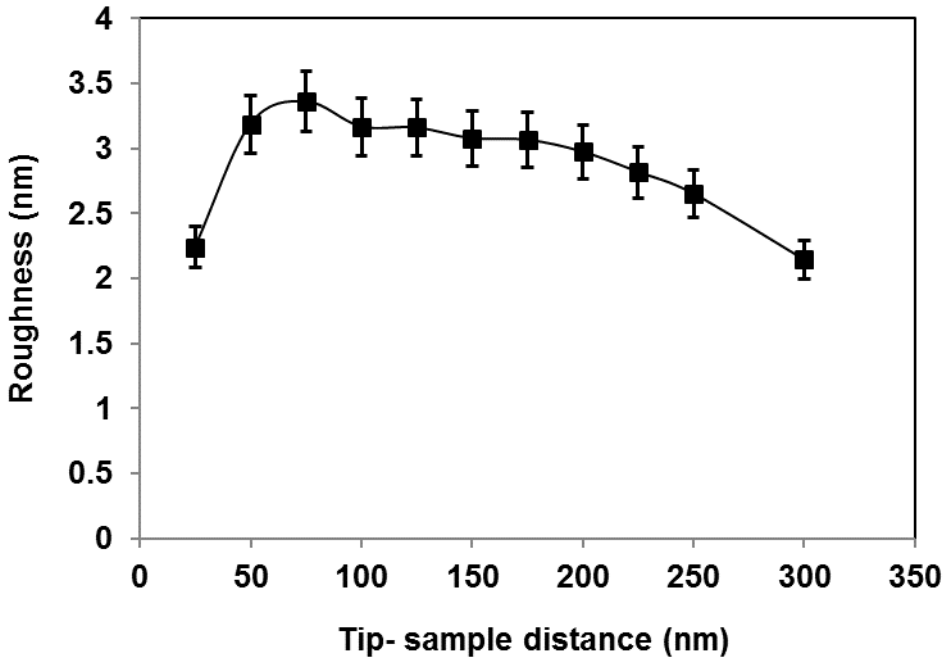

Figure 4-2 Surface roughness of sintered Nd-Fe-B measured at each tip-sample distance.

In order to verify that the tip was not randomly magnetised and demagnetised by the sample, the same sample area is rescanned at different scan sizes and heights [90]. Fig. 4.3 shows the same sample area re-scanned at different scan sizes and heights in direction perpendicular to the alignment axis. The first scan was at a height of 200nm and a size of 20 × 20μm (Fig.4.3a), and then same area was scanned at a tip-sample distance of 50nm and 10 × 10μm scan size (Fig. 4.3b). This was found to produce a similar scan image to the first one with different scan size, which indicates that random magnetisation had not occurred during scanning. In addition, Fig. 4.3 confirms that the tip observes the same domain patterns at different conditions. If the observations in such cases were different, this would mean that the observations of domains are not accurate. It can be noted that there is a difference in resolution between Fig. 4.3 (a) and (b) because of the effect of Van Deer Waals forces apparent at smallest tip-sample distances. As the tip-sample separation is increased, the

magnetic effects become apparent. One way to separate magnetic images from topographic images is by collecting a series of images at different tip heights. 50nm and 200nm are the smallest tip-sample separations at which the magnetic image can be observed without the effect of Van Deer Waals forces, for 10µm and 20µm image sizes respectively.

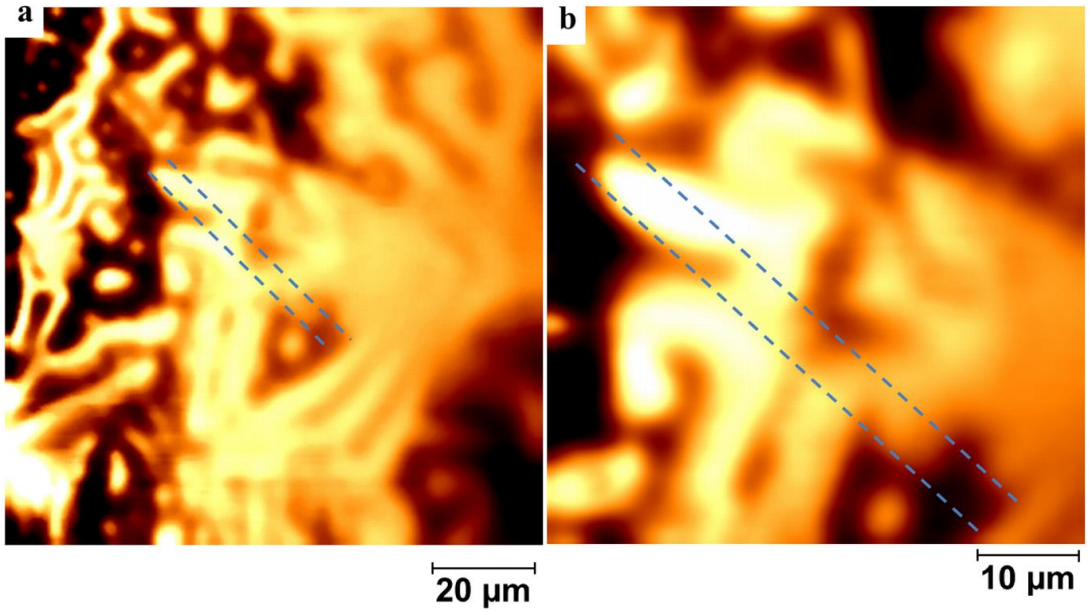

Figure 4-3 MFM images scanned at different scan size and tip-sample distance on the surface perpendicular to the alignment axis: (a) scan size 20 × 20µm and 200nm scan height, (b) re-scan from (a) with scan size of 10 × 10µm and tip-sample distance of 50nm**.**

It is concluded that the contrast in MFM images depends on the tip-specimen distance. In this thesis, the MFM images for the different proposed magnets are imaged at a tip height of 200nm.

4.3 Domain structure observation on the perpendicular surface

The domain structure is studied in the direction perpendicular (⊥) to the magnetic alignment axis in the thermally demagnetised state. The samples are a sintered Nd-Fe-B magnet, one batch of sintered $SmCo_5$ magnets and a selection of three different sintered $Sm_2(Co,Cu,Fe,Zr)_{17}$ magnets. The structure and properties of the magnets are explained in detail in chapter 3, section 3.2.

Fig.4.4 illustrates the domain structure of a sintered Nd-Fe-B magnet on the surface perpendicular to the alignment axis, observed at different locations on the same surface using the MFM technique. The upper row shows the topographic images while the lower row illustrates the corresponding MFM images. Folks *et al* [39]

described the microstructure observation of sintered Nd-Fe-B on the perpendicular alignment axis using MFM as a magnetic domain with different patterns, such as bubble domains and stripe domains. Furthermore, in 2006, Szmaja reported the domain structure of different samples of sintered Nd-Fe-B observed by MFM in the direction perpendicular to the alignment axis and described then as maze domains and reverse spikes [40]. The maze-like domains have frequently been reported using MFM for SmCo and Nd-Fe-B magnets in the direction perpendicular to the alignment axis [4, 76, 91].

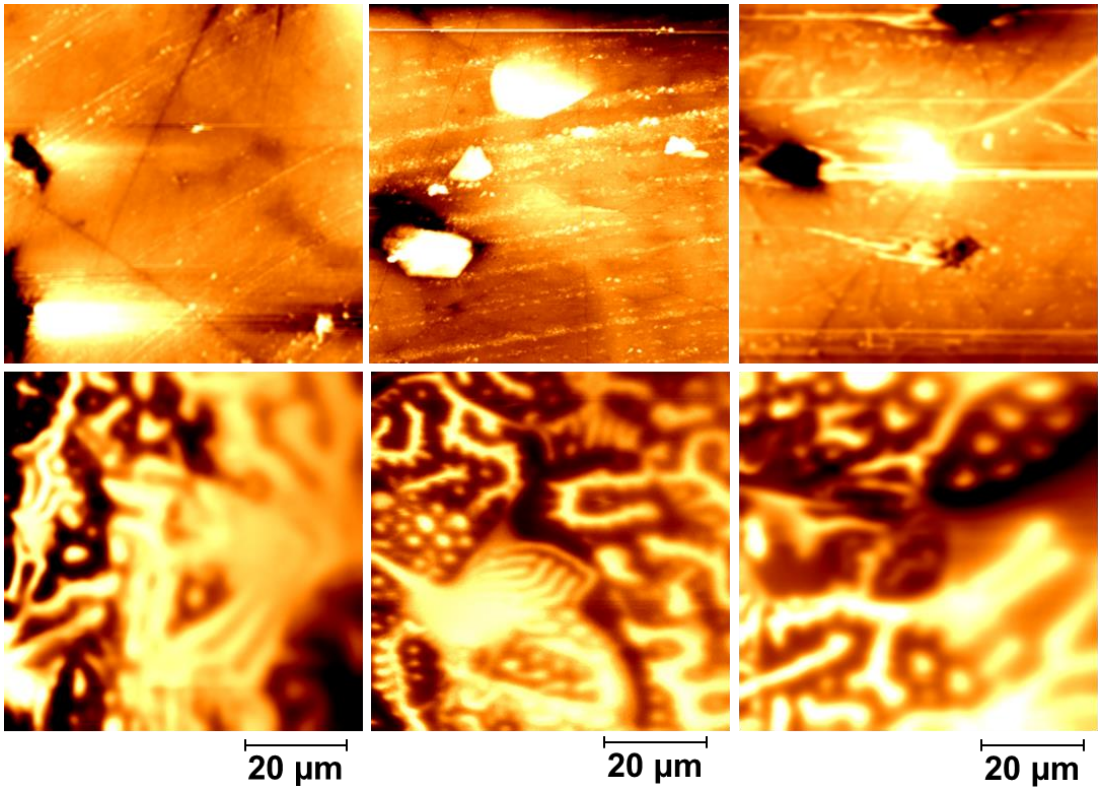

Figure 4-4 Typical domain structure of sintered Nd-Fe-B magnet observed using MFM on the surface perpendicular to the alignment axis at different locations. Upper and lower rows show topography images and MFM images respectively.

Therefore, the MFM images in the lower row in Fig. 4.4 can be described as magnetic domains that are composed of main domains and domain walls. The MFM images show that there are undulations within the main domains that form a maze-like pattern. However, this occurrence reduces the magneto-static energy at the cost of an increase in the total Bloch wall area. The stray fields of the main domains reverse the tip magnetisation each time when traversing a domain boundary wall, generating black highlighted walls leading to a loss of information on the boundary. The images display different contrast domains (dark and bright) magnetised in

directions opposite to each other. The dark and bright domains are associated with attractive and repulsive stray fields respectively acting on the MFM tip.

Furthermore, it should be noted from the lower right quadrant of the MFM images as shown in Fig. 4.5 that some domains appear with parallel straight domain walls with a different shape to most of the main domains. These are referred to as stripe or surface domains [40, 60, 83, 92]. The magnetostatic interaction energy between the stripe domains and the tip was not perturbed, as clearly shown by the straight lines. These domains are magnetised perpendicular to the surface alignment opposite to the main domains, and they reduce the magnetostatic energy close to the sample surface.

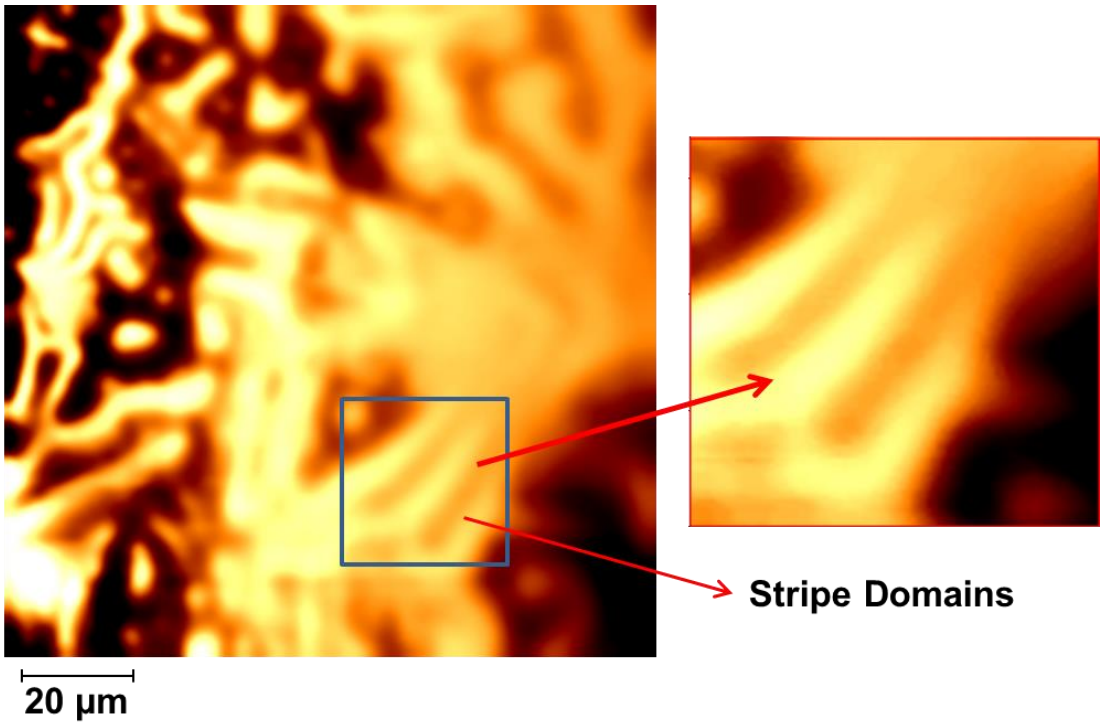

Figure 4-5 The appearnce of stripe domains in a sintered Nd-Fe-B magnet on the surface perpendicular to the alignment axis observed using the MFM method.

The sample of sintered Nd-Fe-B magnet is scanned at the same location with different sizes to verify the correlation between domains and grains. Fig. 4.6 shows in-situ observations of topography and MFM images scanned at different sizes (50 × 50µm and 20 × 20µm). There are some domains near the centre of the MFM image in Fig. 4.6 that appear as entirely bright areas with a different shape to most of the main domains. These are associated with a strong repulsive force acting on the tip with a positive force gradient that specifies a high stray field in their regions. This indicates that the grain has a multi-domain structure. These images confirm that the tip was not perturbed during scanning and accurately observed the domain structure.

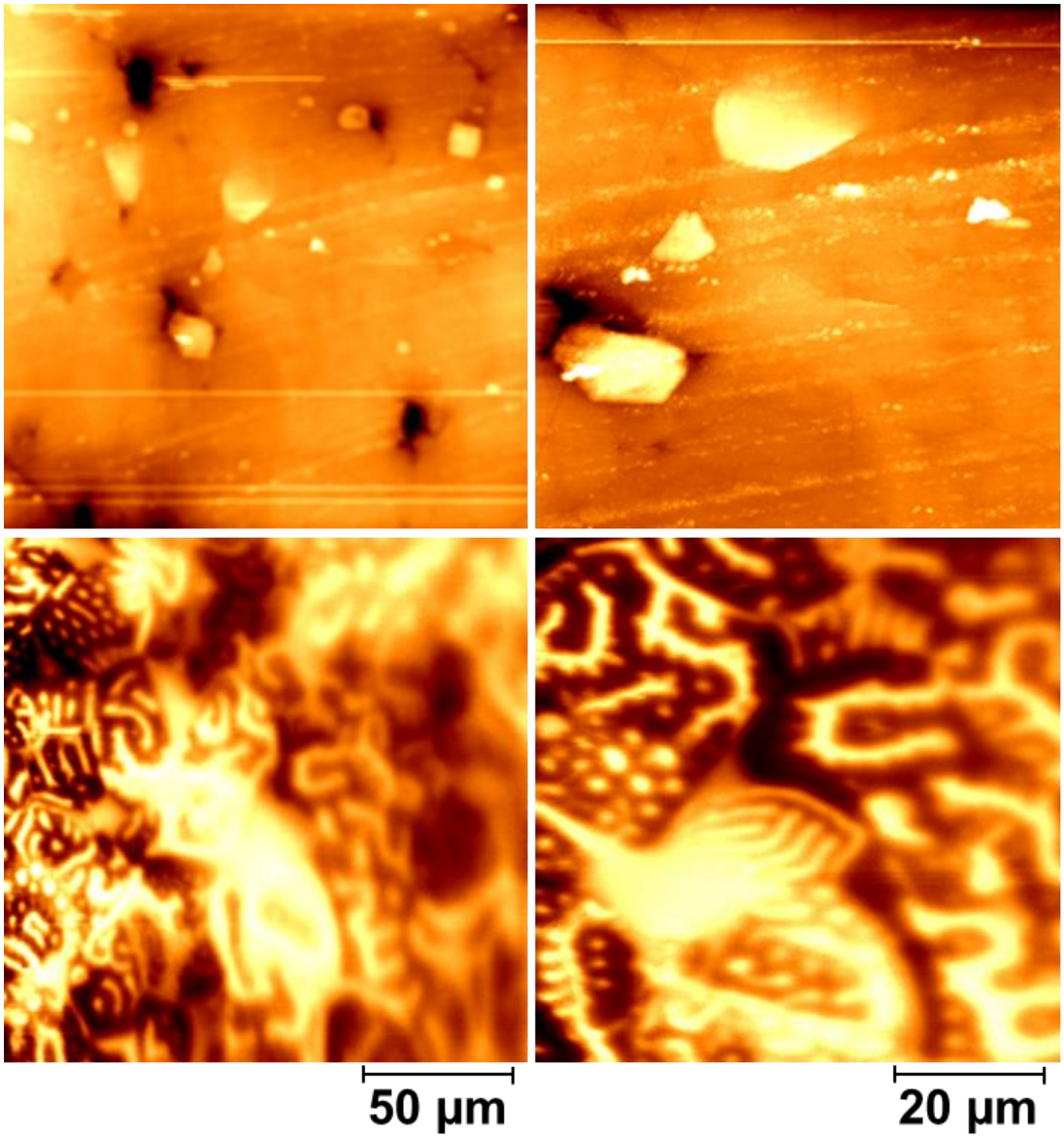

Figure 4-6. In-situ observations of domain structure for sintered Nd-Fe-B magnets at different scan sizes.

In addition to sintered Nd-Fe-B magnet, the domain structure of sintered $SmCo_5$ and Sm_2Co_{17} magnets is studied in the direction perpendicular ($\perp$) to the magnetic alignment axis in the thermally demagnetised state. Three different samples of sintered Sm_2Co_{17} magnets (A, B, and C) have been prepared using different processing routes. Sample A is the standard Sm_2Co_{17}, while specimens B and C have been annealed at different annealing temperatures. Fig. 4.7 shows the domain structure of these sintered SmCo magnets observed on the surface perpendicular to the alignment axis. Each column represents a single magnet, as indicated on the top of each column. The upper row shows the topographic images while the lower row

illustrates the corresponding MFM images. On the whole, the four samples differ significantly in the structure of the magnetic domains.

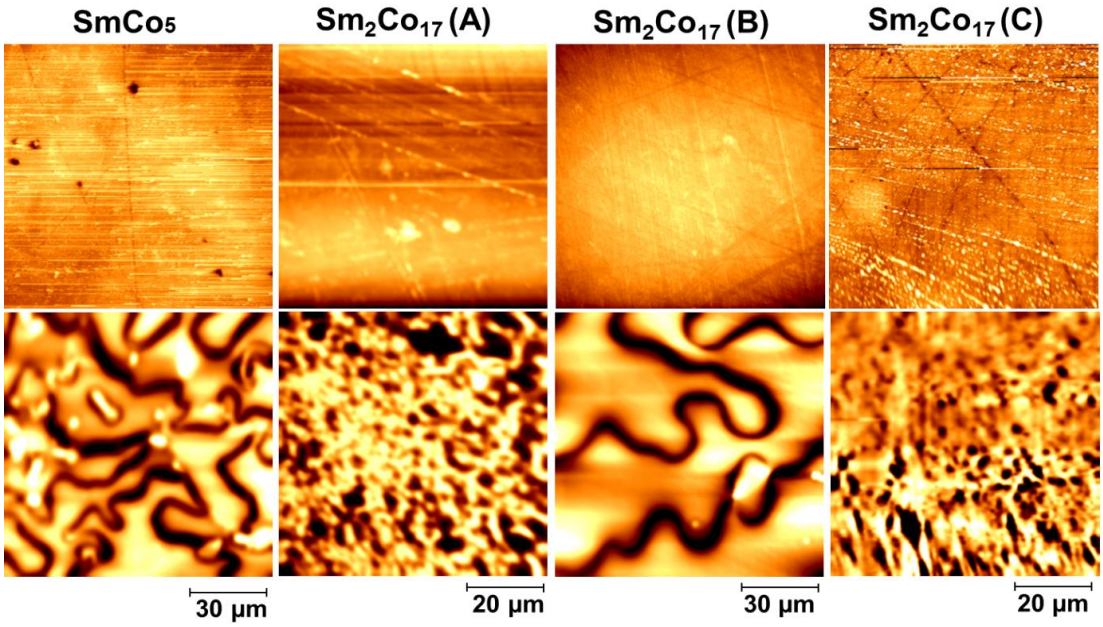

Figure 4-7. Typical domain structure of sintered SmCo magnets observed using MFM on the surface perpendicular to the alignment axis. Upper and lower rows show topography images and MFM images respectively. The MFM images show maze-like patterns in the domain structure. The difference in the scale of images is due to the different grain size of each material.

The structures of the magnetic domains in Fig. 4.7 have maze-like patterns similar to those in the sintered Nd-Fe-B magnets. As the tip is repulsed or attracted by the magnetic force from the sample, the resonant frequency of the cantilever changes leading to the variations in contrast (dark and light). The maze domains appear as light while the domain walls are imaged as dark. During the process of scanning, the stray field of the maze domains reverses the magnetisation of the tip each time when passing a domain wall. The maze domains reduce the magnetostatic energy near the surface at the cost of an increase in the total Bloch wall area. It can be seen that the main domains of $SmCo_5$ and Sm_2Co_{17} (B) are detected as a coarse domain structure of a few micro-metres in width. The coarse domains indicate that the materials have a large grain size and fewer defects. During the reversal process of magnetisation, the domain walls move easily in the crystal without interaction, generating a low magnet coercivity [4, 83, 91, 93]. Meanwhile, the microstructure of sintered Sm_2Co_{17} (A) and (C) exhibit fine domains, when compared to $SmCo_5$ and Sm_2Co_{17} (B). These fine domains indicate the formation of magnetic interaction between neighbouring domains and grains [94]. The magnetic interaction is an important concern in controlling magnet coercivity [93].

In addition, the topographic images in Fig. 4.7 reveal some topographic features, such as lines and small circles, generated during the polishing process. However, when comparing the topography images with the corresponding MFM images, the surface topography has no influence on the magnetic domain structure.

The magnetic domain structure of the SmCo magnets studied is different from one sample to another due to differences in magnetic anisotropy and grain size.

4.4 Domain structure observation on the parallel surface

The materials proposed for sintered Nd-Fe-B and SmCo magnets are studied in the parallel alignment axis using the MFM method. The domain structure is observed in the direction parallel to the magnetic alignment axis in the thermally demagnetised state.

The sintered Nd-Fe-B magnets are scanned at different locations on the same surface, as shown in Fig. 4.8. The domain structure is observed in the direction parallel to the alignment axis. The upper row displays the topography images, while the corresponding MFM images are shown in the lower row. The MFM images are not influenced by the topographic features of the surface.

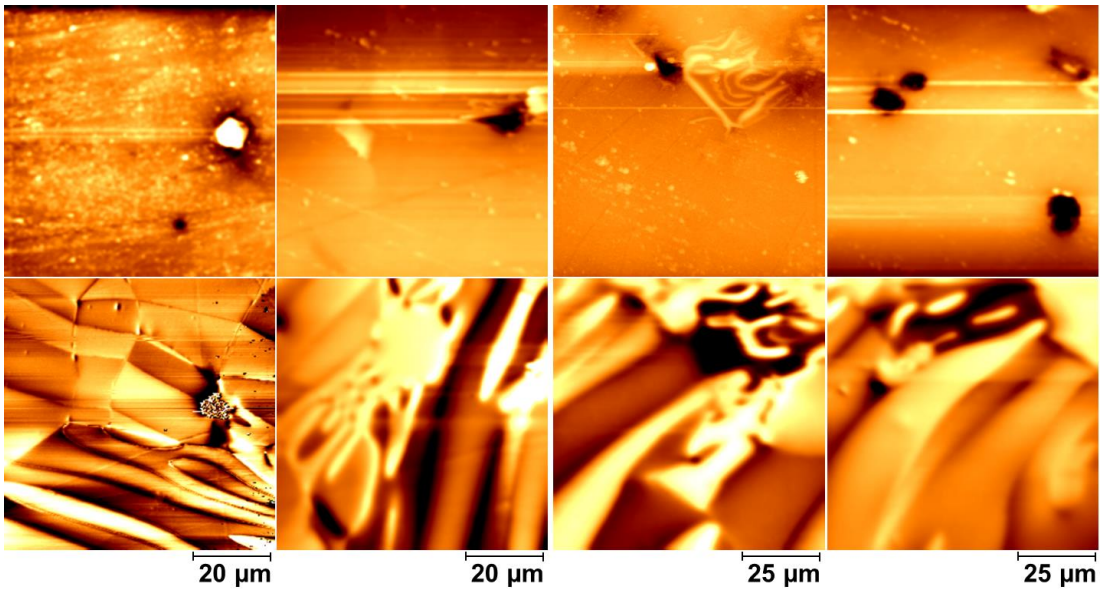

Figure 4-8 Typical domain structure of sintered Nd-Fe-B magnet observed using MFM on the surface parallel to the alignment axis at different locations. The upper row shows topography images while the lower row reveals the corresponding MFM images.

The magnetic domain microstructure largely consists of domain walls lying parallel to the magnetisation direction in almost straight lines. Recently, Fang *et al* reported

the appearance of similar plate-like domains and grains observed using MFM in the direction parallel to the alignment axis [95]. The main domains of the MFM images are stripe-like patterns. However, the appearance of the stripe domain structure is one of the characteristics of the surface parallel to the alignment axis for uniaxial materials with $K_1 > 2\pi M_s^2$ (where M_s is the saturation magnetisation and K_1 is the first order anisotropy constant) [40, 60]. The images display different dark and bright contrast domains magnetised in directions opposite to each other. The dark and bright domains are associated with attractive and repulsive stray fields respectively acting on the MFM tip. Generally, to achieve high coercivity, the tetragonal $Nd_2Fe_{14}B$ matrix phase has strong magnetocrystalline anisotropy. This causes the alignment of the magnet to be preferred along the c-axis (alignment axis) [29]. Therefore, the study of the domain structure on the surface parallel to the alignment axis can provide direct information on the magnetic alignment of each individual grain along the alignment axis (c-axis).

In addition, the parallel side of the domain structures shows the appearance of branch-like patterns, as shown in Fig. 4.9. The domain wall energy is influenced by the branched domains, which have been described as saving the energy of domain walls [60]. These domains indicate that a different magnetisation process occurs in the branch. It can be seen that the branched patterns show a two-phase branching which may lead to two magnetisation directions. The branch-like domains were observed for Nd-Fe-B magnets at different orientations and a systematic series of these domains are shown elsewhere [60].

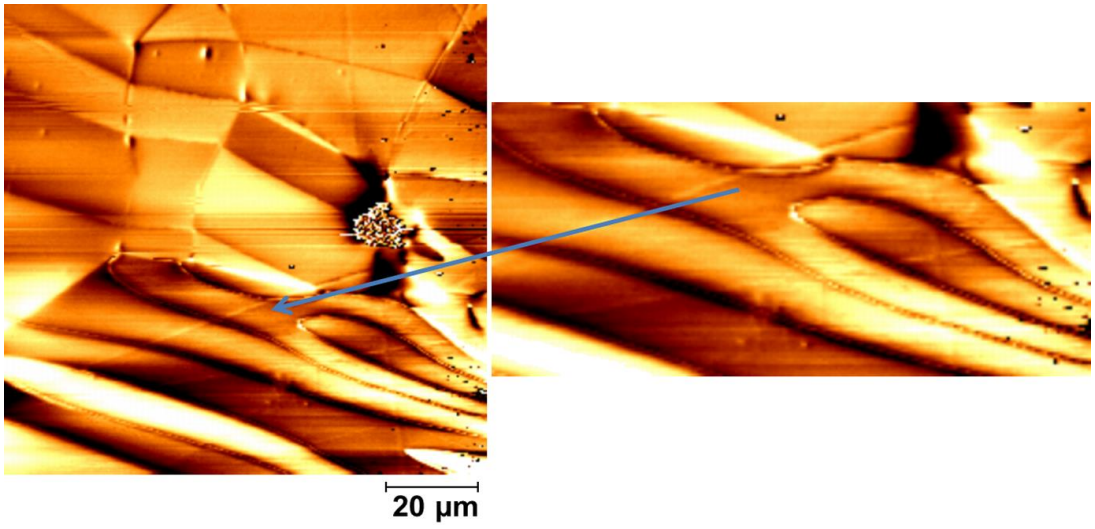

Figure 4-9 MFM image of sintered Nd-Fe-B showing the appearance of branch-like domains, observed in the direction parallel to the alignment axis.

Furthermore, one of the characteristics of parallel side observation is the appearance of a grain structure. Fig. 4.10 shows the grain structure of the studied sintered Nd-Fe-B magnet observed using MFM in the direction parallel to the alignment axis for different areas of the same sample. It can be noticed from the MFM image in Fig. 4.10 that the grains have a good magnetic alignment across nearly the whole surface, with the domain structure appearing as stripes running approximately parallel to the alignment axis. It has been stated in a previous study [2] that the better the magnetic alignment between grains, the higher the magnetisation produced. There are some exceptions in the images where magnetic misalignment appears between the grains, which leads to an increase in coercivity and a decrease in the remnant magnetisation M_r with a consequent reduction in the maximum energy product $(BH)_{max}$ [96].

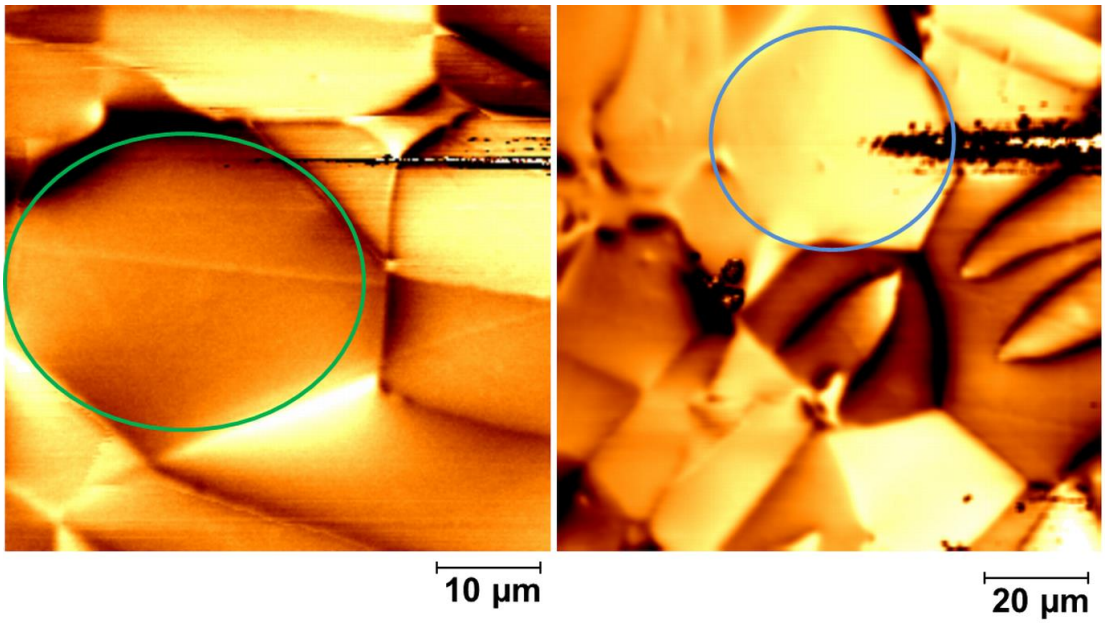

Figure 4-10 MFM images of sintered Nd-Fe-B magnet showing the grain structure in different areas of the sample in the direction parallel to the alignment axis.

The size of grain in Fig. 4.10 is much larger the domain size, which indicates that multi-domain structures exist in each grain. Previous research has reported that each grain has a multi-domain structure [68, 92, 97]. The magnetic domains at the grain boundaries seem to be terminated, and the separation of the magnetic domains at grain boundaries is an important concern in developing high coercivity magnets. Moreover, the images presented show domain walls extending through the boundaries of individual grains. This indicates that there is magnetic interaction between neighbouring grains and domains.

In addition, the domain structure of sintered SmCo samples is observed in the direction parallel to the alignment axis, in the thermally demagnetised state. The sintered SmCo magnets are four different types of $SmCo_5$ and Sm_2Co_{17}. The structure and properties of these samples were explained earlier in section 3.2.

The observed domain structures of the sintered SmCo magnets are shown in Fig. 4.11, in the surface parallel to the alignment axis. Each column represents a single magnet, as indicated on the top of each column. The upper row shows the topography images while the lower row displays the MFM images. In general, the four samples vary in their magnetic domain structures.

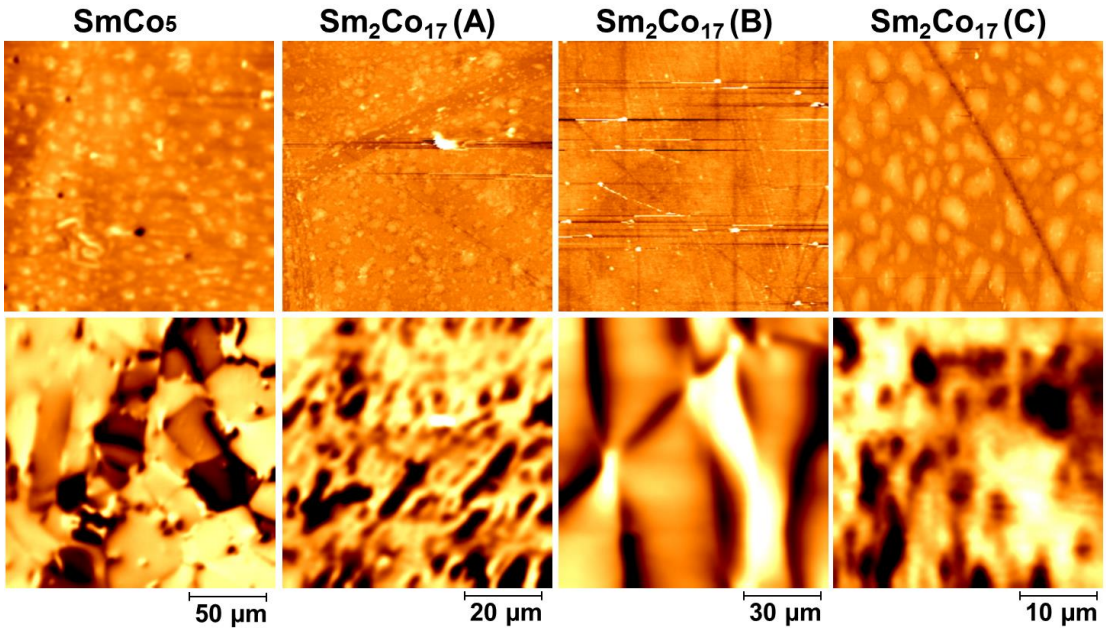

Figure 4-11 Typical domain structure of sintered SmCo magnets observed using MFM on the surface parallel to the alignment axis. The upper row shows topography images while the lower row reveals the corresponding MFM images. Each column represents a single magnet, as indicated on the top. The difference in scale of images is due to the different grain sizes of each material.

The topographic images in the upper row have lines, scratches and features appearing on the surface. These topographic features may be because of sample preparation. The MFM images are not influenced by the topographic features of the surface. The magnetic domains on the lower row (parallel direction) largely consist of stripe-like patterns with domain walls lying in almost straight lines parallel to the magnetisation direction. The stripe-like domains reduce the magnetostatic energy near the sample surface. The image of the $SmCo_5$ magnet has more grains than domains, and a large scan size is required to present the structural configuration clearly. This provides information on the magnetic alignment and size of each individual grain, as well as

the orientation of grain surface with respect to the magnetic alignment axis (parallel). The microstructures of Sm_2Co_{17} (A) and (C) exhibit fine domains when compared to $SmCo_5$ and Sm_2Co_{17} (B). This indicates that magnetic interaction is formed between neighbouring domains and grains which lead to high coercivity.

The Sm_2Co_{17} (B) microstructure shows the appearance of branch-like domain patterns in the parallel side, as shown in Fig. 4.12. The branched domains influence the domain wall energy. The size of branched domains seems to be high compared to the other materials. The branching patterns are one of the characteristics of uniaxial crystal on the side plane (parallel to alignment axis).

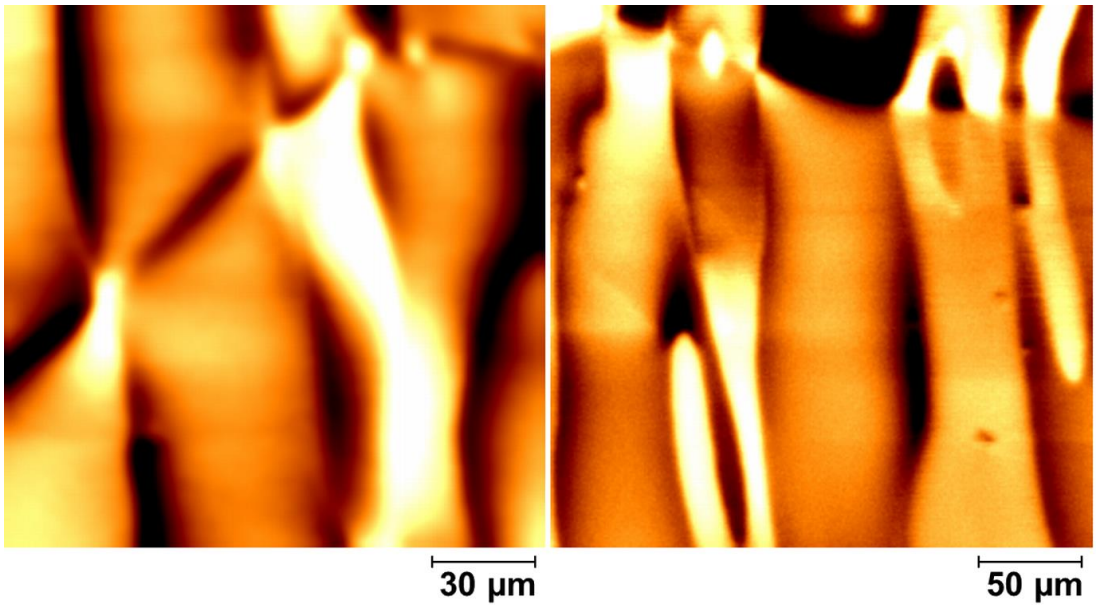

Figure 4-12 The appearance of branch–like domains for sintered Sm_2Co_{17} (B) magnets in the direction parallel to the alignment axis.

The results for all of samples show clear differences in the domain structures in both perpendicular and parallel directions. However some samples exhibit similarities in domain patterns, such as the sintered Nd-Fe-B and Sm_2Co_{17} (A) and (C). Therefore it is important to understand the differences in domain patterns by comparing all of the samples in one figure for both directions, as presented in the next section.

4.5 Domain structure comparison on perpendicular and parallel alignment axes

In order to evaluate the differences in domain structures between the samples, the MFM images are shown in one figure for both directions. Fig. 4.13 shows the domain structure of sintered Nd-Fe-B and the different types of sintered SmCo magnets on the surfaces perpendicular (upper row) and parallel (lower row) to the

alignment axis. Each column represents a single magnet, as indicated on the top row. On the whole, the five samples differ significantly in the structure of the magnetic domains.

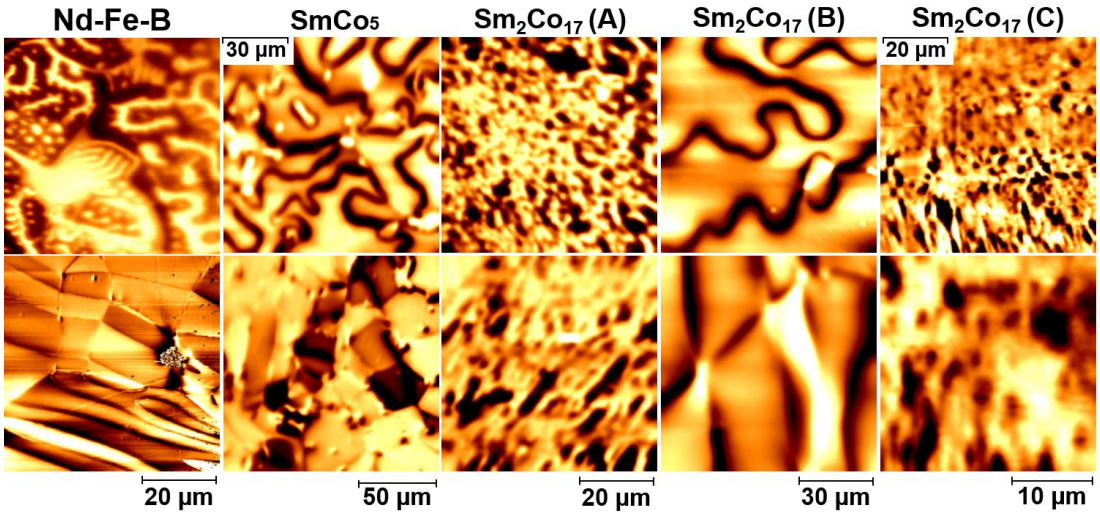

Figure 4-13 Typical domain structure of sintered Nd-Fe-B and SmCo magnets observed using MFM on the surfaces perpendicular (upper row) and parallel (lower row) to the alignment axis. The MFM images show maze-like and stripe-like patterns in both perpendicular and parallel alignments. As the tip is repulsed or attracted by magnetic force from the sample, the resonant frequency of the cantilever changes, leading to the variations in dark and light image contrast. The differences in the scale of images are due to the different grain sizes of each material.

The structures of the magnetic domains have maze-like and stripe-like patterns in both the perpendicular and parallel alignments respectively. These domain patterns have been discussed earlier in detail. It can be seen that the main domains of $SmCo_5$ and Sm_2Co_{17} (B) are detected as coarse domain structure in both alignment directions of a few micro-metres width. The coarse domains indicate the low coercivity of the magnets. During the process of reverse magnetisation, the domain walls move easily in the crystal without interaction generating low coercivity [4, 83, 91, 93]. The microstructures of Nd-Fe-B and Sm_2Co_{17} (A) and (C) exhibit fine domains. These fine domains indicate the formation of magnetic interaction between neighbouring domains and grains [94]. The interaction of domains is an important concern in controlling magnet coercivity [93].

The results show that just changing the annealing temperature can have a major effect on the domain structure and magnetic properties as it is presented for the Sm_2Co_{17} magnets. The data also show the necessity to observe the domain structure in the directions both parallel and perpendicular to the alignment axes.

4.6 Visualisation of domain structures in 3D view

In this section the domain structures are displayed in a 3-dimensional view. The mechanism of 3D viewing is described in detail in section 3.6. The 3D data explain the domain structure more clearly and allow unwanted features to be distinguished.
In addition to the maze domains, stripe domains and branch-like patterns observed on the perpendicular and parallel directions for sintered Nd-Fe-B magnets, Fig. 4.14 illustrates some domains within the main domains which appear on the surface perpendicular to the alignment axis as spikes and reverse spikes or domains. In Fig. 4.14 the spikes are displayed as approximately conically shaped spikes in the 3D view. The meaning of the z axis in the 3 D view is the height of the surface structure or patterns which can be measured using line profiles. When 2-dimensional profiles (cross-section) are applied, the accurate width (distance on x or y) and height (distance in z) can be measured [87]. Nevertheless, the spikes within the main domains appear to follow the bends of some maze domains in the 3D view. These types of domains have been described as ripple patterns that follow the domain walls [98]. It has been stated that, if these ripples are interpreted as spike domains, they would reduce the domain wall energy [77, 98, 99]. The spike domains and reverse spikes reduce the domain wall energy, generate a strong surface anisotropy, and may reduce the density of magnetostatic energy near the surface. The reverse spikes are in the opposite magnetisation direction to the spike domains. However, the spike domains and reverse spikes are associated with strong repulsive and attractive stray fields respectively acting on the tip, and this indicates high and low stray fields in their regions compared to the main domains.

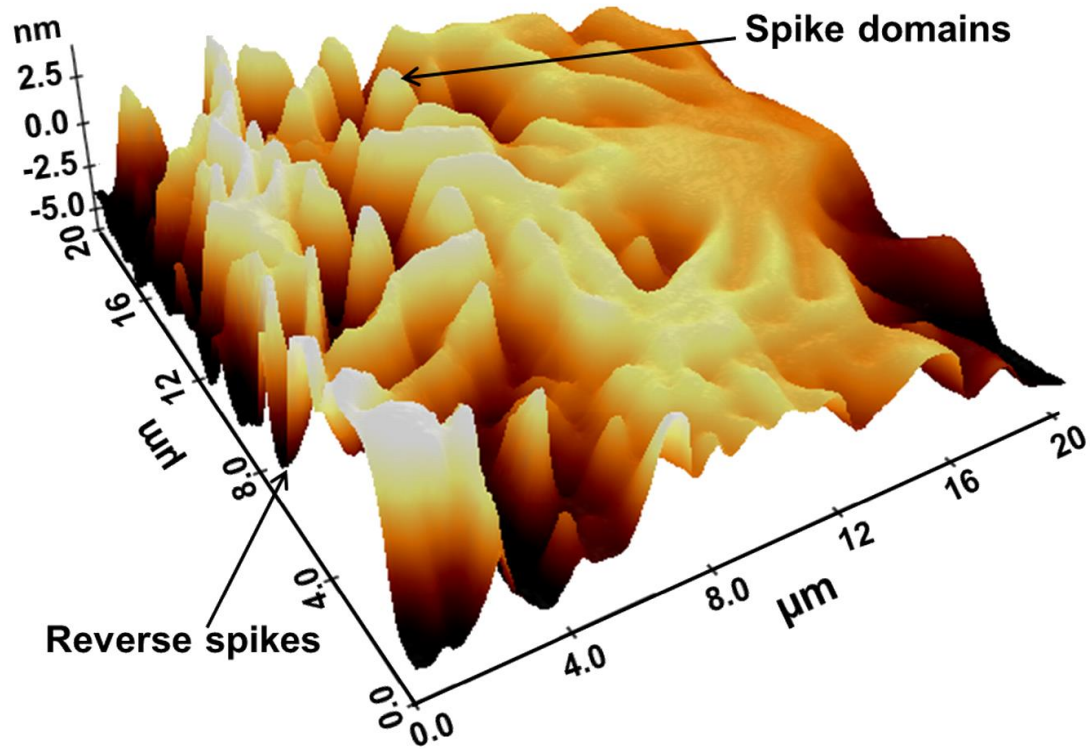

Figure 4-14 3D view of sintered Nd-Fe-B domain structure observed on the surface perpendicular to alignment axis.

The spike domains and reverse spikes appear in the sintered SmCo magnets on the surface perpendicular to the alignment axis. In addition to maze-like patterns, stripe-like patterns and branch-like patterns observed for SmCo magnets, Fig. 4.15 shows some domains appear on the surface perpendicular to the alignment axis as spikes and reverse spikes or domains. The spike domains and reverse spikes for sintered SmCo are compared with those found on sintered Nd-Fe-B permanent magnet materials. Fig. 4.15 illustrates the appearance of magnetic domain structure in 3D MFM images of the perpendicular alignment axis for sintered SmCo magnet types. The 3D data explain the domain structure more clearly. The 3D MFM images show that a different microstructure is present for each of the samples.

In $SmCo_5$ and Sm_2Co_{17} (B) samples, with wider magnetic domains, some magnetic domains appear as spontaneous vortices or spikes elongated vertically along the magnetically aligned direction. These locations are associated with a strong repulsive force acting on the tip with a positive force gradient, indicating a high stray field in these regions. Nevertheless, the spikes within the main domains appear to follow the bends of some maze domains in the 3D view. Meanwhile the samples of Sm_2Co_{17} (A and C) have narrower magnetic domains, and the reversed domains emerge as reverse spike regions in the 3D view. These reveres spikes are connected

with a strong attractive force acting on the tip with a negative force gradient that show a low stray field in their regions.

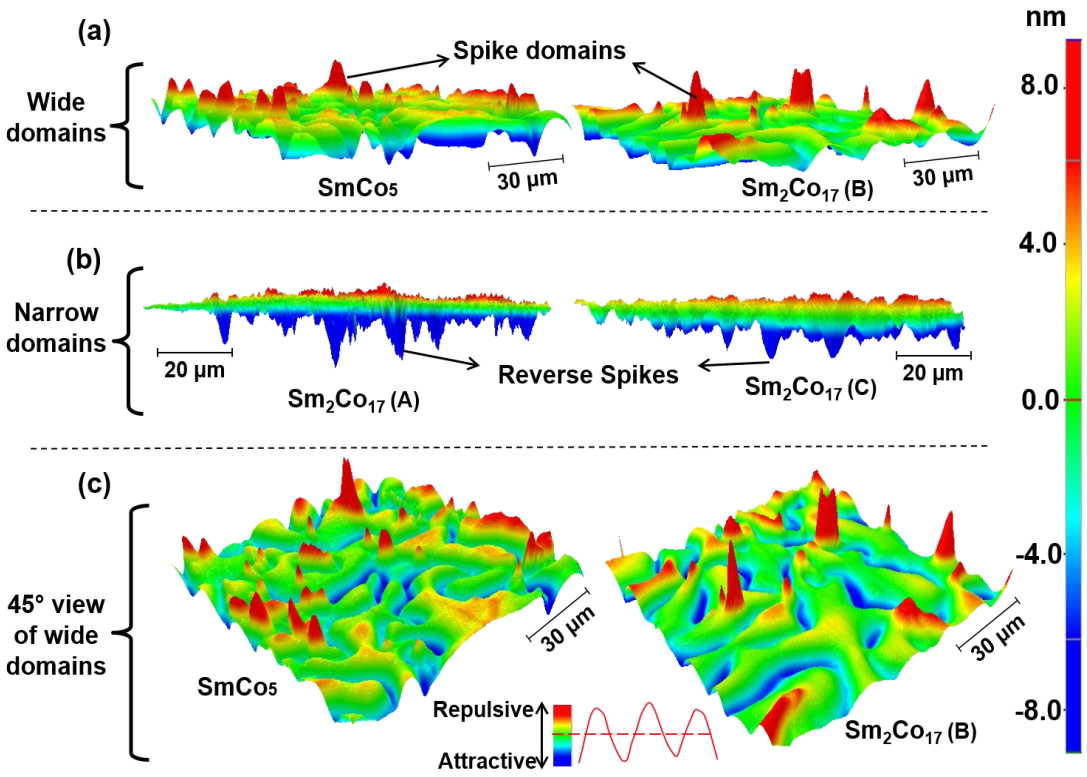

Figure 4-15 MFM images taken in the perpendicular alignment axis showing the appearance of spike domains and reverse spikes in 3D. Different behaviour for $SmCo_5$ and Sm_2Co_{17} (A, B and C) samples is shown. In (a), $SmCo_5$ and Sm_2Co_{17} (B), with wider magnetic domains, the spike patterns appear as spontaneous vortices or spikes elongated vertically along the magnetically aligned direction (positive force gradient). In (b), Sm_2Co_{17} (A and C), with narrower magnetic domain, the reversed domains emerge as reverse spikes in 3D rendering (negative force gradient). In (c), a 45° view is presented of samples shown in (a).

The schematic representation of spike domains and reverse spikes for Sm_2Co_{17} magnets has been described by Li. *et al* [91]. The author reported that the reduction of magnetostatic energy is caused by the appearance of corrugation and reverse spike domains. In addition, Iavarone et al [100], reported the observation of vortices in wider magnetic domains and uniform reversal regions in narrower domains, using scanning tunnelling microscopy. The samples consisted of different Co/Pd multilayers.

Furthermore, the 3D view of typical region of spike and reverse spike domain for the magnets studied are shown in Fig. 4.16. The MFM images are from a small region and taken with a high resolution. The upper row of Fig. 4.16 represents the spike domains for $SmCo_5$ and Sm_2Co_{17} (B), while lower row represents the reverse spikes for Nd-Fe-B and Sm_2Co_{17} (A and C). These figures are used for determining the

shape of spikes and reverse spikes that appear as circular truncated cones. The spike domains and reverse spikes are in opposite magnetisation direction to each other.

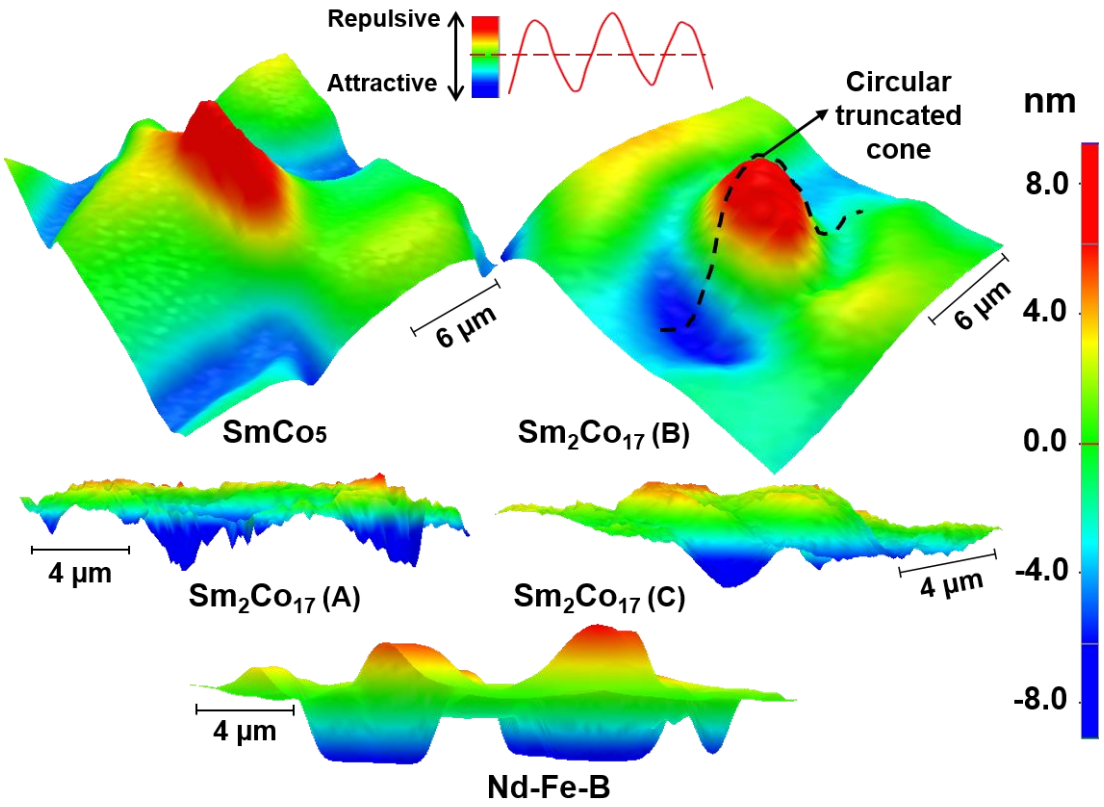

Figure 4-16 3D view of small regions of spike and reverse spikes within MFM images at high scale for different sintered SmCo magnets.

These results suggest that whether spike or reverse spikes are generated depends on the magnetic domain structure. They indicate the stray magnetic field acting on the MFM tip from the underlying magnetic domains.

The spike domains and reverse spikes reduce the domain wall energy, generate a strong surface anisotropy, and may reduce the density of magnetostatic energy near the surface. These domain patterns may affect the magnetocrystalline anisotropy which is the source of coercivity, leading to have an impact on coercivity. Therefore, the observation of spike domains and reverse spikes is an important step in order to control their appearance over the surface.

4.7 Summary

The chapter has described the use of the MFM technique to characterise the domain microstructure of sintered Nd-Fe-B and SmCo magnets. Observations are made at surfaces perpendicular and parallel to the alignment axis. Maze-like magnetic domains and stripe magnetic domains are observed in the perpendicular and parallel surfaces respectively. MFM images illustrate the grains of Nd-Fe-B magnets, and indicate the multi-domain structures within individual grains. Branch-like domains are observed for sintered Nd-Fe-B and Sm_2Co_{17} magnets in the parallel alignment axis. The domain structures have been analysed for the first time in the 3D view. The 3D MFM images exhibited that a different microstructure is present for each of the samples. The MFM images have shown important micro-magnetic structural characteristics such as spike domains and reverse spikes in the 3D view. The appearance of spikes domains and reverse spikes indicate the stray magnetic field acting on the MFM tip from the underlying magnetic domains. The spike domains and reverse spikes reduce the domain wall energy, generate a strong surface anisotropy, and may reduce the density of magnetostatic energy near the surface. It has been suggested that the spikes and reverse spikes may affect the magnetocrystalline anisotropy, which is the source of coercivity, leading to have an impact on coercivity. Therefore, the observation of spike domains and reverse spikes is an important step in order to control their appearance over the surface.

The observation of magnetic domain microstructure of sintered NdFeB and SmCo magnets has been reported in this chapter. However, it is vital to determine the microstructure parameters from these observations, such as domain wall width and domain wall energy. The following chapter considers the evaluation of the magnetic domain width and domain wall energy for all types of sintered permanent magnets studied.

CHAPTER 5 DETERMINATION OF MICROSTRUCTURE PARAMETERS

5.1 Introduction

Microstructural variables such as grain size, domain width and phase morphology have a strong influence on coercivity and remanence. It is known experimentally that the coercivity (H_c) of a magnetic material varies inversely with grain size (D) [25, 63-65], and the grain sizes change with domain size. From the phenomenological model explained earlier (section 2.9.2, equation 2.8), the coercivity of permanent magnet materials is influenced by domain wall energy (γ_w). The domain wall energy and exchange constant of materials are calculated from the measurement of domain width.

In this context, this chapter discusses the determination of domain width and domain wall energy in the parallel and perpendicular alignment directions. In addition, the ratio of root-mean-square values for MFM phase images ($Ø^{\perp}/Ø^{//}$) is found to be an indicator for predicting the variation on magnet properties of the studied samples. The ratio of $Ø^{\perp}/Ø^{//}$ is determined in both direction alignment, parallel and perpendicular.

5.2 Determination of the main domain width

The main domain width and domain wall energy are very important microstructural parameters for determining the magnetic properties of magnet materials. The coercivity (H_c) of a magnetic material varies inversely with grain size (D) [25], and the grain size changes with domain size. The domain wall energy and exchange constant of materials are calculated from the measurement of domain width.

It is not easy to determine the domain width using visual methods for materials such as the Nd-Fe-B magnet with complicated domain patterns. Therefore, a digital method has been applied to obtain the main domain width.

The domain width is determined based on the stereological method proposed by Rudolf and Hubert [60]. The procedure of the stereological method is described in section 3.6.2. The expression of the method is:

$$D_W = \left(\frac{2}{\pi}\right) \times \left(\sum_i l_i\right) / \left(\sum_i n_i\right) \tag{5.1}$$

where l_i is the length of the i^{th} test line and n_i is the number of intersections of the i^{th} test line with the domain walls.

Firstly the MFM images of the sintered Nd-Fe-B and SmCo magnets are transferred to a black and white area to suit Matlab software. The Matlab coding is shown in Appendix A. The images are enhanced using the XEI digital imaging process. The procedure of XEI software has been discussed earlier in section 3.6.1. Fig. 5.1 shows the procedure for applying the stereological method to MFM images of sintered Nd-Fe-B magnets as an example. After that, more than 1000 test lines are applied in the images based on random directions (100 test lines are shown in Fig. 5.1). The length of each line, the total length of test lines and the number of intersection points have been accurately determined. The procedure was repeated 10 times for each image in order to evaluate the accuracy of the determination of domain width. The domain width is determined in this image as 0.78μm and classified as a fine domain structure.

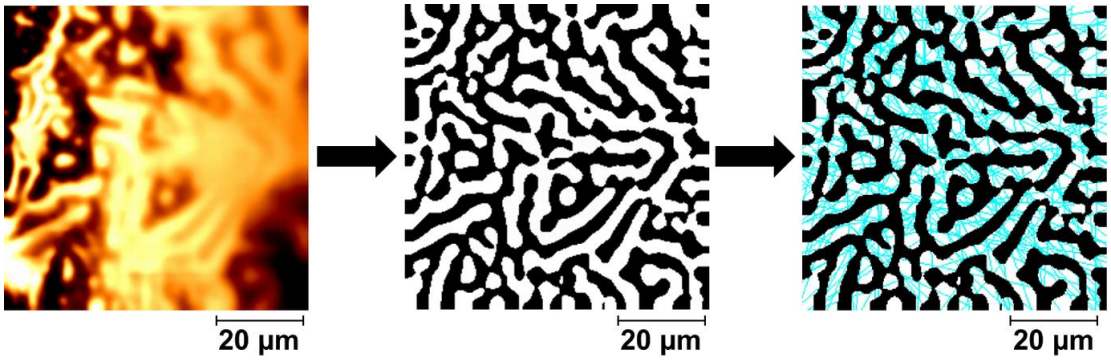

Figure 5-1 100 test lines applied to an MFM image in the stereological method**.** The MFM image is for sintered Nd-Fe-B magnet and enhanced using XEI software to be readable by Matlab.

In this work, domain width is determined in both the parallel and perpendicular directions. Most previous investigations have evaluated domain width on the surface perpendicular to the alignment axis. The determination of domain width in the parallel direction has been reported only once for die-upset Nd-Fe-B magnets [101]. The experimental values of domain width were used to evaluate the domain wall energy in both directions. Fig. 5.2 shows the procedure for applying the stereological method to MFM images in direction parallel to the alignment axis. The sintered Sm_2Co_{17} magnet is taken as an example in Fig.5.2 to illustrate the procedure.

The domain width is determined in this image as 3.5µm and classified as a coarse domain structure.

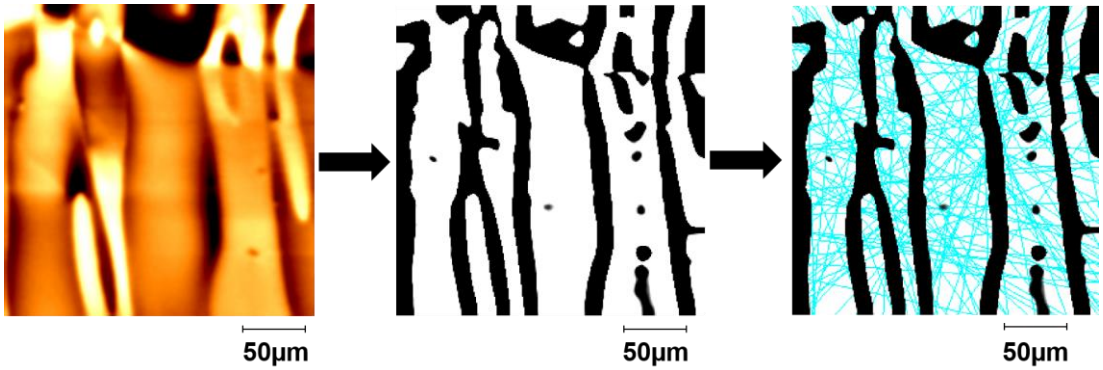

Figure 5-2 100 test lines applied to an MFM image in the stereological method. The MFM image is for sintered Sm_2Co_7 (B) magnets in the direction parallel to the alignment axis. The image is enhanced using XEI software to be readable by Matlab**.**

The stereological method for domain width determination has been applied for all proposed magnets. A comparison of domain width between the perpendicular and parallel directions is shown in Fig. 5.3 for each type of sample. It can be seen from the figure that the samples of sintered Nd-Fe-B and Sm_2Co_{17} exhibit a fine domain width comparing to $SmCo_5$ and Sm_2Co_{17} (A, B). The domain width of sintered Nd-Fe-B magnet is 0.78 ± 0.01µm in perpendicular alignment axis ($D_w^{\perp}$) and 1 ± 0.1µm in parallel direction (D_w //). The value of $D_w^{\perp}$ for $SmCo_5$ is 1.25 ± 0.01µm, while for Sm_2Co_{17} A, B and C, the values are 0.58 ± 0.01µm, 2.06 ± 0.02µm, and 0.34 ±0.01µm respectively. Domain width in the parallel direction (D_w //) for $SmCo_5$ is 2.32 ±0.02µm while for Sm_2Co_{17} samples, it lies in the range of 0.89 - 3.5µm. In general, all the samples exhibit different domain width from each other according to the microstructure of the magnet. The domain width in the parallel alignment axis is higher than the direction perpendicular to the alignment axis, which lead to a higher domain wall energy produced in the parallel side. Therefore, it could be important to determine the domain width in the parallel alignment axis.

The domain width determined in this section is used to calculate the energy of domain wall for each type of magnets. Next section shows the determinations of domain wall energy of all the proposed sample.

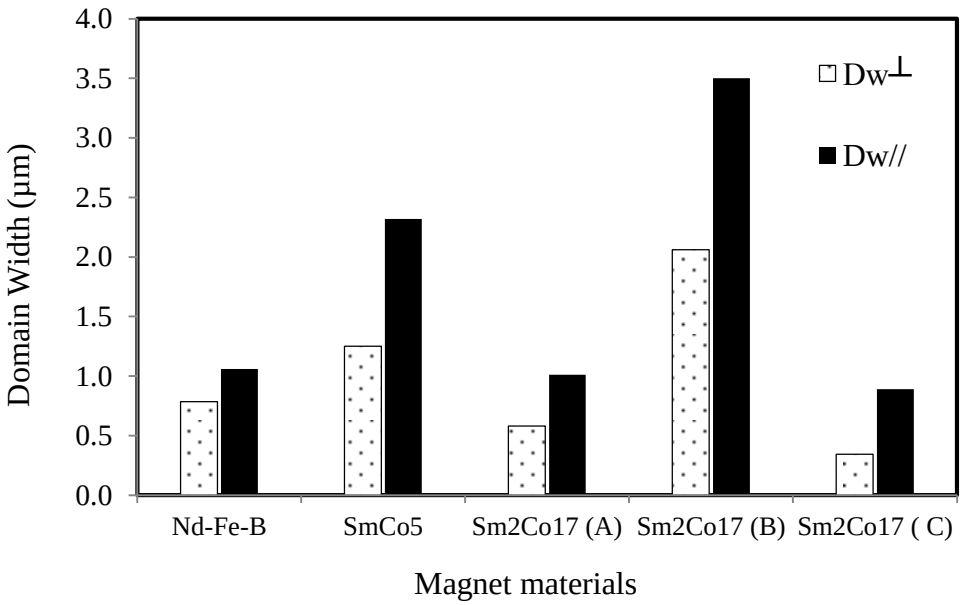

Figure 5-3 Determination of domain width for sintered Nd-Fe-B and SmCo magnets in directions perpendicular and parallel to the alignment axis**.**

5.3 Domain wall energy determination

Domain wall energy is a fundamental microstructure parameter that is related to the coercivity of materials. It is approximately the sum of magnetic anisotropy energy and exchange energy. From the phenomenological model explained earlier (section 2.9.2), the coercivity of permanent magnet materials is influenced by domain wall energy (γ_w). The knowledge of magnetic domain microstructure can be used to achieve the domain wall energy. The domain wall energy can be obtained on the basis of investigations of the magnetic domain structure. The domain wall energy and exchange constant of materials are calculated from the measurement of domain width. In addition the knowledge of domain wall energy allows to determine the exchange constant of materials.

Domain wall energy (γ_w) has been evaluated according to the model proposed by Bodenberger and Hubert [61] from the expression:

$$\gamma_w = \frac{D_w (M_s)^2}{4\pi\beta} \tag{5.2}$$

where: D_w is the determined domain width and M_S is the magnetisation saturation with values shown in table 5.1. The coefficient β is estimated depending on the

surface structure, and its value has been previously determined as 0.31 for $SmCo_5$ and similar magnetic materials with high magnetocrystalline anisotropy [61].

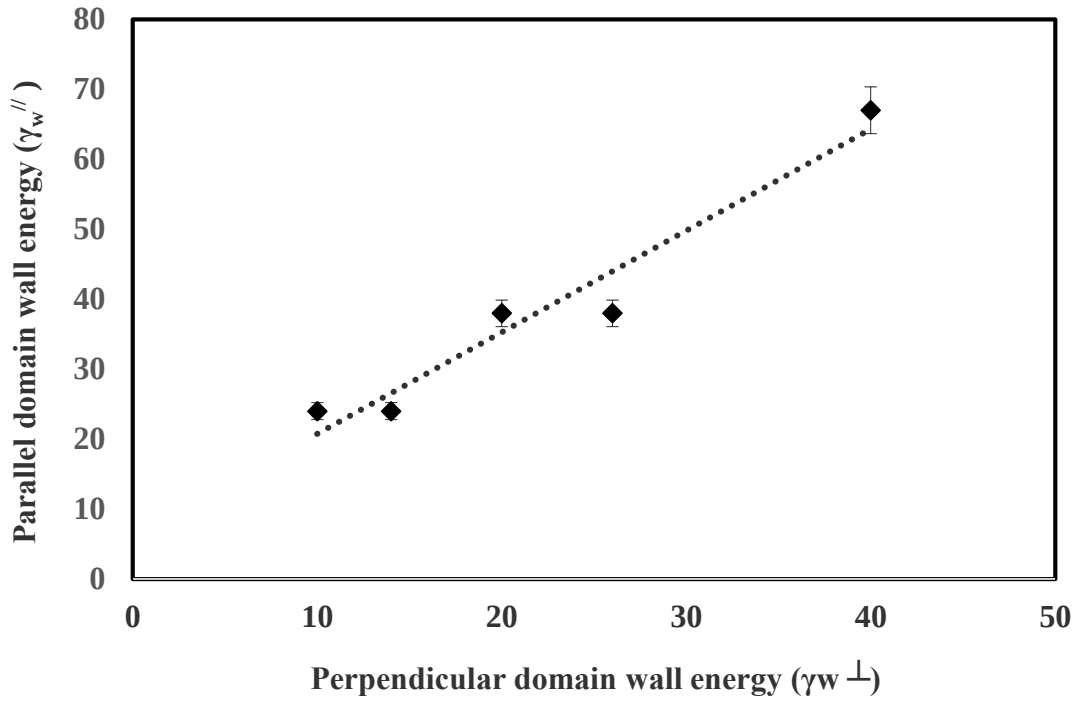

Figure 5-4 Domain wall energy for all the proposed samples, determined in directions both perpendicular and parallel to the alignment axis using MFM.

The domain wall energy is determined for all types of magnet materials in both alignment directions. Fig. 5.4 shows the energy of domain wall for the proposed samples (sintered Nd-Fe-B and SmCo magnets). The domain wall energy (γ_w) for a sintered Nd-Fe-B magnet is 26erg/cm^2 in the perpendicular direction and 38erg/cm^2 in the parallel direction. The previously reported values of Nd-Fe-B domain wall energy in the perpendicular direction are γ_w= 35erg/cm^2 as estimated by Livingston [97] and γ_w= 33erg/cm^2 by Szymczak *et al.* [102]. These early results are very close to the value of γ_w= 26erg/cm^2 obtained in this research. In addition, the values of domain wall energy for sintered $SmCo_5$ and Sm_2Co_{17} magnets are determined to be in the range of 10 to 40erg/cm^2 on the perpendicular surface and from 24 to 67erg/cm^2 on the surface parallel to the alignment axis.

The domain wall energy is evaluated from MFM images in order to be used for the analysis of magnetic properties. The results for all the samples show clear difference in the domain width and domain wall energy in perpendicular and parallel directions. However some samples exhibit similarities in domain wall energy, such as Sm_2Co_{17} (A) and (C).

Therefore it is important to understand the differences in domain width and domain wall energy by comparing all of the samples in one table for both directions, as presented in the next section.

5.4 Comparison of domain width and domain wall energy on perpendicular and parallel alignment axes

In order to evaluate the differences in domain width and domain wall energy between the samples, the results in previous section are shown in one table for both directions, perpendicular and parallel to the alignment axis. Table 5.1 shows the microstructural parameters such as domain width and domain wall energy of each sample studied. The magnetic properties in terms of coercivity H_c and magnetisation saturation M_s are also listed in table 5.1.

Table 5-1 Main domain width and domain wall energy in both direction alignments

Samples	M_S (T)	H_c (k A/m)	$^aD_w\perp$ (μm)	D_w // (μm)	$^a\gamma_w\perp$ erg/cm^2	$\gamma_w^{//}$ erg/cm^2
Nd-Fe-B	1.44	1058	0.78 ± 0.01	1.0 ± 0.1	26	38
$SmCo_5$	1	750	1.25 ± 0.01	2.32 ±0.02	20	38
*Sm_2Co_{17} (*A)	1.2	780	0.58 ± 0.01	1.01 ± 0.01	14	24
Sm_2Co_{17} (B)	1.1	560	2.06 ± 0.02	3.5 ± 0.01	40	67
Sm_2Co_{17} (C)	1.3	865	0.34 ±0.01	0.89 ± 0.01	10	24

^aD_w = the effective main domain width in directions perpendicular '$\perp$' and parallel '//' to the alignment axis; μm= micro-metre; and γ_w= domain wall energy evaluated in both directions.

On the whole, a surface parallel to the alignment axis exhibits a higher domain width and energy compared to that in the perpendicular direction. This is due to the difference in the demagnetisation field. The table shows that the sintered Nd-Fe-B magnet exhibits fine domain structures in both directions, with values of 0.78 ± 0.01μm and 1 ± 0.1μm respectively in directions perpendicular ($D_w\perp$) and parallel (D_w //) to the alignment axis. The value of $D_w\perp$ for $SmCo_5$ is 1.25 ± 0.01μm, while for Sm_2Co_{17} A, B and C, the values are 0.58 ± 0.01μm, 2.06 ± 0.02μm, and 0.34 ±0.01μm respectively. Domain width in the parallel direction (D_w //) for $SmCo_5$ is 2.32 ±0.02μm while for Sm_2Co_{17} samples, it lies in the range of 0.89 - 3.5μm. However, the domain width and domain wall energy for the sintered Nd-Fe-B and

SmCo magnets in the direction parallel to the alignment axis have been determined for the first time here.

The results show that just changing the annealing temperature can have a major effect on the domain width and domain wall energy that leads to change the magnetic properties. The data also show the necessity to observe the domain width and wall energy in both alignment axes. The values of domain wall width and domain wall energy are evaluated from MFM images in order to be used for the analysis of magnetic properties. In addition it has been previously stated that the MFM images can be used as an indicator for the magnetic property of the magnets. Next section estimates the variation of magnetic properties from MFM images for the different samples.

5.5 Estimation of the variation of magnetic properties using MFM

The MFM images have been used to estimate the magnetic properties of magnet materials [103, 104]. A good indicator of the magnetic properties of magnet materials is the ratio of root-mean-square values ($Ø_{r,m,s}$) for the phase shift from the MFM images [101, 104]. The phase shift between the cantilever response and the drive voltage is measured by MFM images. As the tip is repulsed or attracted by the magnetic force of the sample, the resonant frequency of the cantilever changes, which leads to the variation in image contrast. The variation in the contrast of phase image represent the mapping of magnetic force gradient. In this case, the contrast of the MFM image is proportional to the magnetisation of the sample surface.

The root-mean-square value ($Ø_{r,m,s}$) represents the contrast in magnetic force images. The standard deviation of phase shift (Ø) is represented by the value of root-mean-square ($Ø_{r,m,s}$) of the scanned area. The $Ø_{r,m,s}$ is calculated using the expression:

$$\phi_{r,m,s} = \sqrt{\frac{\sum_{i=1}^{N}(\phi_i - \phi_{avg})^2}{N}} \qquad (5.3)$$

where: $Ø_{avg}$ is the average value of roughness for the MFM image, $Ø_i$ is the current i^{th} of the value of ϕ value, and N is the number of pixels within the MFM image.

It has been found by Fang *et al*. [101] that the ratio of the perpendicular ($Ø^{\perp}$) value to the parallel ($\phi^{//}$) value is a better indicator for the variations in the magnetic properties of the materials. The samples were die-upset Nd-Fe-B magnets. The

higher the $Ø^{\perp}$/ $Ø^{//}$ ratio, the better the magnetic properties achieved. In addition, Yue *et al*. [103] proved that there is a correlation between the coercivity H_c or maximum energy product and $Ø_{r,m,s}$ value. The highest $Ø_{r,m,s}$ value for different Zr_2Co_{11}-based magnets was found at the largest coercivity and energy product sample.

Hence, the root-mean-square phase shifts of the MFM images are determined using roughness analysis for both parallel and perpendicular directions and are shown in table. 5.2. The highest $Ø^{\perp}$/ $Ø^{//}$ ratio of 3.2° for Nd-F-B is in agreement with the largest coercivity of 1058 kA/m. The highest $Ø_{r,m,s}$ ratio of 3.0° for the different SmCo magnets is found for the Sm_2Co_{17} (C) sample at coercivity value of 865 kA/m. This indicates that the Sm_2Co_{17} (C) sample has the best magnetic properties among the SmCo specimens studied. The perpendicular surface alignment shows a higher root mean square value than the parallel surface because the perpendicular stray field is higher than that in the parallel. The ratios of $Ø_{r,m,s}$ values for the sintered Nd-F-B and SmCo magnets have been determined for the first time here. In addition, samples with narrower domain sizes exhibit higher ratios of $Ø_{r,m,s}$ value than those with wider domain sizes. These results indicate that the domain size plays an important role in achieving better magnetic properties.

Table 5-2 Root-mean-square ($Ø_{r,m,s}$) values of phase MFM images, as a magnetic property indicator**.**

Samples	M_S (T)	H_c (k A/m)	$Ø_{r,m,s}^{\perp}$ (°)	$Ø_{r,m,s}^{//}$ (°)	$Ø^{\perp}$ / $Ø^{//}$
Nd-Fe-B	1.44	1058	10.6 ± 0.01	3.3 ± 0.01	3.2
$SmCo_5$	1	750	6.4 ± 0.01	6.1 ± 0.01	1.1
*Sm_2Co_{17} (*A)	1.2	780	2.5 ± 0.01	1.7 ± 0.01	1.5
Sm_2Co_{17} (B)	1.1	560	3.4 ± 0.02	1.6 ± 0.02	2.1
Sm_2Co_{17} (C)	1.3	865	0.79 ±0.01	0.26 ± 0.01	3.0

5.6 Summary

This chapter has described the determination of microstructural parameters, such as domain width and domain wall energy, for sintered Nd-Fe-B and SmCo magnets. The effective domain width and domain wall energy have been determined in surfaces both perpendicular and parallel to the alignment axis. The sintered Nd-Fe-B magnet exhibited fine domain structures in both directions, with values of 0.78 ± 0.01μm and 1 ± 0.1μm in directions perpendicular and parallel to the alignment axis respectively. The SmCo magnets have a domain width varies in the range of 0.3 – 2.1μm in the perpendicular direction and 0.89 - 3.5μm in the parallel direction. On the whole, a surface parallel to the alignment axis exhibits a higher domain width and energy compared to that in the perpendicular direction. The results showed that just changing the annealing temperature can have a major effect on the domain width and domain wall energy that leads to change the magnetic properties.

In addition, the variation of magnetic properties for the proposed magnets has been evaluated using MFM phase images. It has been found that the ratio of root-mean-square values for MFM phase images ($Ø^{\perp}/Ø^{//}$) is a good indicator of the variation of magnetic properties. These insight will help to indicate the magnetic properties of the materials using MFM.

Next chapter will discuss the influence of interfacial microstructure on the domain wall dynamic for the proposed sintered Nd-Fe-B magnets.

CHAPTER 6 EFFECT OF GRAIN SEPARATION ON DOMAIN PATTERNS FOR SINTERED ND-FE-B

6.1 Introduction

Understanding the magnetic microstructure of sintered Nd-Fe-B is vital for the development of high performance magnets. The magnetic microstructure of Nd-Fe-B based magnets is determined by the crystalline microstructure. The crystal structure of sintered Nd-Fe-B magnets consists of mainly a hard magnetic $Nd_2Fe_{14}B$ matrix and grain boundary phases. The grain boundary phase separates the hard magnetic grains from each other and prevents magnetic interaction between grains. Usually, a paramagnetic Nd-rich phase is added as an insulation layer between the grains and is located at the boundary and triple junctions. In this context, this chapter discusses the effect of grain separation on domain patterns of the proposed sintered Nd-Fe-B magnet, observed using MFM technique.

Novel distorted regions on the topographic image are observed which have a clear effect on MFM image. The effect of these distorted regions on the domain walls is studied for the first time using MFM. These regions have been identified using Raman spectroscopy. In order to study the dynamic behaviour of distorted regions, the condition of observation has to be changed. This chapter studies the impact of increasing temperature on the distorted regions. In-situ distorted regions of sintered Nd-Fe-B magnet are observed using MFM method at high temperature up to 80°C. Furthermore the observation of distorted regions at different locations of the same sample surface are presented at elevated temperature up to 120°C. The distortion regions have been illustrated in 3D view. The size of distorted domain walls is determined at each degree of temperature using two different methods in XEI digital imaging software. These methods are the 2D line profile and watershed technique, and are explained in detail. Raman spectroscopy is carried to identify the variation of distorted regions with temperature.

Finally, the change of domain wall size with temperature is shown in this chapter.

6.2 Crystal microstructure of the studied sintered Nd-Fe-B sample

The magnetic microstructure of Nd-Fe-B based magnets is determined by the crystalline microstructure. The crystal structure of sintered Nd-Fe-B magnets consists of mainly a hard magnetic $Nd_2Fe_{14}B$ matrix. The hard $Nd_2Fe_{14}B$ magnetic phase is tetragonal in shape with uniaxial crystalline anisotropy. The grain boundary phase separates the hard magnetic grains from each other and prevents magnetic interaction between grains. Usually, a paramagnetic Nd-rich phase is added as an insulation layer between the grains and is located at the boundary and triple junctions. However, in order to identify the different phases of the sintered Nd-Fe-B magnet, X-ray diffraction (XRD) has been performed at room temperature.

The XRD results of the sintered Nd-Fe-B magnet are depicted in Fig. 6.1. The majority phase is the main $Nd_2Fe_{14}B$ phase with a percentage of 98%. Other phases are identified with low percentages, such as Nd- rich and Nd_2O_3.

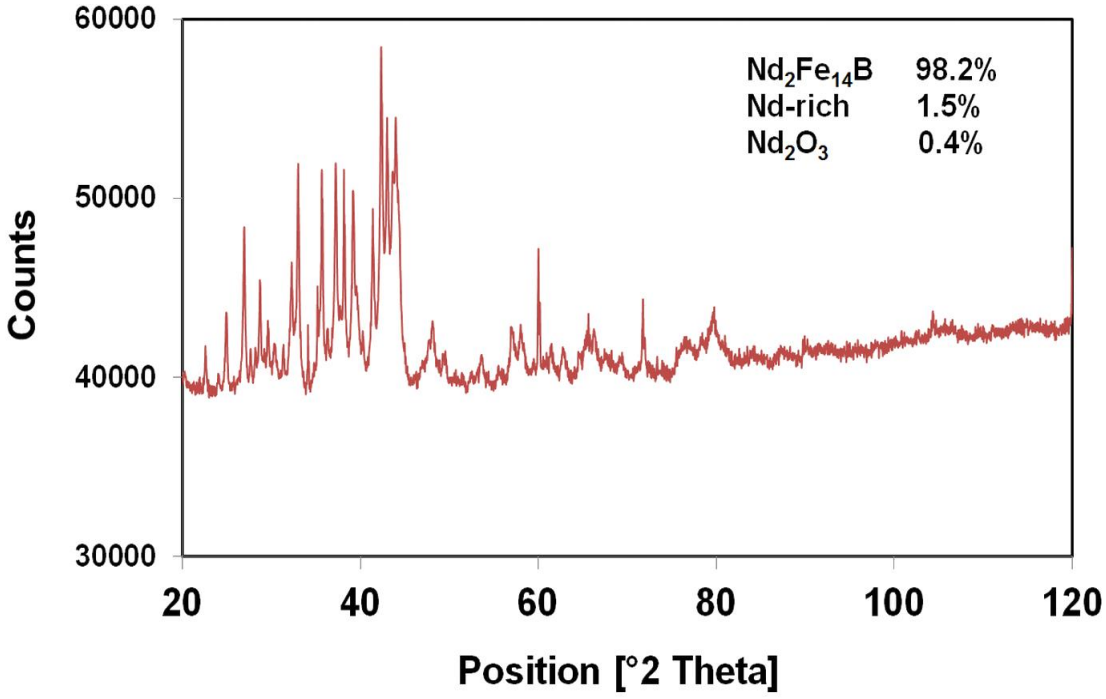

Figure 6-1 Experimental XRD data for the investigated sintered Nd-Fe-B magnet.

The XRD findings are also supported by scanning electron microscopy (SEM) analysis of sintered Nd-Fe-B, as shown in Fig. 6.2, which shows the microstructure of the sample with the existence of Nd-rich spots and layers at triple junctions. The grey area represent the grain structure, which is mainly the hard $Nd_2Fe_{14}B$ magnetic phase. This phase is responsible for the magnetic properties of the magnet. The white area (between the grains and at triple junctions) is the grain boundary phases

and identified as Nd-rich regions. The grain boundary phases have a major impact on magnet coercivity and performance.

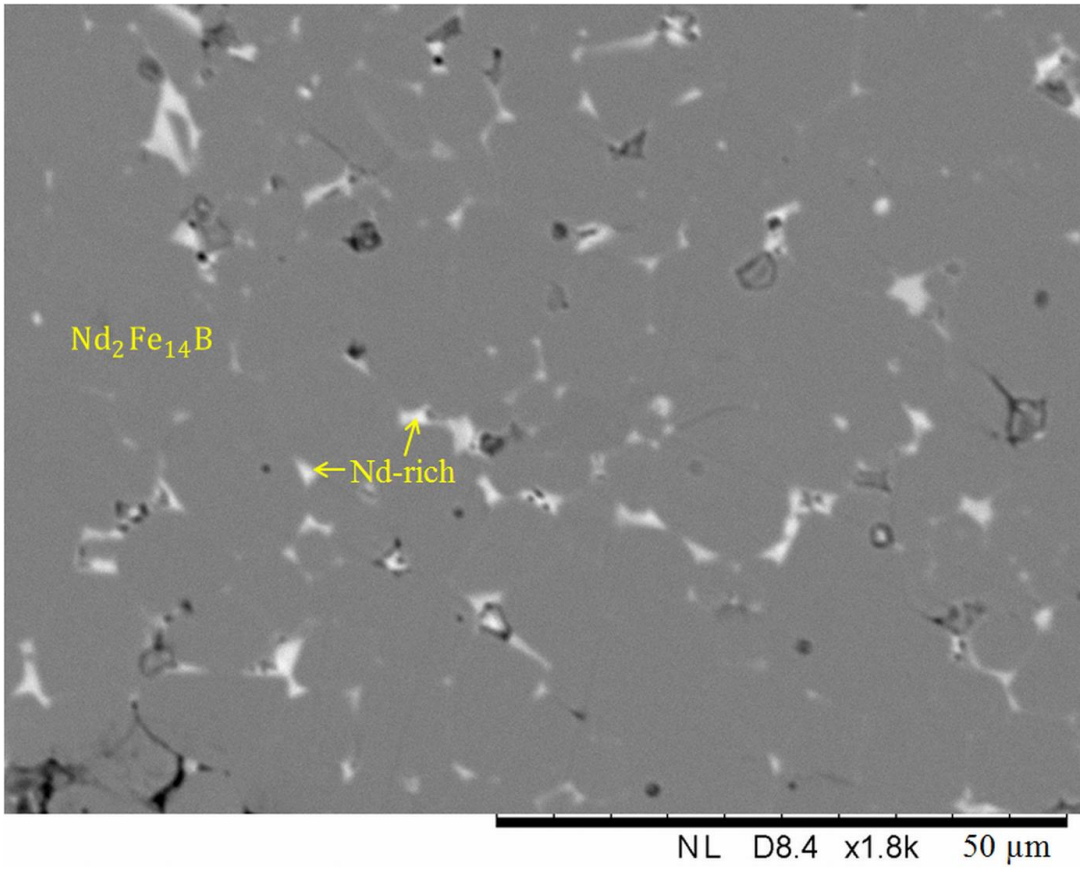

Figure 6-2 Scanning electron microscopy (SEM) image of sintered Nd-Fe-B magnet.

The XRD and SEM analysis of the sample of sintered Nd-Fe-B, provides information on the grain and grain boundary structure. In the next section, the impact of the structure of grain separation on domain walls is studied using MFM.

6.3 Effect of interfacial distorted regions on the domain patterns

At certain locations on the surface, some interfacial distorted sites appear which have an impact on the domain structures by changing the domain patterns. Fig. 6.3 shows a typical microstructure of the Nd-Fe-B sintered magnet with interfacial microstructure distortions obtained in the direction perpendicular to the alignment axis. In Fig. 6.3, the topography image is on the left and the corresponding MFM image is on the right.

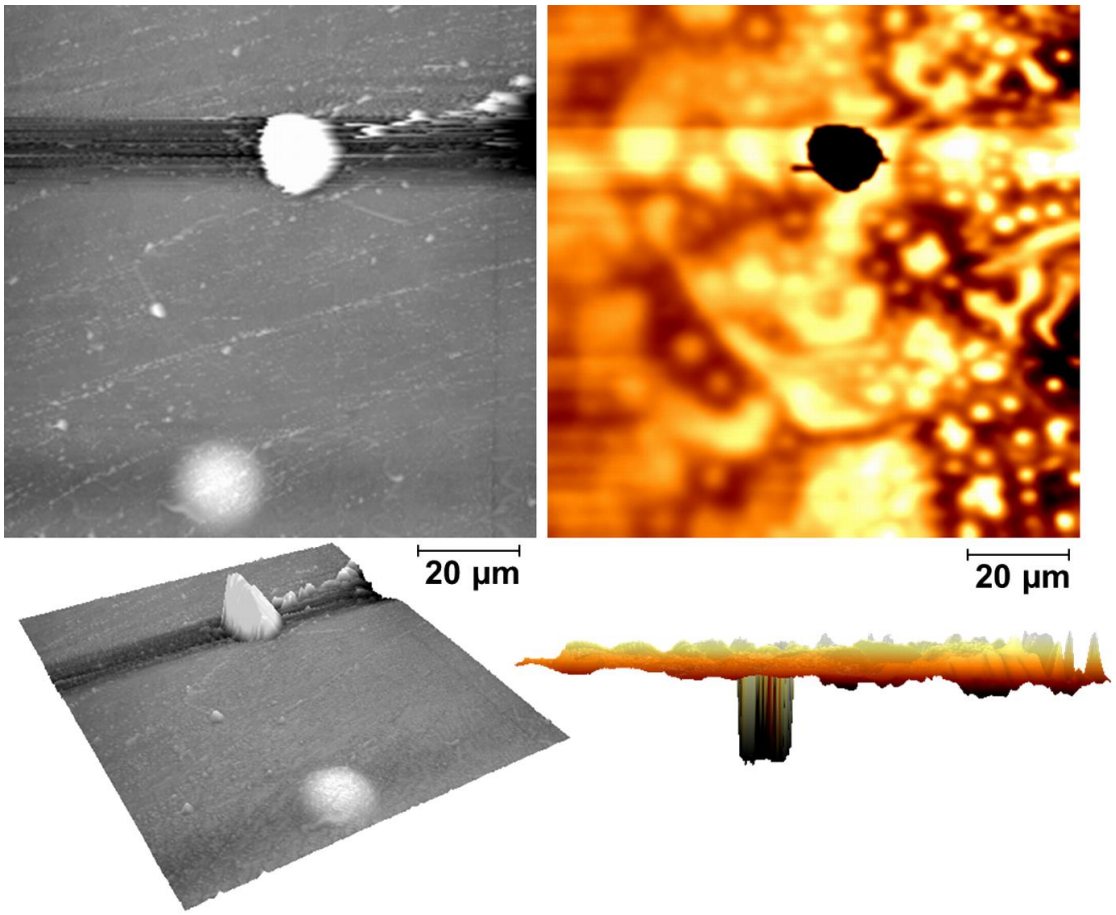

Figure 6-3 Magnetic domain structure of sintered Nd-Fe-B magnet with interfacial distorted regions appeared: topographic image (Left column); and MFM image (Right column).

There are dislocations or distortions in the topographic image which have a clear effect on the MFM image. The shape of these regions seems to be elongated vertically along the magnetically aligned direction. The domain wall on the MFM image appears as a reversal region in the 3D view with large size. The reversal site is associated with a strong attractive force acting on the tip with a negative force gradient, and this indicates a low stray field in these regions. The distorted sites are observed at different locations on the same surface of sintered Nd-Fe-B magnets, as shown in Fig. 6.4. The figure shows the influence on the domain patterns, resulted from the appearance of two distorted regions at different sites in the 3D view of the same sample.

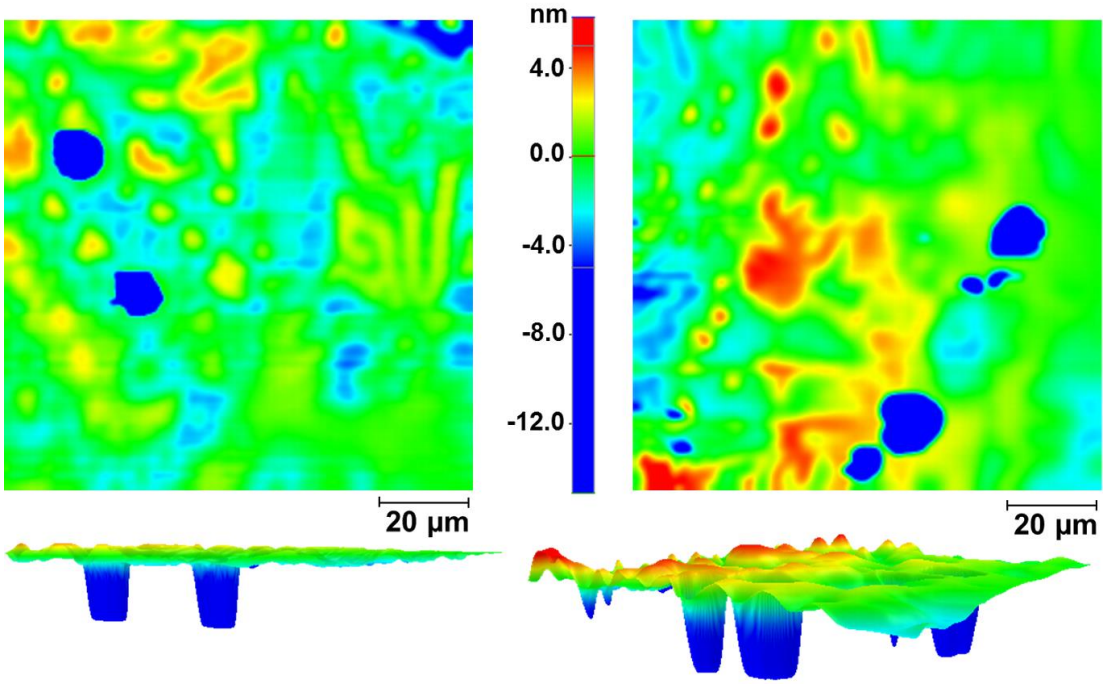

Figure 6-4 the influence on the domain patterns, resulted from the appearance of distorted regions in the 3D view at different locations of the sintered Nd-Fe-B magnets.

Furthermore, different areas have been imaged by MFM and are shown in Fig. 6.5. The dislocation sites are shown in 3D view within a smaller regions and a high scale. The figure shows four distorted regions and their corresponding sites of domain walls. The topographic images are in the upper row and the MFM images are in the lower row. The MFM images illustrate obvious reverse sites of magnetic domains in 3D view. The shape of the distorted regions seems to be elongated vertically along the magnetically aligned direction. These sites are associated with a strong attractive force acting on the tip with a negative force gradient, and this indicates a low stray field in their regions.

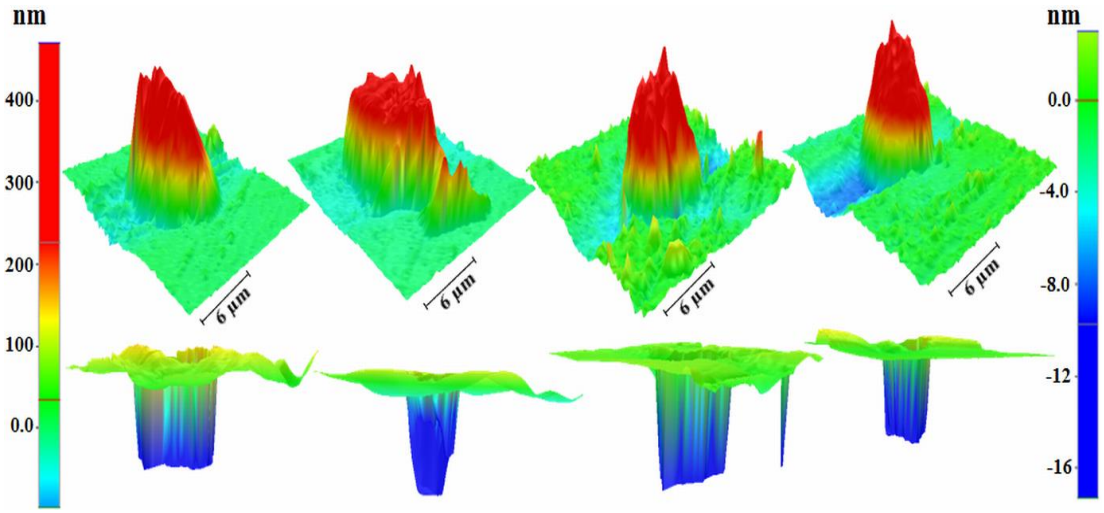

Figure 6-5 Four distorted regions (upper row) and their corresponding regions of domain walls (lower row) observed at different sample areas of sintered Nd-Fe-B magnet by MFM. These regions are shown in 3D within a smaller regions and a high scale**.**

The results show the appearance of surface topography with dislocation or distortion. These regions have an impact on domain wall patterns, hence, it is very important to identify the distorted regions in order to control their appearance on the surface. In this context, identifying these sites are discussed in the following section.

6.4 Identification of the distorted regions using Raman spectroscopy

Generally, the sintered Nd-Fe-B magnet contains some minor phases, such as Nd-rich phases, α-Fe, Nd oxides and pores which are located at the boundaries and junctions of the grains. Ono *et al*. [68] found that ferromagnetism is weak at the Nd-rich triple junctions. The authors suggested that, when an external field is applied, the reverse domains may appear as reversal sites in these regions. It has been reported that the defects are mainly generated from the non-uniform distribution of Nd-rich phases during the annealing process [7, 67]. The Nd-rich layer will block the movement of domain walls. Therefore, the uniform distribution of Nd-rich is highly important for the process of demagnetisation and magnetisation of the Nd-Fe-B magnet.

In addition, Sasaki *et al*. [31] confirmed that the Nd_2O_3 grains at triple junctions are defined as misaligned grains that minimize the magnetostatic energy. The demagnetization state is initiated from these misaligned grains. Hrkac *et al* [69, 70] found that the large distortion is expected to be from the oxide Nd_2O_3. The distorted sites decrease the magnetic anisotropy of the main phase. The authors suggested that

the removing the Nd_2O_3 phases from the microstructure could lead to produce a high coercivity magnet.

The MFM images in previous section show the appearance of surface distortion sites that have an impact on domain patterns. The MFM images indicate the effect of the distorted regions on magnetic domains, where the domain wall size is changed. It is important to identify these regions. According to SEM results in section 6.2 (Fig. 6.2), the grain structure of the studied sintered Nd-Fe-B magnet consists of main $Nd_2Fe_{14}B$ phase and Nd-rich phase. The Nd-rich regions are located at grain boundary and triple junction. In addition, it is identified using XRD in Fig. 6.1, that other phases such as Nd-rich and Nd_2O_3 are exhibit in the structure of proposed sample with low percentage.

Raman spectroscopy is applied to identify the distorted regions of a sintered Nd-Fe-B magnet. Fig. 6.6 shows the Raman trace of the sintered Nd-Fe-B magnet for four different areas (two distorted areas and two non-distorted). The spectra contain strong peaks appearing in the area between 150-600 cm^{-1} wave number regions, which match the peaks observed for pure Nd_2O_3. It is interesting to note that no peaks have been found on the planar, except at the triple junctions, during the process of spectroscopy. This may suggest that the distortion regions are oxides rather than metallic in character and identified as Nd_2O_3.

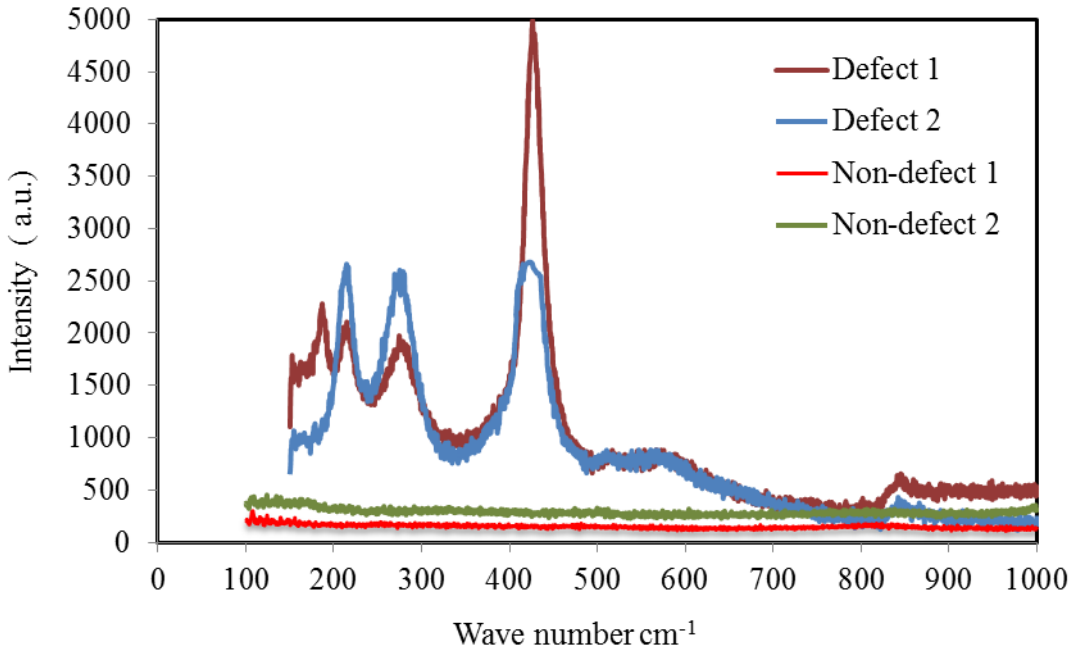

Figure 6-6 Raman spectroscopy signals for four different areas of sintered Nd-Fe-B surface

The Raman data identify the distorted regions that observed using MFM as Nd-rich regions and oxides in character. These regions have an impact on the movement of domain walls as it can be clearly shown from the observed MFM images. It is not known whether the effect of distorted regions on domain walls is continuing after changing the conditions of scan. However, it is vital to study the impact of different conditions on the observed regions such as varying temperature, which will be discussed in the next section.

6.5 The effect of high temperature on distorted regions

Most of the applications for sintered Nd-Fe-B magnets, such as the motors in hybrid and electric vehicles, are operating at high temperature around T=450K. The magnetic properties of magnet materials deteriorate with the increase of operating temperature. In order to study the dynamic behaviour of interfacial distorted regions observed in section 6.3, the condition of observation has to be changed. Therefore this section studies the impact of increasing temperature on the distortion regions using MFM technique.

The sintered Nd-Fe-B magnet is analysed at high temperature up to 120°C. The sample is studied close to thermally demagnetising state. The heat is applied using two different thermal stages and a detailed information on them are shown in section 3.5. In MFM analysis, the sample is heated in-situ up to 80°C, and at different locations up to 120°C. It has been found that the amplitude and direction of magnetisation for the MFM tips are significantly affected above 120°C. Therefore the thermal analysis is carried out up to 120°C. The MFM measurements are conducted in-situ and at different locations for the same sample surface of sintered Nd-Fe-B magnet as shown in the following sections.

6.5.1 In-situ observation of distorted regions with increasing temperatures

In-situ domain structure for sintered Nd-Fe-B magnet is observed at high temperature, with the appearance of interfacial distorted regions and their corresponding effected domain wall patterns. Fig. 6.7 illustrates the change of temperature from 20ºC to 80ºC applied in steps of 20ºC to the same location of distorted regions. The upper row of Fig. 6.7 represents the topography images with the appearance of distorted regions on the surface, while the lower row shows the MFM images with the visualising of the effected domain walls. The surface

distorted regions and their corresponding domain walls are grown with the increase of temperature. The change of the domain wall size is probably due to the decrease of magnetocrystalline anisotropy of the magnet as the temperature increase. There are no changes in the maze-like patterns as the temperature increased. The change of the interfacial distorted regions is higher at 80ºC comparing to 60ºC and 40ºC.

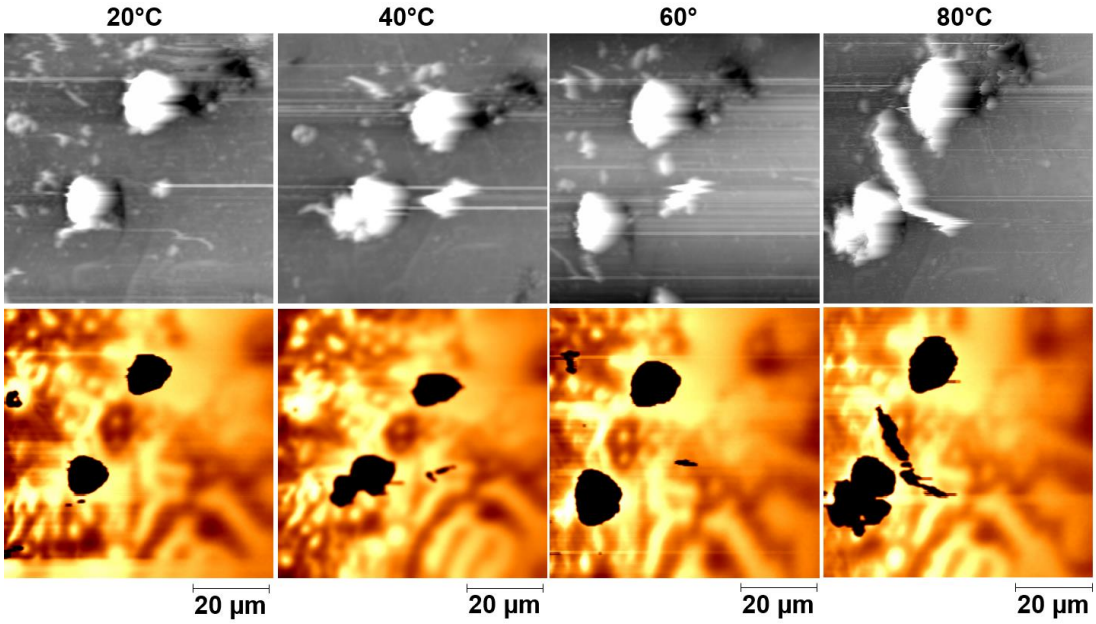

Figure 6-7 In-situ distorted regions and their corresponding domain walls for sintered Nd-Fe-B magnet captured using MFM method at different temperature up to 80°C.

The Raman data in section 6.4 identify the effected regions as Nd-rich regions and oxides in character. Therefore, Fig. 6.7 may indicate a diffusion in Nd-rich after applying the temperature. These results lead to produce high distortion on the surface which reduce the magnetocrystalline anisotropy.

Furthermore, the in-situ distortion regions and domain walls presented in Fig. 6.7 are illustrated in 3D view using XEI digital imaging process as shown in Fig. 6.8. The procedure of 3D mechanism is discussed in detail in section 3.6.1. This 3D view shows the change of distorted regions with the temperature more clearly. Fig 6.8 shows that the microstructure distorted regions and their corresponding domain walls increase with the raise of temperature. It is noted that there is small change in the size of distorted regions between 40ºC and 60Cº, while the variation is higher from 20ºC to 40ºC and between 60ºC to 80ºC. The domain walls start form small size and grow up with temperature.

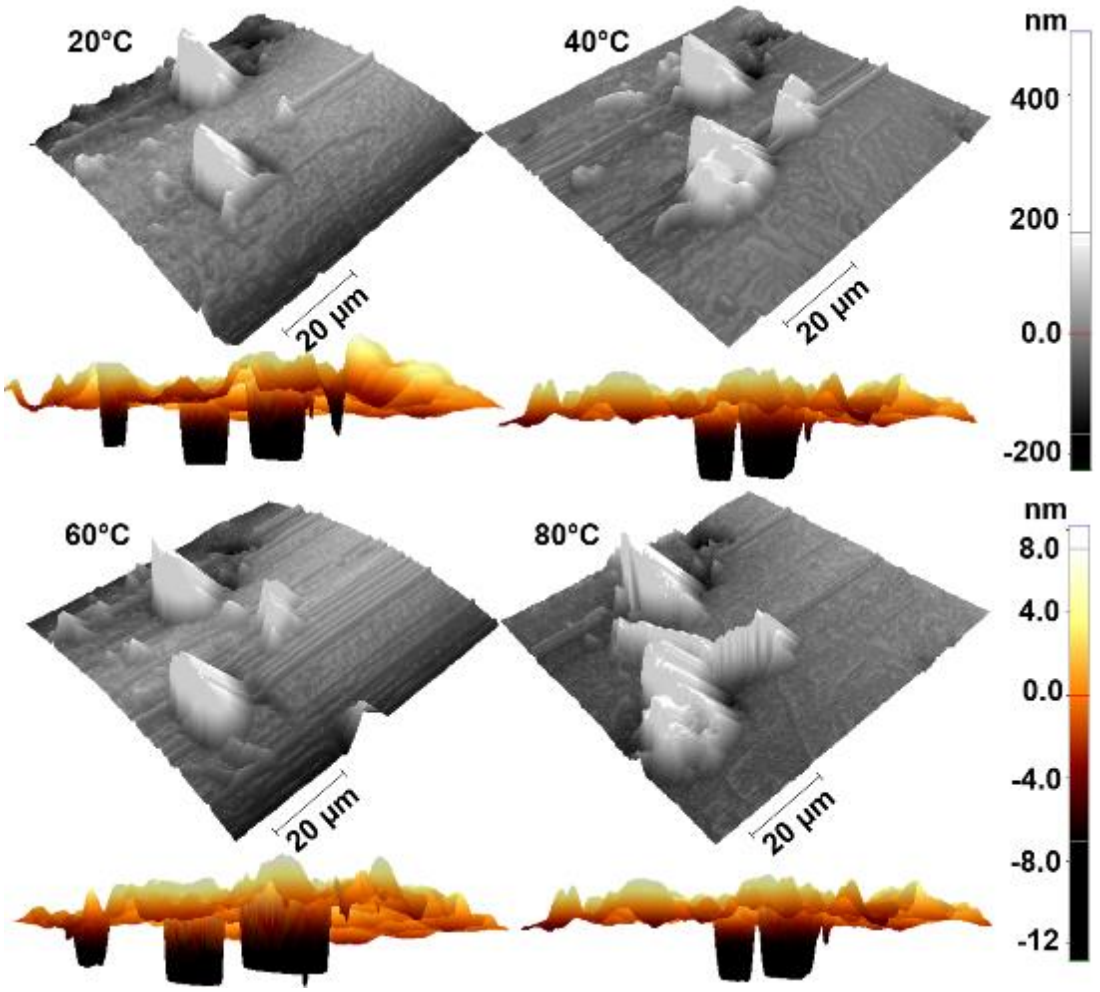

Figure 6-8 In-situ 3D view of surface distortion regions and their corresponding domain walls for sintered Nd-Fe-B magnet observed at different temperature up to 80ºC.

However the observation of in-situ distortion regions of sintered Nd-Fe-B magnets at elevated temperature is presented in 3D view for the first time. In this experiment, the magnetisation of MFM tip and the contrast of MFM images are significantly changed after temperature of 80ºC. Consequently the same location of surface distortion regions cannot be found after 80ºC. Therefore different locations of the same sample surface have been imaged with higher temperature than 80ºC and analysed in the next section.

6.5.2 Observation of distorted regions at elevated temperatures and different locations

The distorted regions of domain walls are observed in the direction perpendicular ($\perp$) to the magnetic alignment axis on the thermally demagnetised state. The observation is made at different locations of the same surface for sintered Nd-Fe-B magnet with

increasing temperature. The temperature is applied up to 120ºC in steps of 20ºC. Fig. 6.9 shows the appearance of distorted domain walls at varies locations of the same sample surface. The size of domain walls are increased as the temperature raise. The temperature degree is shown at the top of each MFM image.

The dark blue areas in Fig. 6.9 represent the effected domain walls and are associated with strong attractive force acting on the tip with negative force gradient, and this indicates a low stray field in their regions.

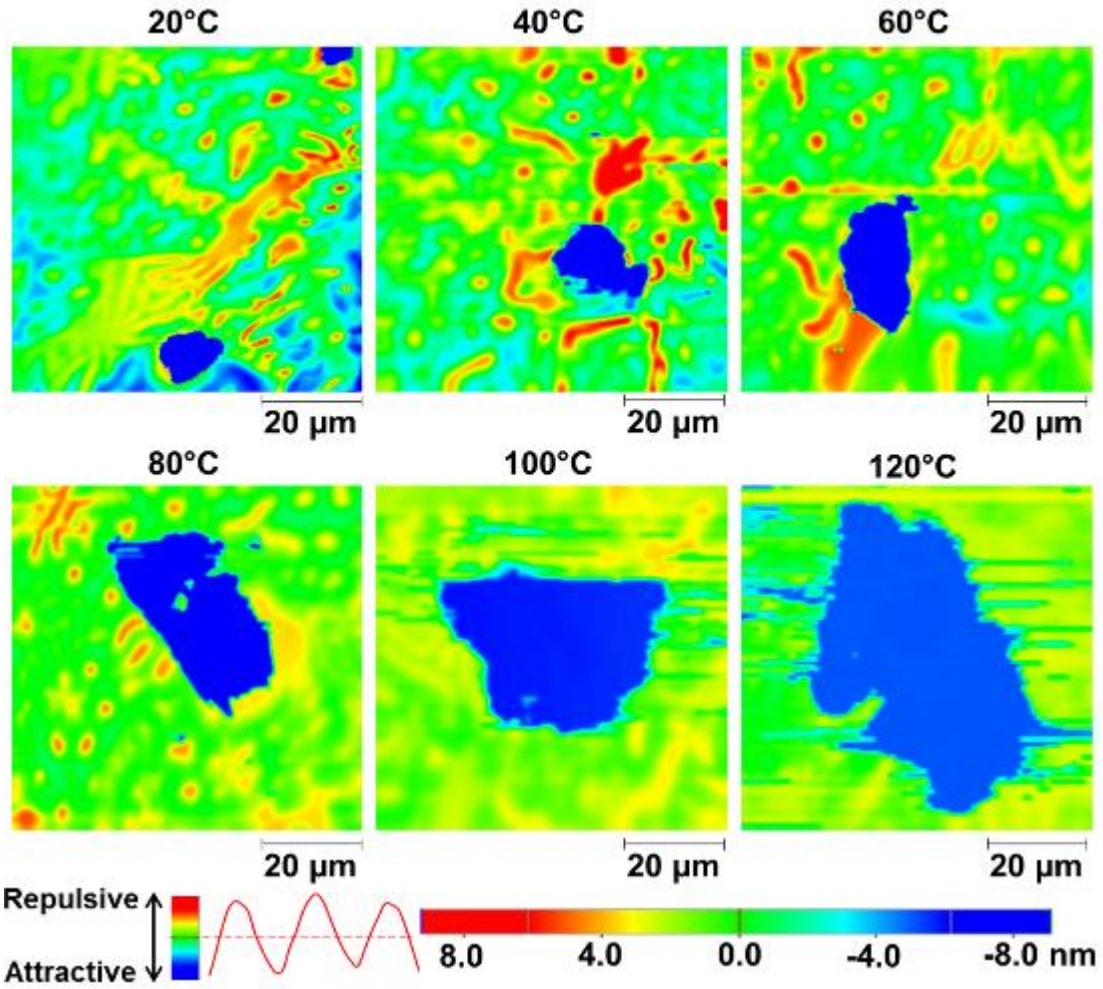

Figure 6-9 Different distorted regions of domain walls at changed temperature up to 120°C for sintered Nd-Fe-B observed at different surface locations using MFM method. The images show an increase of distorted domain walls with temperature.

Ten different locations of the effected domain walls for the proposed sintered Nd-Fe-B magnet are imaged using MFM technique at each degree of temperature and are shown in Appendix C. These different locations of distorted domain wall confirm the increase of distortion regions with temperature. However at the degree of 120°C

the contrast of MFM images is reduced due to the losing of magnetisation of MFM tip, and MFM images cannot be clearly detected after 120°C.

It can be concluded that, the change of temperature increase the size of distorted domain walls at different locations of the same sample surface. However, it is important to study the impact of changing temperature upon the Raman spectra observed in previous section to identify the variation of distorted regions when the temperature is varied.

6.6 In-situ Raman spectroscopy analysis of distorted regions at elevated temperatures

Raman spectroscopy is carried to identify the variation of distorted regions with temperature at the same surface location of sintered Nd-Fe-B magnet. Raman analysis is performed to validate the variation of distortions that observed using MFM technique at high temperature. Fig. 6.10 shows the Raman trace of the sintered Nd-Fe-B magnet at a distorted location and changed temperature up to 120°C. The spectra contain strong peaks appearing in the area between 150-600 cm^{-1} wave number regions, which match the peaks observed for pure Nd_2O_3. The temperature is applied in-situ and in steps of 20°C. The change of Raman peaks is observed as shown in Fig 6.10. The peaks are increased with the raise of temperature. They are increased rapidly from 20°C to 100°C, while the increase is very small between 100°C and 120°C. This is in agreement with the change of distorted domain walls observed using MFM at high temperature, in previous section 6.5. This probably validates our finding of MFM measurements for the increase of distorted regions with temperature.

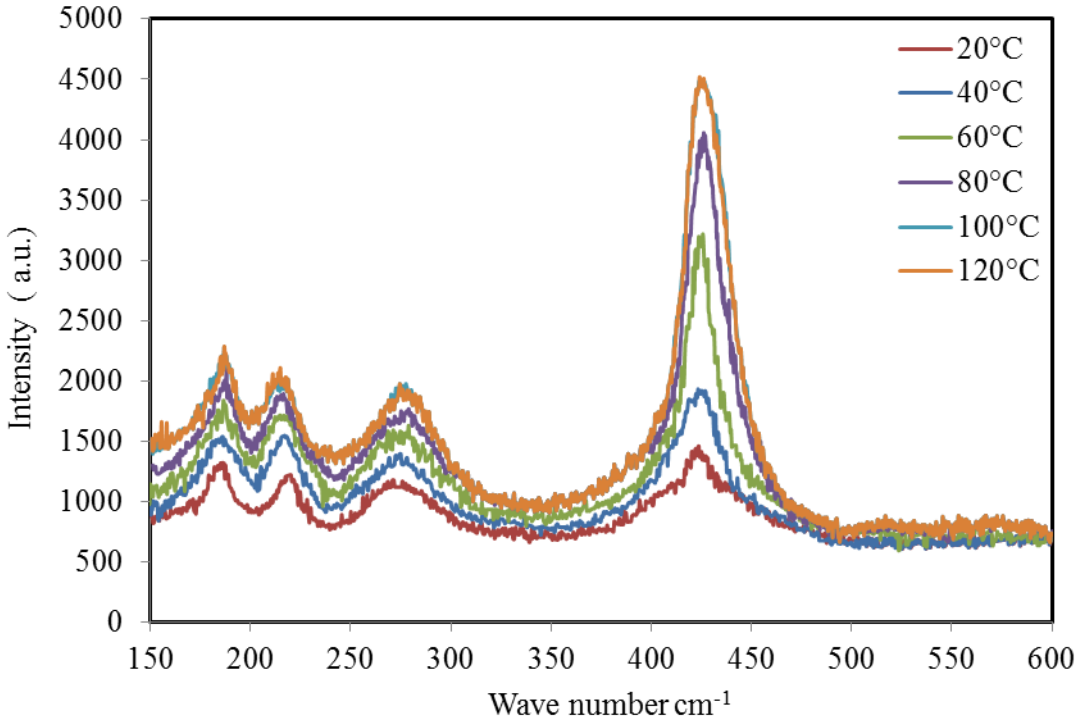

Figure 6-10 in-situ Raman spectroscopy signal for sintered Nd-Fe-B magnet at different temperature up to 120°C. It shows that the peaks are grown with the temperature.

The Raman peaks indicate the variation of crystal structure, which represent the magnetocrystalline structure for the sintered Nd-Fe-B magnet. The magnetocrystalline variation is connected to the anisotropy shape of the magnet. Hence the peaks represent the change of anisotropy shape which is the source of coercivity.

All in all, the Raman spectra are maybe an indicator for the change of anisotropy shape at different temperature, which have an impact on the domain walls. This is useful to estimate the variation on the nanocrystalline anisotropy shape of magnet materials. However some magnet materials are not active with Raman, such as the proposed SmCo magnets.

6.7 Determination of domain wall size at the distorted regions

Domain wall width and domain wall energy are very important microstructural parameters for coercivity analysis. It is claimed in the previous sections that the domain walls is changed with temperature that resulted from the effect of the distortion regions on domain pattern. However it is important to determine the

change of domain wall at the distorted regions. The size and area of distortion sites are determined using two methods, as follows.

6.7.1 Line profile method

A 2D line profile method (cross-section) is used to evaluate the width and height of the distorted sites. The size and area of distortion regions are determined from the width and height. The shape of these regions appears as a circular truncated cone with different lower and upper radii. By using the XEI digital imaging process, the width and height of any features can be easily evaluated using the 2D line profile method (cross-section). 2D line profiles have been applied in both the X and Y axes to determine the shape of distorted regions. Both X and Y line profiles exhibit the same shape, being a circular truncated cone with the same width and height as is shown in Fig. 6.11, and one of the line profiles (X coordinate) is chosen for size determination.

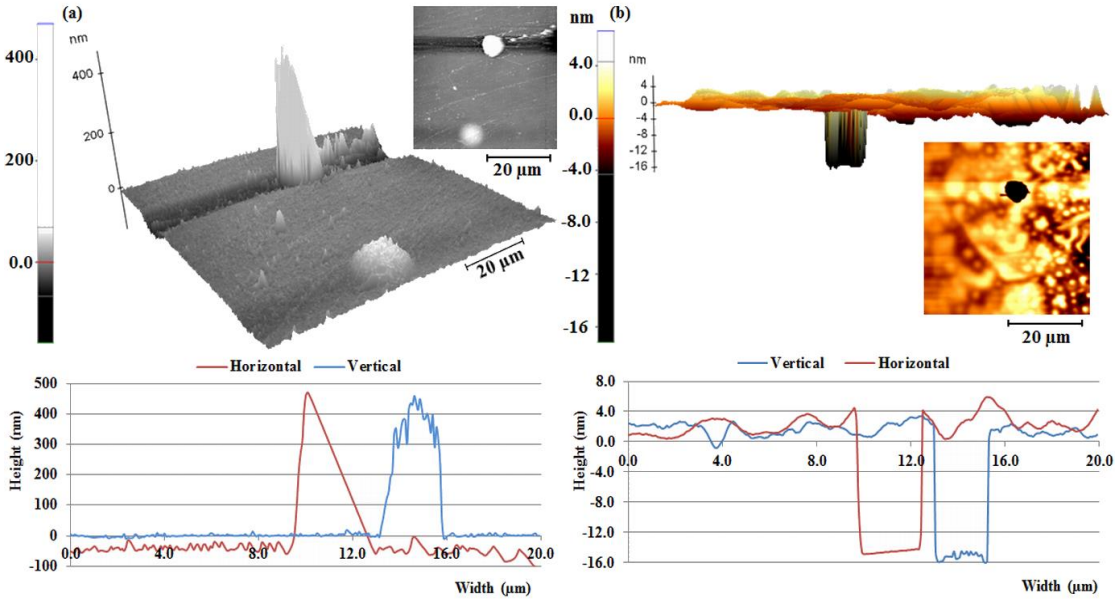

Figure 6-11 Distorted region measured using XEI imaging process software: (a) 2D and 3D topography image and line profile analysis (vertical and horizontal); (b) 2D and 3D MFM image and its line profile analysis (vertical and horizontal).

Half the lower width and half the upper width of the line profile applied over the distorted region represent the lower and upper radii respectively of the truncated cone. The height in the z coordinate of the line profile represents the circular truncated cone height. Then, size and surface area are determined for the truncated cone with different radii from the expressions:

$$v = \frac{1}{3}\prod(r_1^2 + r_1 r_2 + r_2^2)h \tag{5.4}$$

$$s = \prod(r_1 + r_2)\sqrt{(r_1 + r_2)^2 + h^2} \tag{5.5}$$

where: v is the volume of distorted domain wall; s is the surface area; r_1 and r_2 are lower and upper radii respectively; and h is the height. These parameters are determined using 2D line profile analysis on XEI software.

For the sintered Nd-Fe-B sample, six different distorted regions have been scaled using the 2D line profile in XEI imaging software. The heights range from approximately 132 ± 0.2nm to 477 ± 0.1nm and the width is 3 ± 0.2μm. In addition, the six corresponding distorted regions of domain walls are measured with a height of 19 ± 0.2nm, lower radii of 1.33 ± 0.2μm and upper radii from 0.3 ± 0.1μm to 1.02 ± 0.1μm. Hence, the surface area of domain walls ranges from 1.08 to 2.26μm^2 and the volume (v) ranges from 0.0138 to 0.08366μm^3. These values are shown in Fig. 6.12.

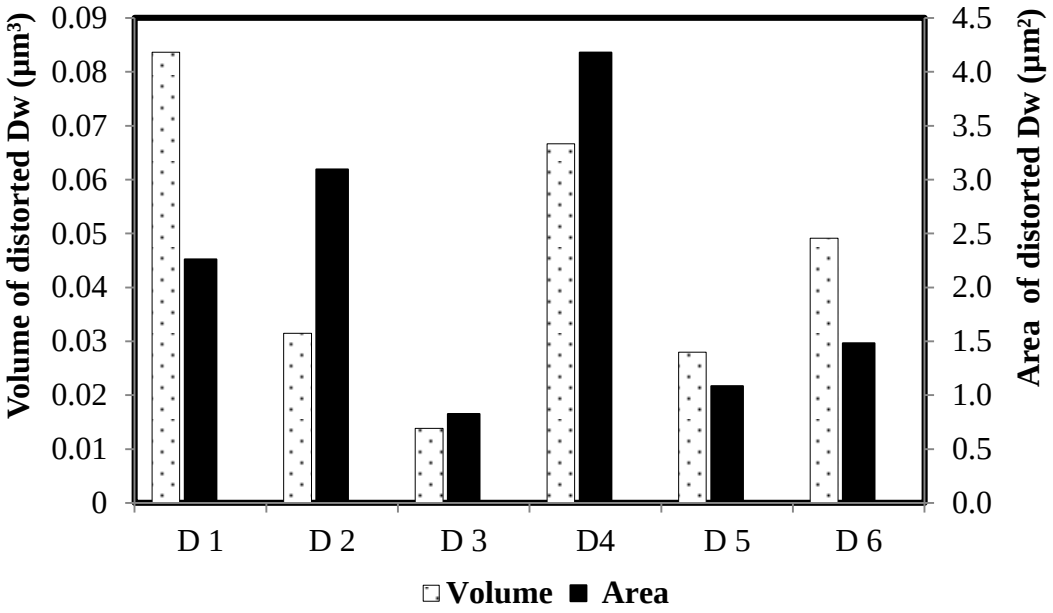

Figure 6-12 Volume and surface area of different distorted regions (D) of domain walls (D_w) measured for sintered Nd-Fe-B magnet using XEI imaging software.

Fig. 6.12 represent the volume and area of distorted sites (D) of domain walls (Dw) at different locations of the same sample surface of sintered Nd-Fe-B magnet. The 2D profile method is proposed for the first time to measure the distorted sites of

MFM images. The applied cross-section line to the distortions determines the shape, from which the volume can be evaluated.

6.7.2 Watershed method

Another proposed method is the watershed technique in XEI software, used to evaluate the volume of distorted regions. The algorithm of the watershed method is explained in detail elsewhere [86]. However, to understand the idea of the watershed algorithm, assume that water is dropped over a surface, as shown in Fig. 6.13. The lowest points of the surface are filled first with water and are recognised first as a single grain. More grains are detected as the water fills more regions. The algorithm identifies the grain boundary and sets the points when the level of water reaches a certain level and overflows from one grain to other neighbouring grains.

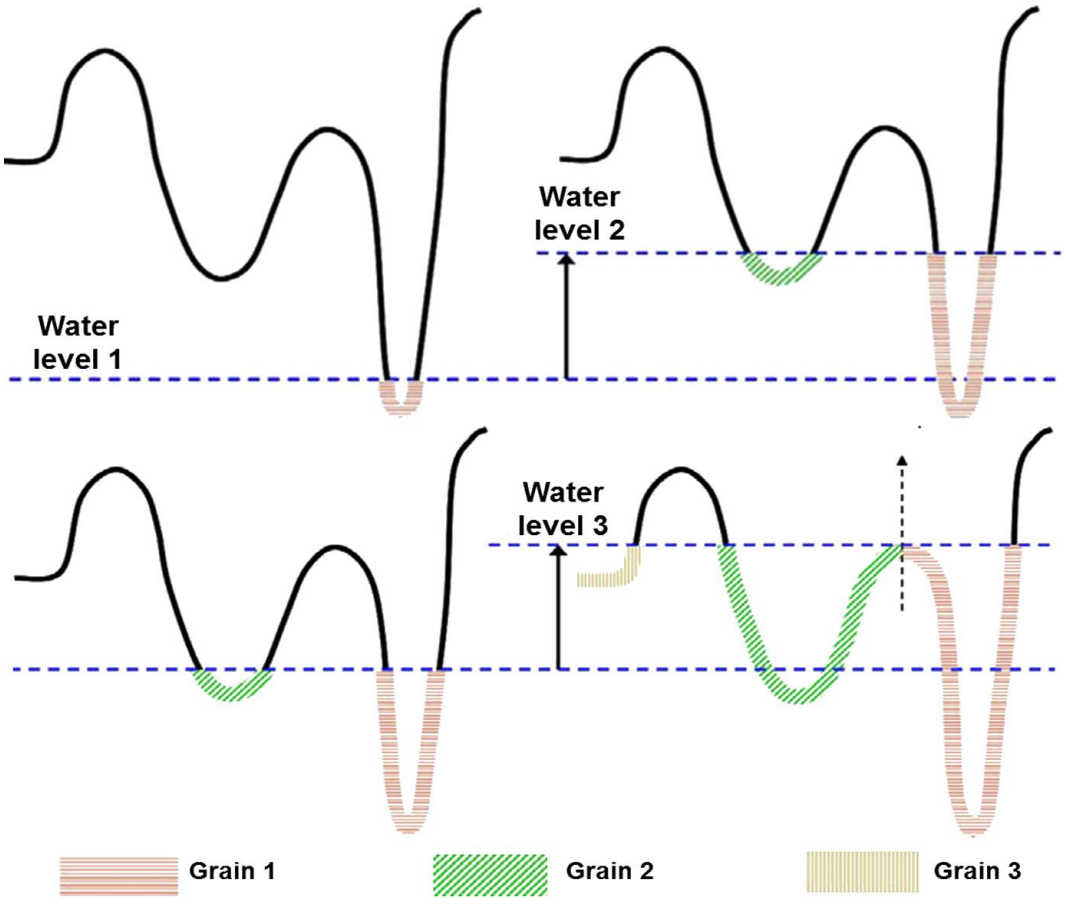

Figure 6-13 Schematic diagram of the process of watershed grain detection.

A number of parameters is detected using the watershed method, such as area, volume, and length of each recognised grain. One of the regions is the distorted site, as shown in Fig. 6.14. For example, the site in Fig. 6.14 is recognised by number 75 and has volume of 0.051µm^3 and area of 4.25µm^2.

Twelve different distorted regions of domain walls for sintered Nd-Fe-B magnet have been scaled using the watershed method, and the volume ranges from approximately 0.023 to 0.097μm^3. The watershed method is more accurate than the 2D line profile method, because the watershed depends mainly on filling the grain with water and detecting the entire region of the grain.

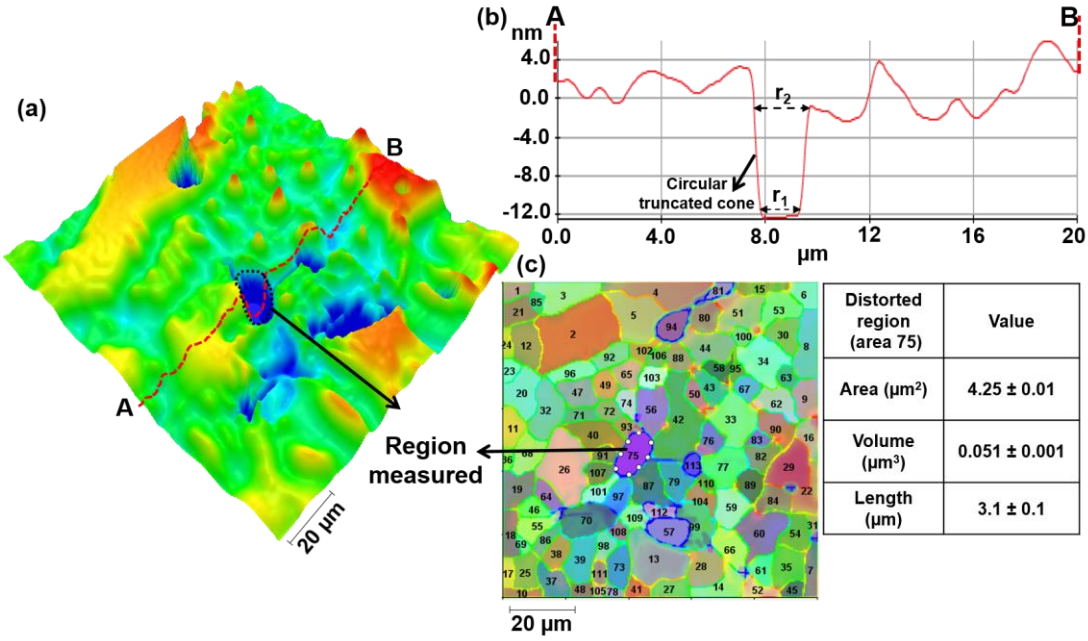

Figure 6-14 Watershed method for determining the size of distorted regions: (a) 3D MFM image with measured region shown in blue; (b) 2D line profile through the region (from A to B) on (a); (c) Grain map of MFM image in (**a).**

Both methods give similar values of size for different distorted regions. Fig. 6.15 shows a comparison in volumes of distorted domain walls between 2D line profile and watershed methods.

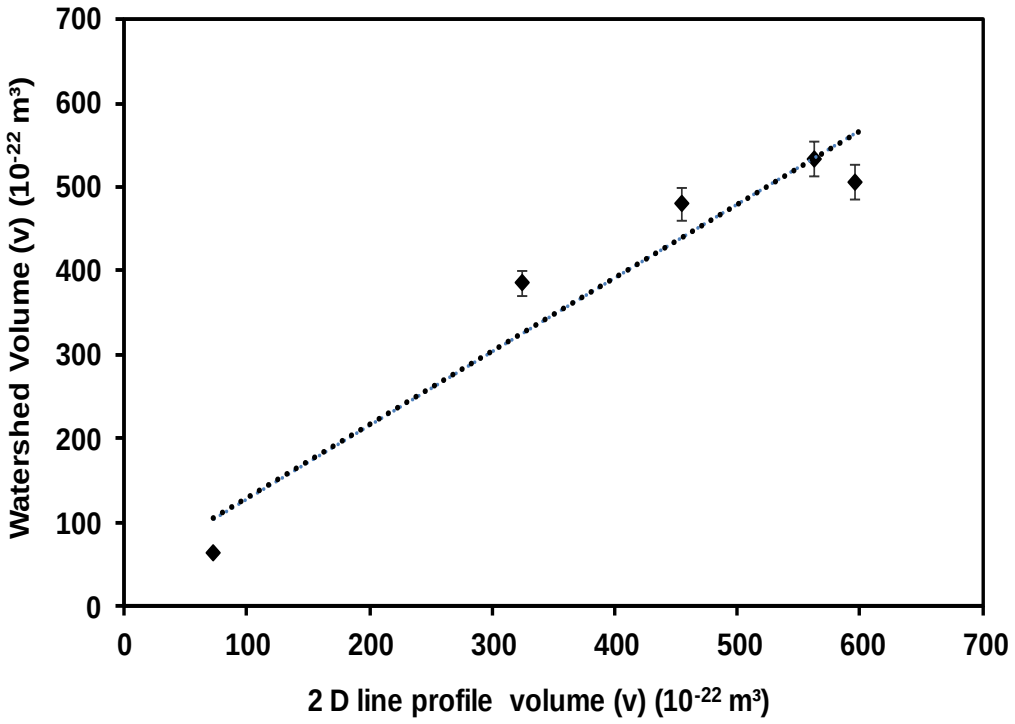

Figure 6-15 Comparison in size of distorted domain walls determined by Watershed and 2D line profile methods.

The change of domain walls at the distorted regions is evaluated when the temperature raise, as explained in next section.

6.8 The Change of domain walls at the distorted regions with temperature

The size of domain walls at the distorted sites estimated using watershed method when the temperature increase. Fig. 6.16 illustrates the watershed method is applied on the distorted domain walls at high temperature for sintered Nd-Fe-B magnet to determine the size.

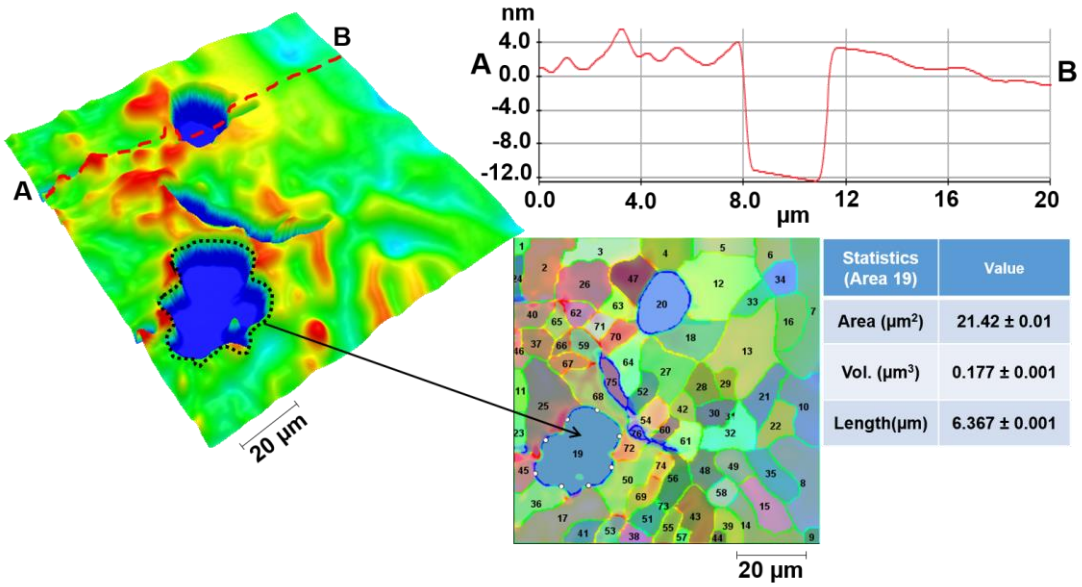

Figure 6-16 Watershed method is used to determine the size of distorted domain walls at high temperature.

Ten distorted regions are scaled at each degree of temperature from 20°C to 120°C in steps of 20°C. The average size of ten regions at each degree of temperature is evaluated. The size of domain walls ranges from 0.048 to 0.69 μm^3, depending on the temperature degree. The values of volume are presented in appendix D. Fig 6.17 shows the relationship between the temperature and size of distorted regions for sintered Nd-Fe-B magnet. It illustrates that the volume of domain walls at distorted regions is increased as the temperature raise. It is noted that the size is increased rapidly from 20°C to 100°C, while between 100°C and 120°C, the increase is very small. This is probably because of the rapid weakening of the magnetocrystalline anisotropy at higher temperature.

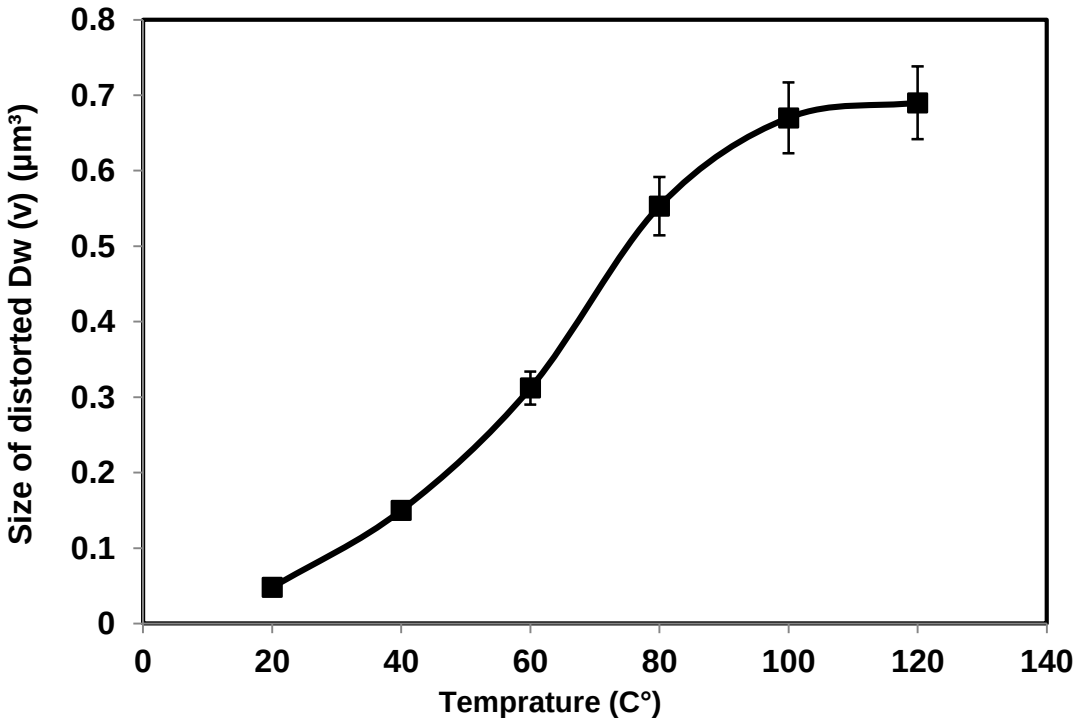

Figure 6-17 Size of distorted domain wall varies temperature of sintered Nd-Fe-B magnet. The size is calculated using watershed method.

6.9 Summary

The microstructure analysis of the proposed sintered Nd-Fe-B magnet has been presented in this chapter. The crystal microstructure consists of mainly a hard magnetic $Nd_2Fe_{14}B$ matrix and Nd-rich phases at grain boundary and triple junction. This chapter has described the observation of some distorted regions on the surface of sintered Nd-Fe-B magnet using MFM technique. The distortion regions have great impact on the domain walls. The effect of these distorted regions on the domain walls was studied for the first time using MFM technique. These regions have been identified using Raman spectroscopy as Nd-rich sites. The Raman spectra illustrates that the distortion regions are oxides rather than metallic in character and identified as Nd_2O_3.

In addition, this chapter has described the observation of distorted regions at elevated temperature up to 120°C in steps of 20°C, using MFM technique. The observation has been made in-situ and at different locations of sample surface. Raman spectroscopy has been also carried to identify the variation of distorted regions with temperature up to 120°C, at the same surface location of sintered Nd-Fe-B magnet.

The Raman data validates the finding of MFM measurements for the increase of distorted regions with temperature.

Furthermore, the physical characteristics of distorted sites have been determined from the MFM images. The size of distorted domain walls were determined for the first time using the 2D line profile and the watershed technique. Ten distorted regions were scaled at each temperature degree using the watershed method, and the average volumes were determined. The results show that the volume is increased with the raise of temperature up 120°C. The distorted sites grow rapidly at low temperature in contrast to high temperature.

These insights will help to understand the effect of the distorted regions on domain walls and energy that may lead to deep knowledge of domain microstructure of sintered Nd-Fe-B magnets.

CHAPTER 7 CONCLUSIONS AND FUTURE WORK

7.1 Background

Rare earth magnet materials have been the preferred choice of materials in many applications. The high demand and expected supply shortages, however have led to a significant increase in the prices of rare earth magnet materials. Therefore, the issues associated with today's rare earth supply need to be addressed in more depth. In this context, more research is being conducted to develop of free rare earth magnets that combine high coercivity and high thermal resistance. Therefore, it is essential to understand the microstructural analysis of materials in greater detail.

More attention in the review of this thesis was focused on the field of permanent magnet materials, in terms of magnetic properties; microstructural analysis; the magnetisation process; and commercially available types of PM materials. The crystal and domain structure of sintered Nd-Fe-B magnets have been described in detail. The crystal structure of sintered Nd-Fe-B magnets comprises mainly of a hard magnetic $Nd_2Fe_{14}B$ matrix surrounded by Nd-rich phase. The Nd-rich phases appear in thin and large layers between the grains and at triple junctions, respectively. However the effect of Nd-oxides at triple junctions on magnetic domains is rarely studied comparing to the thin layers.

Previous research has shown that studying the segregation of the magnetic domains at grain boundaries is an important concern for developing high coercivity magnets. The Nd-rich phases between grain boundaries and at triple junctions play a crucial role in the coercivity mechanism. The Nd-rich phases have a great impact on the domain wall movement. It is vital to understand the effect of Nd-rich phases on the domain wall and the change of magnetic anisotropy that lead to the possibility of improving coercivity.

Therefore, it is suggested here that magnetic force microscopy (MFM) should be used to study the structure of grain separation of sintered permanent materials and to correlate it with domain wall, since; the MFM has a high resolution.

7.2 Magnetic domain analysis

The use of the MFM technique has been described to characterise the domain microstructure of sintered Nd-Fe-B and SmCo magnets. Observations are made at surfaces perpendicular and parallel to the alignment axis. Maze-like magnetic domains and stripe magnetic domains are observed in the perpendicular and parallel surfaces respectively. MFM images illustrate the grains of Nd-Fe-B magnets, and indicate the multi-domain structures within individual grains. Branch-like domains are observed for sintered Nd-Fe-B and Sm_2Co_{17} magnets in the parallel alignment axis. The domain structures have been analysed for the first time in the 3D view. The 3D MFM images exhibited that a different microstructure is present for each of the samples. In addition the MFM images have shown important micro-magnetic structural characteristics such as spike domains and reverse spikes in the 3D view. The appearance of spikes domains and reverse spikes indicate the stray magnetic field acting on the MFM tip from the underlying magnetic domains. The spike domains and reverse spikes reduce the domain wall energy, generate a strong surface anisotropy, and may reduce the density of magnetostatic energy near the surface. These domain patterns may affect the magnetocrystalline anisotropy, which is the source of coercivity, leading to have an impact on coercivity. Therefore, the observation of spike domains and reverse spikes is an important step in order to control their appearance over the surface.

7.3 Determination of microstructure parameters

Some microstructural parameters, such as domain width and domain wall energy, for sintered Nd-Fe-B and SmCo magnets are determined from MFM images. The domain wall energy calculated from the measurement of domain width. The stereological method was used to determine the domain width modelled in Matlab. The effective domain width and domain wall energy have been determined in surfaces both perpendicular and parallel to the alignment axis. The sintered Nd-Fe-B magnet exhibited fine domain structures in both directions, with values of $0.78 \pm 0.01\mu m$ and $1 \pm 0.1\mu m$ in directions perpendicular and parallel to the alignment axis respectively. The SmCo magnets have a domain width varies in the range of 0.3 – 2.1μm in the perpendicular direction and 0.89 - 3.5μm in the parallel direction.

On the whole, a surface parallel to the alignment axis exhibits a higher domain width and energy compared to that in the perpendicular direction. The results showed that just changing the annealing temperature can have a major effect on the domain width and domain wall energy that leads to change the magnetic properties.
In addition, the variation of magnetic properties for the proposed magnets has been evaluated using MFM phase images. It has been found that the ratio of root-mean-square values for MFM phase images ($Ø^{\perp}/Ø^{//}$) is a good indicator of magnet properties.

7.4 Effect of grain separation on domain patterns of sintered Nd-Fe-B magnets

The crystal microstructure of the proposed sintered Nd-Fe-B magnet consists of mainly a hard magnetic $Nd_2Fe_{14}B$ matrix and Nd-rich phases at grain boundary and triple junction. Some distorted regions on the surface of sintered Nd-Fe-B magnet were observed using MFM technique. The distorted regions have great impact on the domain walls. The effect of these distorted regions on the domain walls was studied for the first time using MFM technique. These regions have been identified using Raman spectroscopy as Nd-rich sites. The Raman spectra illustrates that the distortion regions are oxides rather than metallic in character and identified as Nd_2O_3.

In addition, the distorted regions were observed at elevated temperature up to 120°C in steps of 20°C, using MFM technique. The observation has been made in-situ and at different locations of sample surface. Raman spectroscopy has also been carried to identify the variation of distorted regions with temperature up to 120°C, at the same surface location of sintered Nd-Fe-B magnet. The Raman data validates the finding of MFM measurements for the increase of distorted regions with temperature.

The physical characteristics of distorted sites were determined from the MFM images. The size of distorted domain walls were calculated using the 2D line profile and the watershed technique. Ten distorted regions have been scaled at each temperature degree using the watershed method, and the average volumes were determined. The results show that the volume is increased with the raise of temperature up 120°C. The distorted sites grow rapidly at low temperature in contrast to high temperature.

These insights will help to understand the effect of the distorted regions on domain walls and energy that may lead to deep knowledge of domain microstructure of sintered Nd-Fe-B magnets.

7.5 Future work and recommendations

The conclusion of this work has been the successful observation, study, determination and analysis of magnetic domain microstructure for sintered Nd-Fe-B and SmCo magnet materials using MFM in order to understand the coercivity mechanism. Whilst the micromagnetic domains are observed and the microstructure parameters are calculated, the implementation of these parameters to understand the coercivity mechanism is limited.

The research described in this thesis is one step of understanding the magnetic domains. The following recommendations for future work;

- Improve the capability of MFM technique to observe the distorted regions at an external field applied during the process of scanning.
- Possibility of observing the movement of domains during the interaction with distorted site.
- Using MFM cantilever with high magnetic coercivity tips (more than the standard), in order to observe the microstructure domains at temperature degree higher than 120ºC.
- Analyse the MFM images by appropriate micromagnetic simulation software such as OOMMF software to understand the distorted regions in more detail.
- Study the correlation between the distorted regions and the crystal structure of rare earth magnet materials.
- The possibility of understanding the correlation between the coercivity and magnetic domain structure.

APPENDIXES

Appendix A

Model code for determination of main domain width and domain wall energy

The following codes are used to determine the main domain width and domain wall energy from the MFM images. Firstly the MFM images are transferred to black and white images to be readable with Matlab. Secondly the images are uploaded and the next codes are applied.

```
Function AA
Close all
Clear all
clc
DIS=20;
A=imread('140522MFM Amplitude001 copy1.tiff');
M=size(A)
DM=M(1);
imshow(A)
Figure
df=DIS/M(1);
n=100;
AB1=zeros(M(1),M(2),3);
AB1(:,:,1)=A;
AB1(:,:,2)=A;
AB1(:,:,3)=A;
AB1=AB1/255;
i=1;
While (i<=n)
    i
    AB=A;
    P1=rand(1,2)*M(1);
    P2=rand(1,2)*M(1);
    [AB1,N(i),L(i)]=LINE(AB1,AB,P1,P2);
    if(N(i)==0)
       i=i-1;
    end
    i=i+1;
end
imshow(AB1)
N;
L;
LL=sum(L)*df
NN=sum(N)
DW=(2/pi)*(LL/NN)
DW1= DW*10^-4
mu0=4*pi*10^-7
beta=0.31
Ms=(1.44/mu0)*10^-3
```

```
Yw=((DW1)*(Ms)^2)/(4*pi*beta)
end
```

Applying different lines over the image

```
Function [AB,N,L]=LINE(AB,A,P1,P2)
N=0;
M=size(A);
st=0;
fl=0;
EL=[1,1];
SL=[1,1];
dx=P1(1)-P2(1);
dy=P1(2)-P2(2);
For i=1:1:M(1)
    if(abs(dx)>abs(dy))
        a=dy/dx;
    x=round(i);
    y=round((a*(i-P2(1))+P2(2)));
    else
          a=dx/dy;
    y=round(i);
    x=round((a*(i-P2(2))+P2(1)));
    end

    if(y<=0 || y>M(2) || x<=0 || x>M(1))
        continue;
    end
   if(fl==0)
     fl=1;
     SL=[x y];
      if(A(x,y)>100)
      st=1;
      end
   end
    EL=[x,y];
    if(A(x,y)>200 && st==0)
     st=1;
     N=N+1;
    end
   if(A(x,y)<100 && st==1)
     st=0;
     N=N+1;
   end
   AB(x,y)=0;
end
L=sqrt(sum((SL-EL).^2));
end
```

Appendix B

Surface distorted areas during scanning process

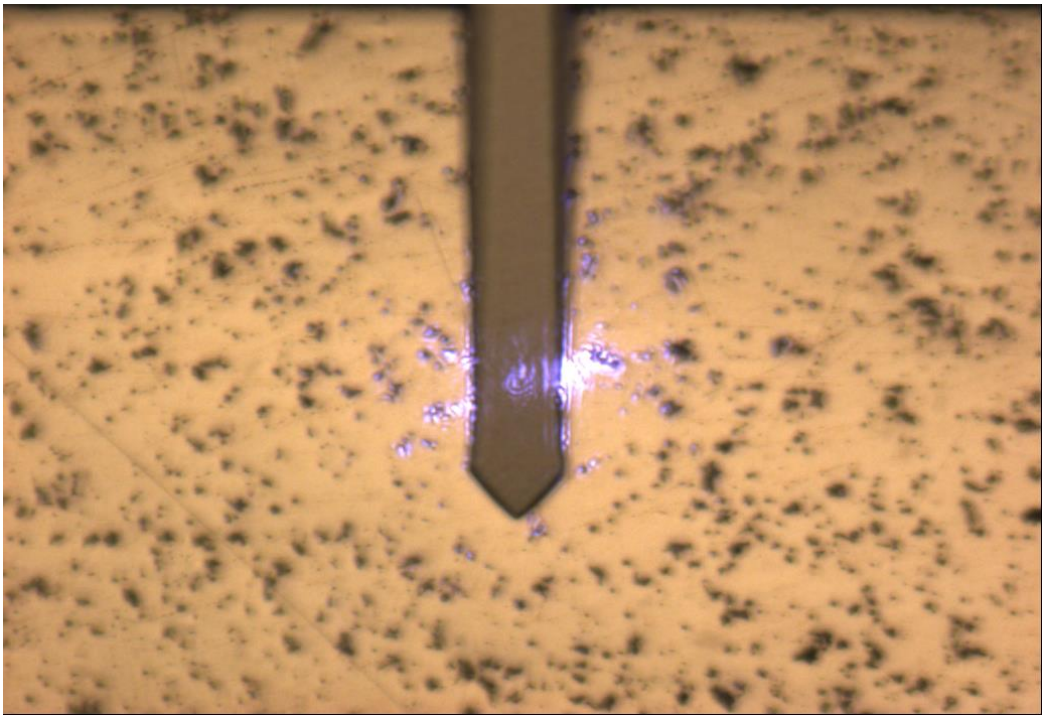

Location of one distorted regions at the surface of Nd-Fe-B magnet during scanning process

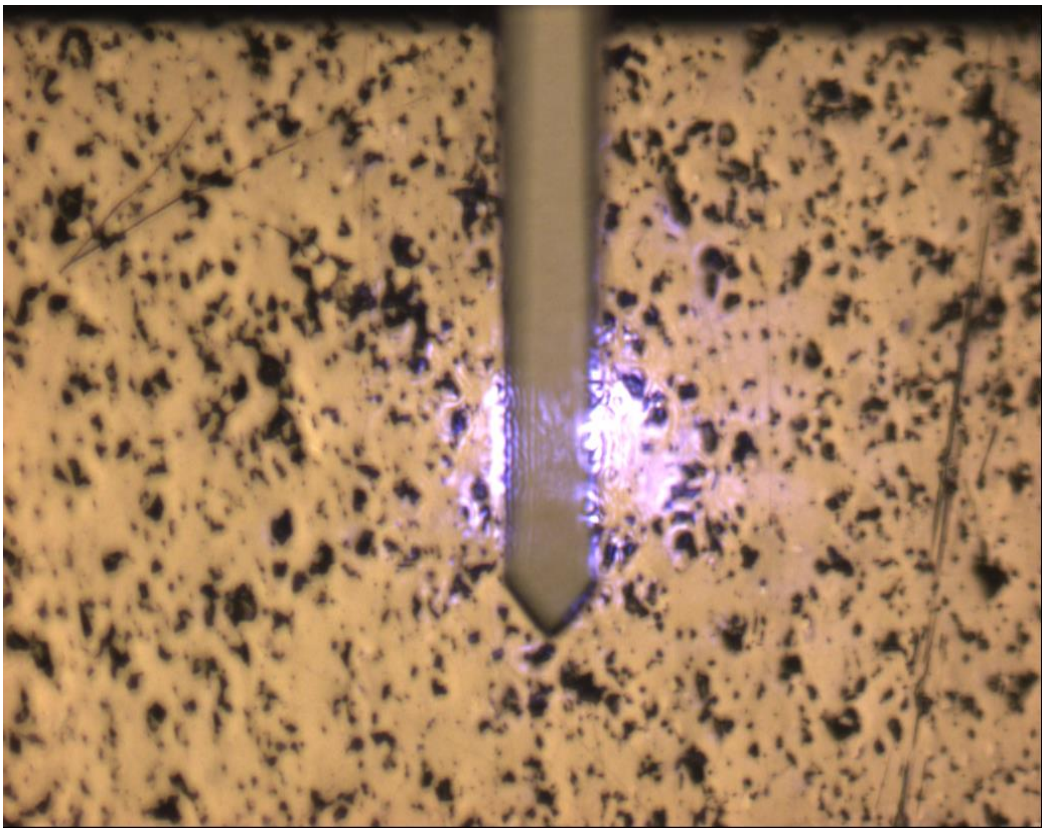

Domain structure of sintered Nd-Fe-B magnet on the perpendicular surface

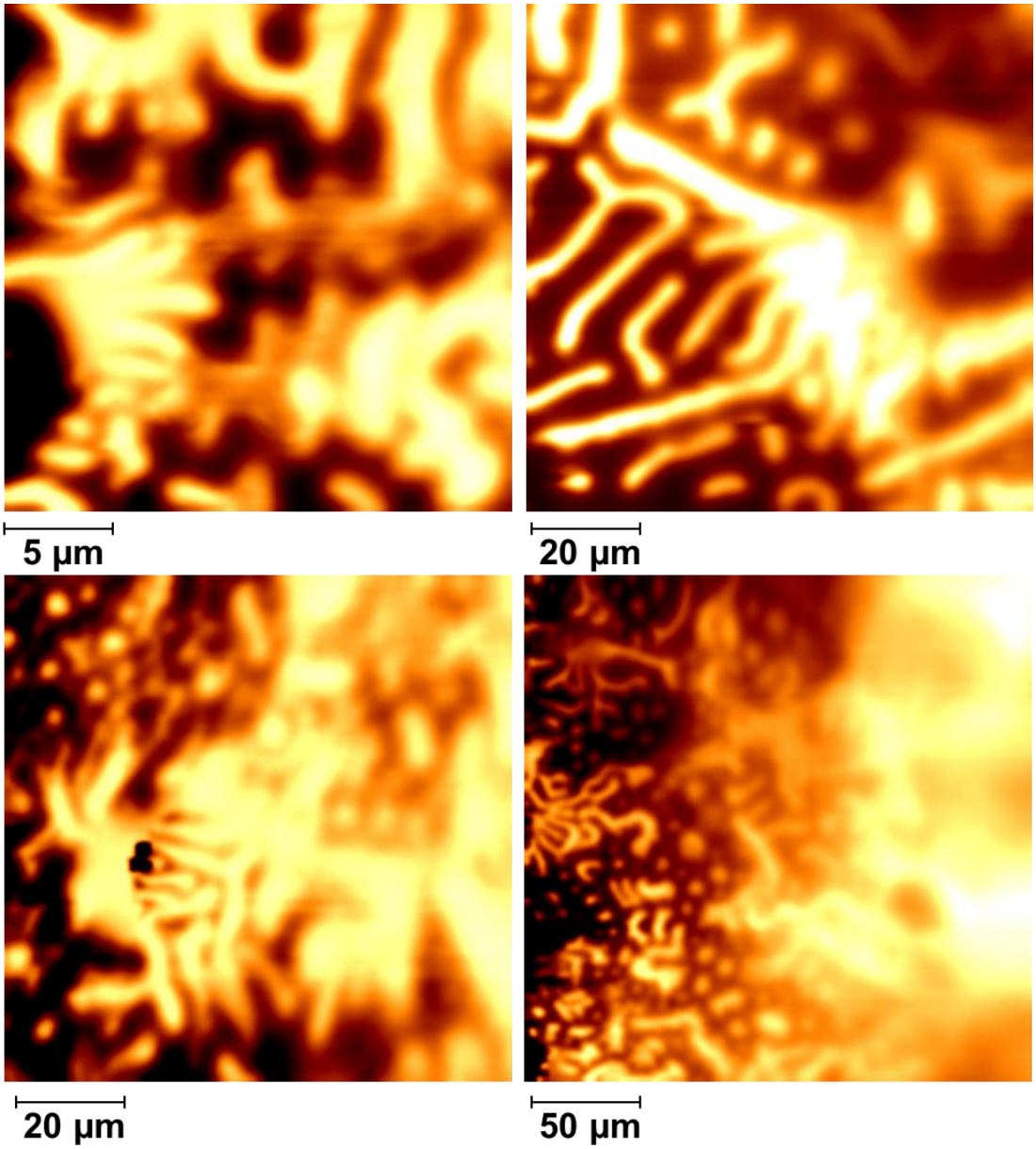

Domain structure of sintered Nd-Fe-B magnet observed using MFM on the surface perpendicular to the alignment axis at different locations and varies scan size.

Domain structure of sintered Nd-Fe-B magnet on the parallel surface

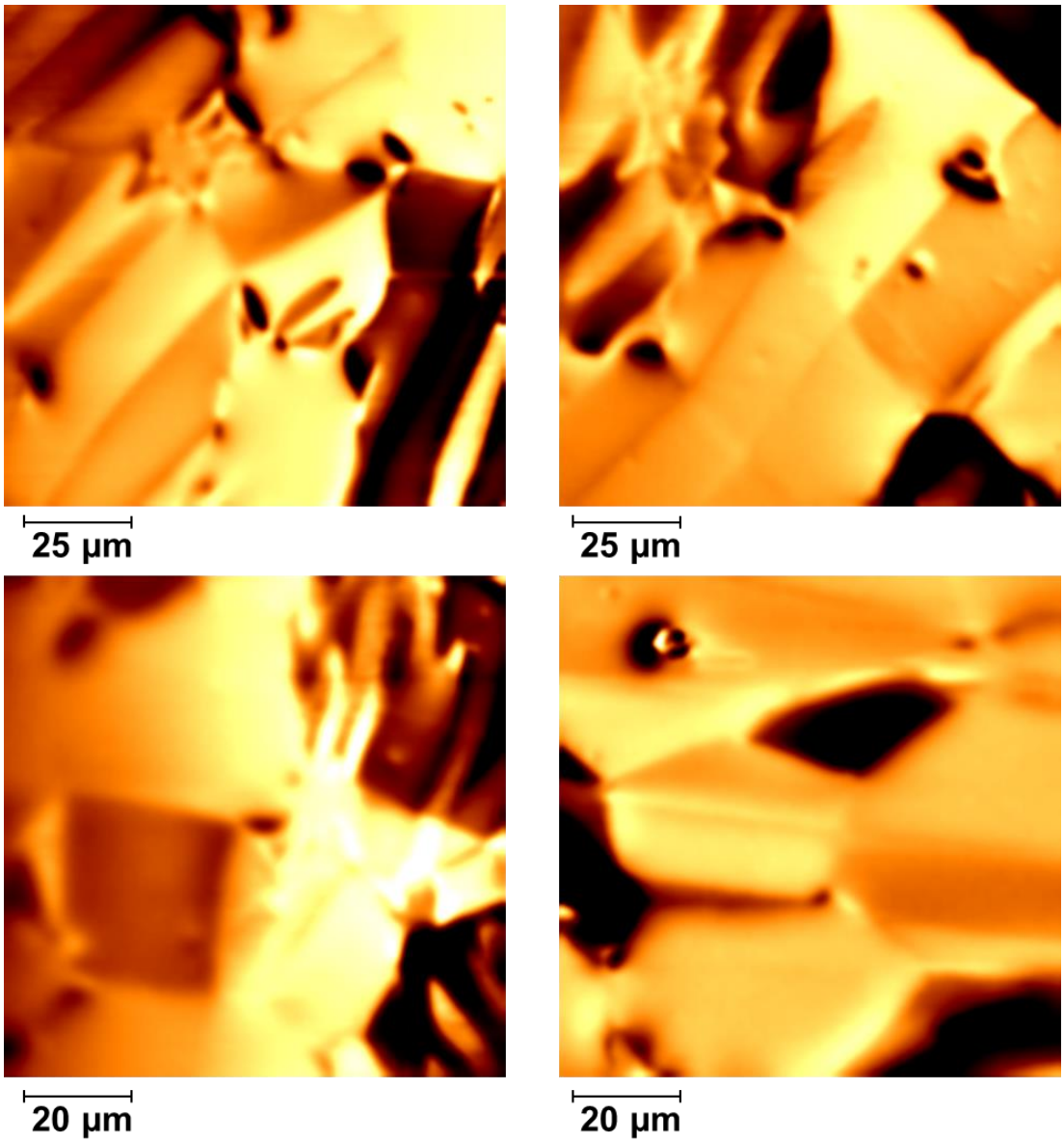

Domain structure of sintered Nd-Fe-B magnet observed using MFM on the surface parallel to the alignment axis at different locations and varies scan size.

Domain structure of sintered SmCo magnets on the perpendicular and parallel surface

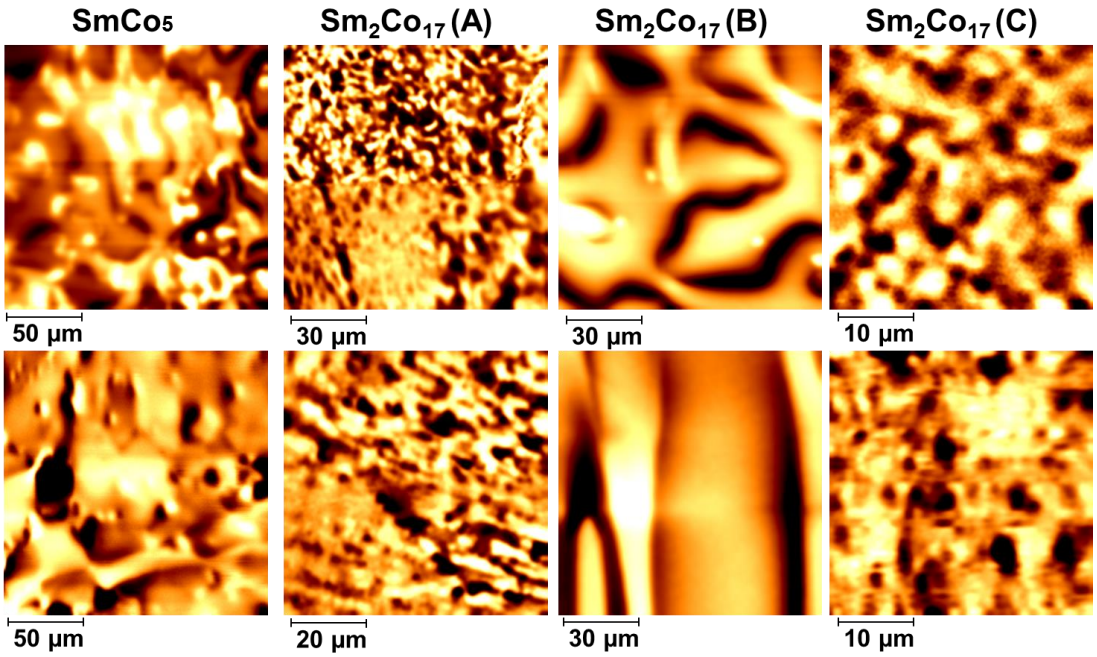

Domain structure of sintered Nd-Fe-B magnet observed using MFM on the surface perpendicular (upper row) and parallel (lower row) to the alignment axis at different locations and varies scan size

Appendix C

Observation of distorted regions at elevated temperatures and different locations

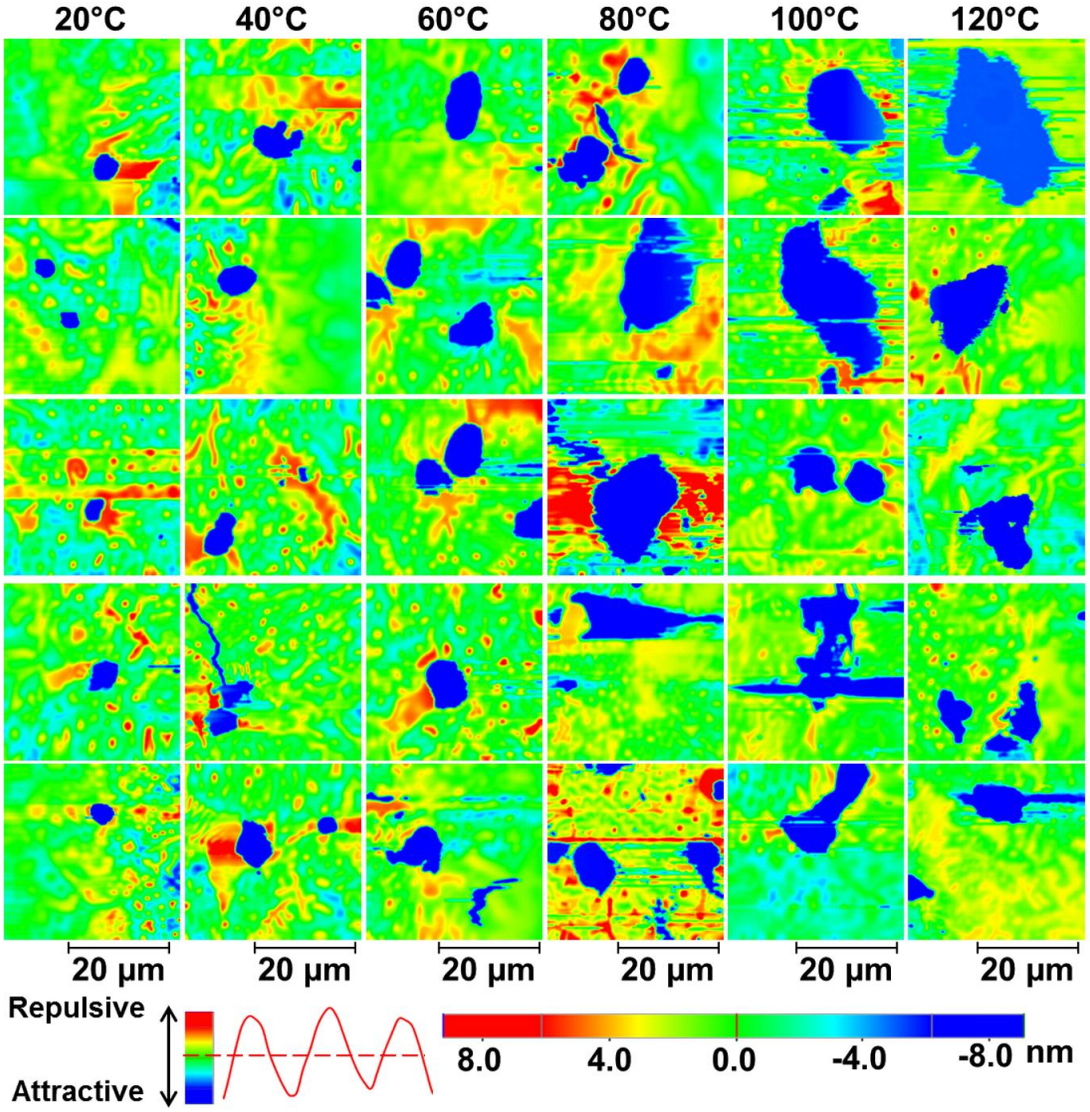

Continuing

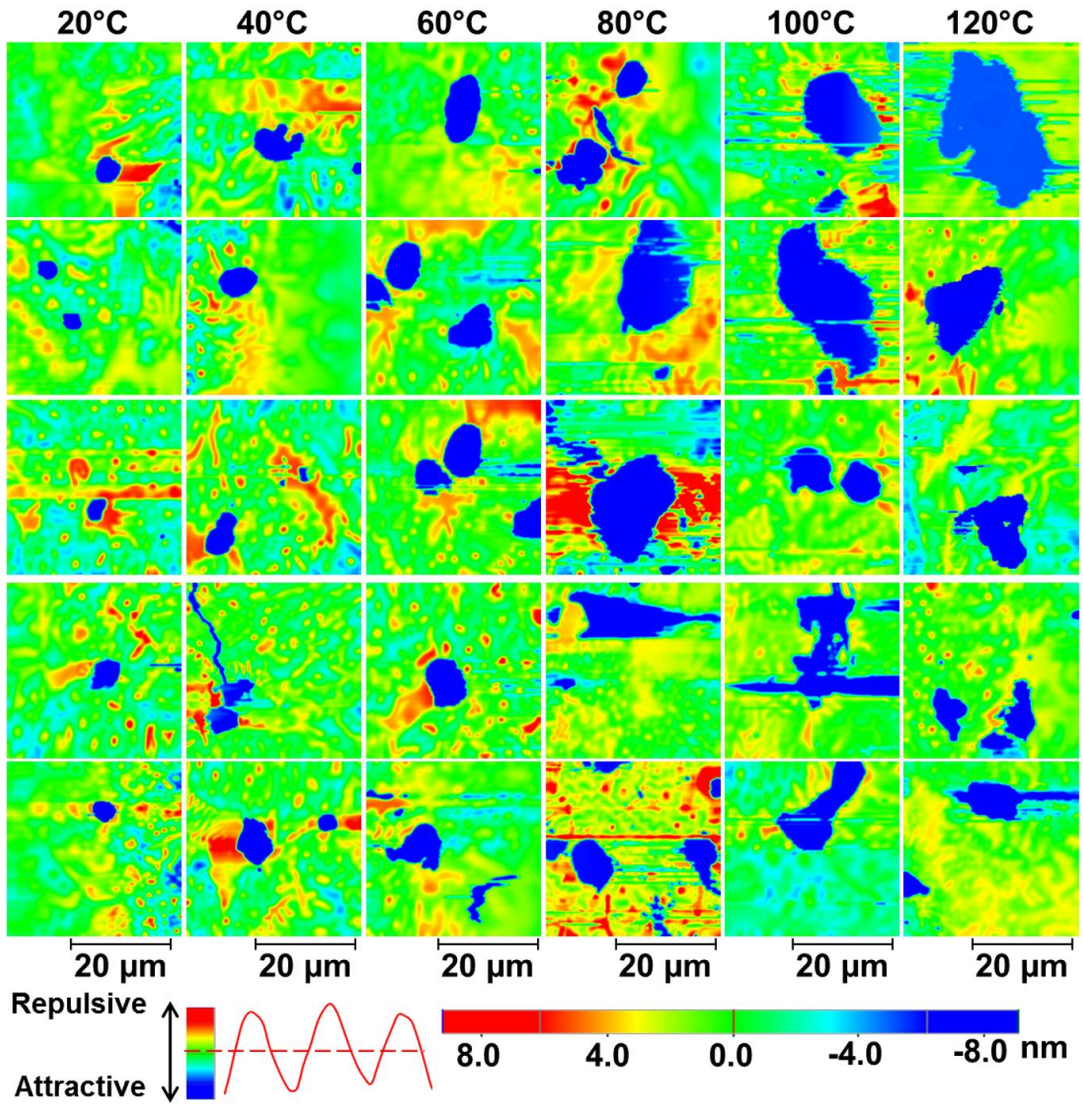

Different distorted domain walls at changed temperature up to 120°C for sintered Nd-Fe-B observed at different surface locations using MFM method**.**

The average volume of ten distorted domain walls at each degree of temperature

[a]T (°C)	[a]v_1	v_2	v_3	v_4	v_5	v_6	v_7	v_8	v_9	v_{10}	Avg. v
20	0.077	0.036	0.067	0.056	0.035	0.055	0.049	0.096	0.041	0.031	0.048
40	0.142	0.110	0.154	0.151	0.133	0.129	0.181	0.149	0.130	0.175	0.148
60	0.256	0.230	0.326	0.174	0.203	0.385	0.367	0.376	0.419	0.494	0.312
80	0.61	1.122	0.769	0.764	0.604	0.618	0.401	0.554	0.339	0.153	0.553
100	0.99	0.78	0.512	0.477	0.626	0.965	0.535	0.525	0.777	0.398	0.659
120	0.453	0.697	0.470	1.723	0.413	0.68	0.491	0.580	0.37	0.279	0.688

[a] v= Volume of distorted domain walls (μm^3); Avg. *v*= the average of ten volumes; and T= temperature (°C).

REFERENCES

[1] O. Gutfleisch, M. A. Willard, E. Brück, C. H. Chen, S. G. Sankar, and J. P. Liu, "Magnetic Materials and Devices for the 21st Century: Stronger, Lighter, and More Energy Efficient," *Advanced Materials,* vol. 23, pp. 821-842, 2011.

[2] T. G. Woodcock, Y. Zhang, G. Hrkac, G. Ciuta, N. M. Dempsey, T. Schrefl, *et al.*, "Understanding the microstructure and coercivity of high performance NdFeB-based magnets," *Scripta Materialia,* vol. 67, pp. 536-541, 9// 2012.

[3] L. H. Lewis and F. Jiménez-Villacorta, "Perspectives on Permanent Magnetic Materials for Energy Conversion and Power Generation," *Metallurgical and Materials Transactions A,* vol. 44, pp. 2-20, 2013.

[4] O. Gutfleisch, K. H. Müller, K. Khlopkov, M. Wolf, A. Yan, R. Schäfer, *et al.*, "Evolution of magnetic domain structures and coercivity in high-performance SmCo 2:17-type permanent magnets," *Acta Materialia,* vol. 54, pp. 997-1008, 2// 2006.

[5] H. Sepehri-Amin, T. Ohkubo, and K. Hono, "Grain boundary structure and chemistry of Dy-diffusion processed Nd--Fe--B sintered magnets," *Journal of Applied Physics,* vol. 107, pp. 09A745-3, 05/01/ 2010.

[6] H. Nakamura, K. Hirota, T. Ohashi, and T. Minowa, "Coercivity distributions in Nd–Fe–B sintered magnets produced by the grain boundary diffusion process," *Journal of Physics D: Applied Physics,* vol. 44, p. 064003, 2011.

[7] R. Goto, M. Matsuura, S. Sugimoto, N. Tezuka, Y. Une, and M. Sagawa, "Microstructure evaluation for Dy-free Nd-Fe-B sintered magnets with high coercivity," *Journal of Applied Physics,* vol. 111, pp. 07A739-3, 04/01/ 2012.

[8] D. Hinz, J. Lyubina, G. Fuchs, D. N. Brown, B. M. Ma, O. Gutfleisch, *et al.*, "Hot deformed (Nd,Pr)(Fe,Co)B magnets for low-temperature applications," *Journal of Magnetism and Magnetic Materials,* vol. 272–276, Supplement, pp. E321-E322, 5// 2004.

[9] M. Takezawa, H. Ogimoto, Y. Kimura, and Y. Morimoto, "Analysis of the demagnetization process of Nd–Fe–B sintered magnets at elevated temperatures by magnetic domain observation using a Kerr microscope," *Journal of Applied Physics,* vol. 115, p. 17A733, 2014.

[10] K. J. Strnat, "Modern permanent magnets for applications in electro-technology," *Proceedings of the IEEE,* vol. 78, pp. 923-946, // 1990.

[11] T. Mishima, "Nickel aluminum steel for permanent magnets," *Ohm,* vol. vol. 19, p. pp.353, 1932

[12] B. D. Cullity and C. D. Graham. (2009). *Introduction to Magnetic Materials*.

[13] G. W. R. J. J. Went , E. W. Gorter and G. W. Van Oosterhout, "Ferroxdure, a class of new permanent magnets," *Philips Tech. Rev,* vol. 13, pp. 194 -208 1952

[14] K. Strnat, G. Hoffer, J. Olson, W. Ostertag, and J. J. Becker, "A Family of New Cobalt-Base Permanent Magnet Materials," *Journal of Applied Physics,* vol. 38, pp. 1001-1002, 03/01/ 1967.

[15] K. Strnat, "The recent development of permanent magnet materials containing rare earth metals," *Magnetics, IEEE Transactions on,* vol. 6, pp. 182-190, 1970.

[16] A. E. Ray and S. Liu, "Recent progress in 2:17-type permanent magnets," *Journal of Materials Engineering and Performance,* vol. 1, pp. 183-191, 1992/03/01 1992.

[17] K. H. J. Buschow, "Magnetism and Processing of Permenant Magnet Materials
" in *Handbook of Magnetic Materials*. vol. 10, ed Elsevier Science B.V., Atlanta GA., 1997, pp. 463-593.
[18] M. Sagawa, S. Fujimura, N. Togawa, H. Yamamoto, and Y. Matsuura, "New material for permanent magnets on a base of Nd and Fe (invited)," *Journal of Applied Physics,* vol. 55, pp. 2083-2087, 03/15/ 1984.
[19] J. J. Croat, J. F. Herbst, R. W. Lee, and F. E. Pinkerton, "Pr-Fe and Nd-Fe-based materials: A new class of high-performance permanent magnets (invited)," *Journal of Applied Physics,* vol. 55, pp. 2078-2082, 03/15/ 1984.
[20] J. J. Croat, J. F. Herbst, R. W. Lee, and F. E. Pinkerton, "High-energy product Nd-Fe-B permanent magnets," *Applied Physics Letters,* vol. 44, pp. 148-149, 01/01/ 1984.
[21] E. F. Kneller and R. Hawig, "The exchange-spring magnet: a new material principle for permanent magnets," *Magnetics, IEEE Transactions on,* vol. 27, pp. 3588-3560, 1991.
[22] J. M. D. Coey, "Rare-Earth Iron Permanent Magnets," *J.M.D. Coey, ed., Clarendon Press, Oxford, U.K.,* 1996.
[23] S. Bance, H. Oezelt, T. Schrefl, G. Ciuta, N. M. Dempsey, D. Givord, *et al.*, "Influence of defect thickness on the angular dependence of coercivity in rare-earth permanent magnets," *Applied Physics Letters,* vol. 104, p. 182408, 2014.
[24] S. Bance, J. Fischbacher, and T. Schrefl, "Thermally activated coercivity in core-shell permanent magnets," *Journal of Applied Physics,* vol. 117, p. 17A733, 2015.
[25] S. Bance, B. Seebacher, T. Schrefl, L. Exl, M. Winklhofer, G. Hrkac, *et al.*, "Grain-size dependent demagnetizing factors in permanent magnets," *Journal of Applied Physics,* vol. 116, p. 233903, 2014.
[26] M. Sagawa, S. Fujimura, H. Yamamoto, Y. Matsuura, and K. Hiraga, "Permanent magnet materials based on the rare earth-iron-boron tetragonal compounds," *Magnetics, IEEE Transactions on,* vol. 20, pp. 1584-1589, 1984.
[27] E. A. Périgo, E. P. Gilbert, and A. Michels, "Magnetic SANS study of a sintered Nd–Fe–B magnet: Estimation of defect size," *Acta Materialia,* vol. 87, pp. 142-149, 4/1/ 2015.
[28] O. Gutfleisch, "Advanced Structural Characterisation for Magnetic Materials " in *Proceeding of 18th international workshop on High Performance Magnets and their Applications*, Annecy, France, 2004, pp. 313-323.
[29] W. Szmaja, "Investigation of the domain structure of sintered Nd-Fe-B permanent magnets by Bitter-pattern method," *Czechoslovak Journal of Physics,* vol. 54, pp. 1503-1509, 2004/12/01 2004.
[30] !!! INVALID CITATION !!!
[31] T. T. Sasaki, T. Ohkubo, and K. Hono, "Structure and chemical compositions of the grain boundary phase in Nd-Fe-B sintered magnets," *Acta Materialia,* vol. 115, pp. 269-277, 8/15/ 2016.
[32] H. Sepehri-Amin, T. Ohkubo, T. Shima, and K. Hono, "Grain boundary and interface chemistry of an Nd–Fe–B-based sintered magnet," *Acta Materialia,* vol. 60, pp. 819-830, 2// 2012.

[33] W. F. Li, T. Ohkubo, T. Akiya, H. Kato, and K. Hono, "The role of Cu addition in the coercivity enhancement of sintered Nd-Fe-B permanent magnets," *Journal of Materials Research,* vol. 24, pp. 413-420, 2009.
[34] W. F. Li, T. Ohkubo, and K. Hono, "Effect of post-sinter annealing on the coercivity and microstructure of Nd–Fe–B permanent magnets," *Acta Materialia,* vol. 57, pp. 1337-1346, 3// 2009.
[35] T. T. Sasaki, T. Ohkubo, K. Hono, Y. Une, and M. Sagawa, "Correlative multi-scale characterization of a fine grained Nd–Fe–B sintered magnet," *Ultramicroscopy,* vol. 132, pp. 222-226, 2013.
[36] K. Hono and H. Sepehri-Amin, "Strategy for high-coercivity Nd–Fe–B magnets," *Scripta Materialia,* vol. 67, pp. 530-535, 9// 2012.
[37] N. A. Spaldin, *Magnetic materials: fundamentals and applications*: Cambridge University Press, 2010.
[38] E. Zueco, W. Rave, R. Schäfer, A. Hubert, and L. Schultz, "Combined Kerr-/magnetic force microscopy on NdFeB crystals of different crystallographic orientation," *Journal of Magnetism and Magnetic Materials,* vol. 190, pp. 42-47, 12/1/ 1998.
[39] L. Folks, R. Street, R. C. Woodward, and K. Babcock, "Magnetic force microscopy images of high-coercivity permanent magnets," *Journal of Magnetism and Magnetic Materials,* vol. 159, pp. 109-118, 6// 1996.
[40] W. Szmaja, "Investigations of the domain structure of anisotropic sintered Nd–Fe–B-based permanent magnets," *Journal of Magnetism and Magnetic Materials,* vol. 301, pp. 546-561, 6// 2006.
[41] S. R. Trout, "Understanding Permanent Magnet Materials: An Attempt at Universal Magnetic Literacy " *Magnequench International, Inc,* 2000. Available online at: http://spontaneousmaterials.com/Papers/CW2000.pdf. Retrieved on :21/10/2013.
[42] J. F. Herbst, "R2Fe14B materials: Intrinsic properties and technological aspects," *Reviews of Modern Physics,* vol. 63, pp. 819-898, 10/01/ 1991.
[43] J. M. D. Coey, "Hard Magnetic Materials: A Perspective," *Magnetics, IEEE Transactions on,* vol. 47, pp. 4671-4681, 2011.
[44] D. Givord, M. Rossignol, and V. M. T. S. Barthem, "The physics of coercivity," *Journal of Magnetism and Magnetic Materials,* vol. 258–259, pp. 1-5, 3// 2003.
[45] J. M. D. Coey, *Magnetism and magnetic materials*: Cambridge University Press, 2010.
[46] J. Thielsch, D. Suess, L. Schultz, and O. Gutfleisch, "Dependence of coercivity on length ratios in sub-micron Nd2Fe14B particles with rectangular prism shape," *Journal of Applied Physics,* vol. 114, p. 223909, 2013.
[47] J. Fujisaki, A. Furuya, Y. Uehara, K. Shimizu, H. Oshima, T. Ohkubo, *et al.*, "Micromagnetic Simulations of Magnetization Reversal in Misaligned Multigrain Magnets With Various Grain Boundary Properties Using Large-Scale Parallel Computing," *Magnetics, IEEE Transactions on,* vol. 50, pp. 1-4, 2014.
[48] F. A. Sampaio da Silva, N. A. Castro, and M. F. de Campos, "Modeling hysteresis curves of anisotropic SmCoFeCuZr magnets," *Journal of Magnetism and Magnetic Materials,* vol. 328, pp. 53-57, 2// 2013.
[49] H. Kronmüller, "Theory of Nucleation Fields in Inhomogeneous Ferromagnets " *Phys. Status Solidi B,* vol. 144, pp. 385–396, 1987.

[50] D. Givord, P. Tenaud, and T. Viadieu, "Coercivity mechanisms in ferrites and rare earth transition metal sintered magnets (SmCo5, Nd-Fe-B)," *Magnetics, IEEE Transactions on*, vol. 24, pp. 1921-1923, 1988.

[51] E. C. Stoner and E. P. Wohlfarth, "A Mechanism of Magnetic Hysteresis in Heterogeneous Alloys," *Philosophical Transactions of the Royal Society of London A: Mathematical, Physical and Engineering Sciences*, vol. 240, pp. 599-642, 1948-05-04 1948.

[52] D. Givord, M. F. Rossignol, D. W. Taylor, and A. E. Ray, "Coercivity analysis in Sm(Co, Cu, Fe, Zr)7−8 magnets," *Journal of Magnetism and Magnetic Materials*, vol. 104–107, Part 2, pp. 1126-1128, 2/2/ 1992.

[53] S. Bance, G. Ciuta, T. Shoji, T. Gao, G. Hrkac, M. Yano, *et al.*, "Hard magnet coercivity," in *Proceedings of 23rd international workshop on rare earth and future permenant magnets and their applications (REPM2014)*, Annapolis, Maryland 2014.

[54] R. Street and S. D. Brown, "Magnetic viscosity, fluctuation fields, and activation energies (invited)," *Journal of Applied Physics*, vol. 76, pp. 6386-6390, 1994.

[55] P. Gaunt, "Magnetic viscosity and thermal activation energy," *Journal of Applied Physics*, vol. 59, pp. 4129-4132, 1986.

[56] E. P. Wohlfarth, "The coefficient of magnetic viscosity," *Journal of Physics F: Metal Physics*, vol. 14, p. L155, 1984.

[57] D. Givord, A. Lienard, P. Tenaud, and T. Viadieu, "Magnetic viscosity in Nd-Fe-B sintered magnets," *Journal of Magnetism and Magnetic Materials*, vol. 67, pp. L281-L285, 1987/07/01 1987.

[58] G. B. Ferguson, K. O. Grady, and J. Popplewell, "Magnetisation mechanisms and magnetic viscosity in NdFeB alloys," *IEEE Transactions on Magnetics*, vol. 25, pp. 3449-3451, 1989.

[59] L. Folks and R. Street, "Analysis and interpretation of time dependent magnetic phenomena (invited)," *Journal of Applied Physics*, vol. 76, pp. 6391-6395, 1994.

[60] A. Hubert and R. Schafer, *Magnetic domains: the Analysis of Magnetic Microstrucutres* vol. 21. Berlin, Germany: Springer-Verlag, 1998.

[61] R. Bodenberger and A. Hubert, "Zur bestimmung der blochwandenergie von einachsigen ferromagneten," *physica status solidi (a)*, vol. 44, pp. K7-K11, 1977.

[62] W. Szmaja, J. Grobelny, M. Cichomski, S. Hirosawa, and Y. Shigemoto, "Magnetic force microscopy investigation of the domain structure of nanocomposite Nd2Fe14B/Fe3B magnets," *Acta Materialia*, vol. 59, pp. 531-536, 1// 2011.

[63] R. Ramesh and K. Srikrishna, "Magnetization reversal in nucleation controlled magnets. I. Theory," *Journal of Applied Physics*, vol. 64, pp. 6406-6415, 1988.

[64] P. Nothnagel, K. H. Müller, D. Eckert, and A. Handstein, "The influence of particle size on the coercivity of sintered NdFeB magnets," *Journal of Magnetism and Magnetic Materials*, vol. 101, pp. 379-381, 1991/10/01 1991.

[65] K. Uestuener, M. Katter, and W. Rodewald, "Dependence of the Mean Grain Size and Coercivity of Sintered Nd-Fe-B Magnets on the Initial Powder Particle Size," *IEEE Transactions on Magnetics*, vol. 42, pp. 2897-2899, 2006.

[66] W. F. Li, T. Ohkubo, K. Hono, and M. Sagawa, "The origin of coercivity decrease in fine grained Nd–Fe–B sintered magnets," *Journal of Magnetism and Magnetic Materials,* vol. 321, pp. 1100-1105, 4// 2009.

[67] H. Sepehri-Amin, Y. Une, T. Ohkubo, K. Hono, and M. Sagawa, "Microstructure of fine-grained Nd–Fe–B sintered magnets with high coercivity," *Scripta Materialia,* vol. 65, pp. 396-399, 9// 2011.

[68] K. Ono, T. Araki, M. Yano, N. Miyamoto, T. Shoji, A. Kato, *et al.*, "Element-Specific Magnetic Domain Imaging of (Nd, Dy)-Fe-B Sintered Magnets Using Scanning Transmission X-Ray Microscopy," *Magnetics, IEEE Transactions on,* vol. 47, pp. 2672-2675, 2011.

[69] G. Hrkac, T. G. Woodcock, C. Freeman, A. Goncharov, J. Dean, T. Schrefl, *et al.*, "The role of local anisotropy profiles at grain boundaries on the coercivity of Nd2Fe14B magnets," *Applied Physics Letters,* vol. 97, p. 232511, 2010.

[70] G. Hrkac, T. G. Woodcock, K. T. Butler, L. Saharan, M. T. Bryan, T. Schrefl, *et al.*, "Impact of different Nd-rich crystal-phases on the coercivity of Nd–Fe–B grain ensembles," *Scripta Materialia,* vol. 70, pp. 35-38, 1/1/ 2014.

[71] W. F. Brown, "Virtues and Weaknesses of the Domain Concept," *Reviews of Modern Physics,* vol. 17, pp. 15-19, 01/01/ 1945.

[72] T. Yamaoka, H. Tsujikawa, S. Hasumura, K. Andou, M. Shigeno, A. Ito, *et al.*, "Vacuum Magnetic Force Microscopy at High Temperatures: Observation of Permanent Magnets," *Microscopy Today,* vol. 22, pp. 12-17, 2014.

[73] Y. Fang, X. Yin, R. Skomski, H. Cheng, K. Song, M. Zhu, *et al.*, "In-situ high-temperature domain structures of die-upset Nd–Fe–B magnets," *Scripta Materialia,* vol. 111, pp. 72-75, 1/15/ 2016.

[74] W. Szmaja, J. Grobelny, M. Cichomski, K. Makita, and W. Rodewald, "MFM study of sintered permanent magnets," *Physica Status Solidi (A) Applied Research,* vol. 201, pp. 550-555, // 2004.

[75] W. Szmaja, "Improvements in magnetic domain studies by the colloid-scanning electron microscopy technique," *Materials Letters,* vol. 105, pp. 68-71, 8/15/ 2013.

[76] W. Szmaja, "Studies of the domain structure of anisotropic sintered SmCo5 permanent magnets," *Journal of Magnetism and Magnetic Materials,* vol. 311, pp. 469-480, 4// 2007.

[77] L. Folks and R. C. Woodward, "The use of MFM for investigating domain structures in modern permanent magnet materials," *Journal of Magnetism and Magnetic Materials,* vol. 190, pp. 28-41, // 1998.

[78] J. Thielsch, H. Stopfel, U. Wolff, V. Neu, T. G. Woodcock, K. Güth, *et al.*, "In situ magnetic force microscope studies of magnetization reversal of interaction domains in hot deformed Nd-Fe-B magnets," *Journal of Applied Physics,* vol. 111, // 2012.

[79] M. A. Al-Khafaji, D. G. R. Jones, W. M. Rainforth, M. R. J. Gibbs, H. A. Davies, and I. R. Harris, "Magnetic force imaging of domain structures for a (Pr/Nd)FeB alloy," *Journal of Applied Physics,* vol. 83, pp. 2715-2718, // 1998.

[80] M. A. Al-Khafaji, W. M. Rainforth, M. R. J. Gibbs, H. A. Davies, and J. E. L. Bishop, "Magnetic force microscopy of nanocrystalline NdFeB ribbons: A study of tip-sample interaction using a well-characterised sample," *Journal of Magnetism and Magnetic Materials,* vol. 182, pp. 111-123, // 1998.

[81] Y. Martin and H. K. Wickramasinghe, "Magnetic imaging by ‘‘force microscopy’’ with 1000 Å resolution," *Applied Physics Letters,* vol. 50, pp. 1455-1457, 1987.

[82] M. Al-Khafaji, W. M. Rainforth, M. R. J. Gibbs, J. E. L. Bishop, and H. A. Davies, "The origin and interpretation of fine scale magnetic contrast in magnetic force microscopy: A study using single-crystal NdFeB and a range of magnetic force microscopy tips," *Journal of Applied Physics,* vol. 83, pp. 6411-6413, 1998.

[83] K. Khlopkov, O. Gutfleisch, D. Hinz, K. H. Muller, and L. Schultz, "Evolution of interaction domains in textured fine-grained Nd_2 Fe $_{14}$ B magnets," *Journal of Applied Physics,* vol. 102, pp. 023912-10, 07/15/ 2007.

[84] W. Szmaja, J. Grobelny, and M. Cichomski, "Domain structure of sintered $SmCo_5$ magnets studied by magnetic force microscopy," *Applied Physics Letters,* vol. 85, pp. 2878-2880, 2004.

[85] P. Systems, "XEI image processing software ", 1.8.0.Build20 ed. Korea Park Systems, 2011

[86] P. Systems, *Software Manual of XEI Powerful Image Processing Tool for SPM*, Version 1.5 ed. Korea Park Systems Corporations, 2005

[87] I. Horcas, R. Fernández, J. M. Gómez-Rodríguez, J. Colchero, J. Gómez-Herrero, and A. M. Baro, "WSXM: A software for scanning probe microscopy and a tool for nanotechnology," *Review of Scientific Instruments,* vol. 78, p. 013705, 2007.

[88] W. Szmaja, "Digital image processing system for magnetic domain observation in SEM," *Journal of Magnetism and Magnetic Materials,* vol. 189, pp. 353-365, 11/16/ 1998.

[89] Y. Hua, C. Buenviaje-Coggins, Y.-h. Lee, J.-m. Lee, K.-d. Ryang, and S.-i. Park, "New three-dimensional AFM for CD measurement and sidewall characterization," vol. 7971, ed, 2011, pp. 797118-797118-6.

[90] M. A. Al-Khafaji, W. M. Rainforth, M. R. J. Gibbs, H. A. Davies, and J. E. L. Bishop, "The effect of phase constitution on the magnetic structure of nanophase NdFeB alloys observed by magnetic force microscopy," *Journal of Magnetism and Magnetic Materials,* vol. 188, pp. 109-118, // 1998.

[91] X.-M. Li, Y.-K. Fang, Z.-H. Guo, T. Liu, Y.-Q. Guo, W. Li, *et al.*, "Magnetic domain structures of precipitation-hardened SmCo 2:17-type sintered magnets: Heat treatment effect," *Chinese Physics B,* vol. 17, p. 2281, 2008.

[92] W. Szmaja, J. Grobelny, M. Cichomski, and K. Makita, "Application of MFM for studying Nd–Fe–B magnets," *Vacuum,* vol. 74, pp. 297-300, 5/24/ 2004.

[93] M. Takezawa, Y. Kimura, Y. Morimoto, and J. Yamasaki, "Analysis of Magnetization Reversal Process of Nd-Fe-B Sintered Magnets by Magnetic Domain Observation Using Kerr Microscope," *Magnetics, IEEE Transactions on,* vol. 49, pp. 3262-3264, 2013.

[94] D. J. Craik and E. D. Isaac, "Magnetic Interaction Domains," *Proceedings of the Physical Society,* vol. 76, p. 160, 1960.

[95] Y.-K. Fang, L. Yang, W. Li, L. Zhen, and B.-S. Han, "Magnetic microstructures of a high coercivity Nd–Fe–B sintered magnet in remanent and incomplete thermal demagnetization states," *Journal of Magnetism and Magnetic Materials,* vol. 322, pp. 3720-3723, 11// 2010.

[96] W. Rodewald, M. Katter, B. Wall, R. Blank, G. W. Reppel, and H. D. Zilg, "Dependence of the coercivity HcJ of high energy Nd-Fe-B magnets on the

alignment coefficient," *Magnetics, IEEE Transactions on,* vol. 36, pp. 3279-3281, 2000.

[97] J. D. Livingston, "Magnetic domains in sintered Fe-Nd-B magnets," *Journal of Applied Physics,* vol. 57, pp. 4137-4139, 1985.

[98] M. A. Al-Khafaji, W. M. Rainforth, M. R. J. Gibbs, J. E. L. Bishop, and H. A. Davies, "The effect of tip type and scan height on magnetic domain images obtained by MFM," *Magnetics, IEEE Transactions on,* vol. 32, pp. 4138-4140, 1996.

[99] D. Płusa, J. J. Wysłocki, B. Wysłocki, and R. Pfranger, "Domain-wall energy in sintered Nd15Fe77B8 permanent magnet," *Applied Physics A,* vol. 40, pp. 167-170, 1986/07/01 1986.

[100] M. Iavarone, S. A. Moore, J. Fedor, S. T. Ciocys, G. Karapetrov, J. Pearson, *et al.*, "Visualizing domain wall and reverse domain superconductivity," *Nat Commun,* vol. 5, 28/08/ 2014.

[101] Y. Fang, X. Yin, R. Zhao, S. Valloppilly, W. Li, M. Zhu, *et al.*, "Magnetic micro-structural uniformity of die-upset Nd-Fe-B magnets," *Journal of Applied Physics*, vol. 111, pp. 07A734-3, 04/01/ 2012.

[102] R. Szymczak, H. Szymczak, and E. Burzo, "Domain wall energy in Nd2 (Fe,Co,Al)14 B alloys," *Magnetics, IEEE Transactions on,* vol. 23, pp. 2536-2538, 1987.

[103] L. Yue, Y. Jin, W. Zhang, and D. J. Sellmyer, "Magnetic Force Microscopy Study of Zr_2Co_{11}-Based Nanocrystalline Materials: Effect of Mo Addition," *Journal of Nanomaterials,* vol. 2015, p. 5, 2015.

[104] H. W. Chang, W. C. Chang, Z. Y. Pang, S. H. Han, and B. S. Han, "Investigation of magnetic properties, after effect and MFM of $Pr_yFe_{90-y}B_{10}$ (y=8−11.76) nanocomposites," *Journal of Magnetism and Magnetic Materials,* vol. 279, pp. 149-159, 8// 2004.